Università degli Studi di Padova
Centro interdipartimentale "Centro Ricerche Fusione"

Universidade de Lisboa
Instituto Superior Técnico (IST)

JOINT RESEARCH DOCTORATE IN FUSION SCIENCE AND ENGINEERING
Cycle XXVIII
and
ERASMUS MUNDUS International Doctoral College in Fusion Science and Engineering

Real Time Plasma State Monitoring

Coordinator of the course: Prof. Paolo Bettini
Supervisor: Prof. Paolo Bettini
Advisors: Dr. Giuseppe Marchiori, Prof. Bernardo Brotas Carvalho

PhD student: Ondrej Kudlacek

Padova, January 2016

Signatures:

Coordinator: **Prof. Paolo Bettini**

Supervisor: **Dr. Giuseppe Marchiori**

Candidate: **Ondrej Kudlacek**

ABSTRACT

Real Time Plasma State Monitoring

by

Ondrej Kudlacek

The thesis describes several methods of plasma state monitoring for feedback control. For a tokamak device operation, one needs to gain in real time some information about the plasma state. The amount of needed information increases with the size of the device. In small machines, such as ISTTOK and Golem, the plasma current centroid position control is sufficient, as the heat fluxes are low and the plasma is in limiter regime. In larger devices, like RFX-mod, TCV or ASDEX-Upgrade with more complex plasma shapes and higher heat fluxes on the first wall, it is necessary to measure and control the plasma shape and the heat flux deposition location on the first wall (strike points in diverted regime and plasma-wall contact point in limited regime). The plasma performance is also strongly affected by internal current and pressure profile shape. Additionally, the bootstrap current fraction, that can not be directly measured, plays significant role in more advanced tokamak operation regimes. These quantities related to internal profiles have to be well diagnosed in order to avoid disruptions and mitigate the MHD instabilities. The thesis deals with all the above mentioned layers of control complexity, starting from the simplest ones focused on plasma current centroid position measurement on ISTTOK, over more complicated real time shape and equilibrium monitoring to the most advanced tools useful for plasma internal profiles monitoring, control, instabilities mitigation and disruption avoidance. The work described in this thesis provides original contribution to each category of these methods.

The first part of the thesis deals with real time applicable plasma current centroid position measurement on ISTTOK. In the frame of this work, two major issues had to be solved. The first, which is common for most small devices with highly conductive shell, is related to the impact of

the eddy currents induced in the conductive structures that corrupt the magnetic diagnostic signal and consequently disable the plasma current centroid position measurement. This was solved by a simple, real time applicable state space model that takes into account both the vacuum vessel and the shell and is capable to clean all 12 magnetic sensors installed on ISTTOK from the eddy currents effect. The method has also been tested on RFX-mod and on data from tokamak Golem located in Prague, Czech Republic. The second problem is that the present magnetic diagnostics on ISTTOK is not well calibrated. Therefore a simple method less sensitive to calibration errors was used and validated against Heavy Ion Beam vertical position estimate. The resulting algorithm is reliable enough and capable of providing information about the plasma current centroid position both for real time plasma control and offline post-discharge analysis. In addition, a more advanced method of the plasma current centroid position measurement was proposed to be used after the magnetic diagnostic upgrade planned in near future.

The next part of the work is dedicated to the tools for plasma shape and global macroscopic parameters measurement. It was performed on RFX-mod, a medium sized reversed field pinch operated also in tokamak regime. It is important especially because it started a diverted discharges program last years with the aim of performing MHD active control experiments in H-mode plasma. This part of the research activity focuses on the development of an algorithm for reliable plasma boundary reconstruction, both real time and offline that is applicable on RFX-mod. A real time plasma boundary reconstruction algorithm based on magnetic flux extrapolation in the vacuum suited to RFX-mod was developed and validated against Grad-Shafranov solver MAXFEA. This algorithm provides very good results (error below 2 % of the plasma minor radius) even in the presence of the limited poloidal number of sensors (8 pick-up coils and 8 poloidal flux loops) in RFX-mod with respect to standard tokamaks. As the algorithm does not provide just the knowledge of the plasma boundary, but it is also capable to compute the magnetic field and flux everywhere in the vacuum, it can be used to calculate several equilibrium related parameters such as $\beta_p + l_i/2$ or q_{95} in post-discharge analysis. For elongated discharges, the β_p and l_i can be also separated. The value of β_p provided by this algorithm is almost identical with an independent diamagnetic measurement. It was also used to provide feedback signals to the plasma shape control system designed for RFX-mod diverted discharges. Some shape control operation results are also reported in the thesis. The initial work on the real time plasma shape measurement and control opened the way to LH transition experiments. These experiments have shown H-mode evidence neither in steady state nor in transition phases of the ohmic discharges (mainly current ramp-up and ramp-down). However, the possibility of achieving H-mode in ohmic discharges is not excluded in future campaigns, since

the feedback control on plasma density has been significantly improved. As a second attempt, a biasing electrode to induce LH transition was built and another campaign was carried out. These experiments were successful, since several clear signs of LH transition were observed: the steep drop of H_α signal, increase of plasma density and pedestal formation at the edge. The description of these experiments is given within the thesis.

The last part of the thesis was dedicated to a tool that is being developed to improve present methods of control of plasma current, temperature, pressure profile, and disruption avoidance, RApid Plasma Transport simulatOR (RAPTOR). This code complements a simple set of real time diagnostics and computes the missing information using a lightweight set of transport equations. The thesis contains description of the code, especially the physical simplifications made to cope the computational speed requirements of a real time code, and reports possible applications in the field of disruption prediction and avoidance. Dedicated experiments to test the prediction method have been performed on RFX-mod for Resistive Wall Mode disruptions in discharges with $q(a) < 2$ and on TCV for density limit disruptions. In both disruption classes, the sawteeth behavior is significantly modified before the disruption, but the modification is not reflected in the RAPTOR prediction. Therefore the sawteeth period has been used as a feedback variable: huge discrepancy between RAPTOR and experimental sawteeth period activates the disruption alarm. The experiments showed that RAPTOR in its present state of development is a valid tool for disruption prediction in ohmic L-mode plasma without significant shape changes: in RFX-mod, the disruption alarm was activated several tens of milliseconds before the disruption and in TCV hundreds of milliseconds before. The main benefit is that this method is physics based, hence it does not require huge discharge database to train neural networks as the present algorithms. It is also transferable from one device to another, which is not the case of present days disruption prediction tools. However, the future disruption avoidance tools must be capable to deal with much more complex plasmas than the studied L-mode ohmic cases. The last section of this thesis gives examples of disruption prediction on ASDEX-Upgrade and identifies the gaps that must be filled before RAPTOR becomes a full-blown disruption prediction tool. First of all, inclusion of all heating and current drive sources will be needed. Second important issue is the inclusion of a model of a fast ion pressure, that significantly contributes to the total plasma energy content and affects MHD modes dynamics, for example stabilizes sawteeth. Another important piece of the puzzle is the coupling of a real time Grad-Shafranov solver with RAPTOR, that can improve the equilibrium reconstruction quality, which is closely related for example to the control of the NTM instabilities. Last, not least, huge benefit can be obtained from a better real time estimate of the electron temperature profile by plasma diagnostics.

Riassunto

Monitoraggio dello stato di plasma in tempo reale

di

Ondrej Kudlacek

La tesi descrive diversi metodi di stima e monitoraggio di grandezze di plasma utilizzabili anche per applicazioni di controllo in retroazione. Informazioni in tempo reale sullo stato del plasma sono necessarie per l'operazione di qualsiasi dispositivo Tokamak. In piccole macchine, come ISTTOK e Golem il controllo della posizione del centroide della corrente di plasma è sufficiente poiché i flussi termici sono bassi e il plasma si trova in regime "limiter". In dispositivi più grandi, come RFX-mod, TCV o ASDEX-Upgrade caratterizzati da più complesse forme di plasma e da più elevati flussi termici sulla prima parete, è necessario stimare e controllare la forma del plasma e la localizzazione della deposizione del carico termico sulla prima parete ("strike points" nei regimi con divertore e punto di contatto plasma-parete nei regimi con "limiter"). I risultati degli impulsi di plasma sono anche fortemente influenzati dalla forma dei profili interni di corrente e pressione. Inoltre, anche la frazione di corrente di "bootstrap", che non può essere direttamente misurata, gioca un ruolo importante nei regimi di operazione dei Tokamak più avanzati. Queste grandezze, collegate ai profili interni, devono essere ben diagnosticate per evitare disruzioni e mitigare le instabilità MHD. La tesi affronta tutti i summenzionati livelli di complessità del controllo, partendo dai più semplici centrati intorno alla misura della posizione del centroide della corrente di plasma in ISTTOK, presentando poi più elaborati metodi di monitoraggio in tempo reale dell'equilibrio e della forma di plasma fino agli strumenti più avanzati per la ricostruzione dei profili interni di plasma, per la mitigazione delle instabilità e per evitare le disruzioni. In questa tesi vengono forniti originali contributi a ciascun gruppo di questi metodi. La prima parte della tesi tratta della misura in tempo reale della posizione del centroide della corrente di plasma in ISTTOK. Nell'ambito di questo lavoro è stato necessario risolvere due problemi principali. Il primo, comune alla maggiore parte dei piccoli dispositivi con una scocca altamente conduttiva, è collegato agli effetti delle correnti parassite indotte nelle strutture conduttive, che alterano il segnale delle diagnostiche magnetiche e, conseguentemente, rendono inutilizzabile la misura della posizione del centroide della corrente di plasma. Questo problema è stato risolto grazie all'implementazione in tempo reale di un semplice modello alle variabili di stato che considera la presenza sia della camera da vuoto sia della scocca ed è in grado di rimuovere l'effetto delle correnti parassite da tutti i 12 sensori magnetici installati in ISTTOK. Il metodo è

stato provato anche con dati di RFX-mod e del Tokamak Golem, situato a Praga, nella Repubblica Ceca. Il secondo problema è la non accurata calibrazione delle diagnostiche magnetiche in IST-TOK. Ciò ha richiesto l'uso di un metodo semplice e meno sensibile agli errori di calibrazione. Tale metodo è stato poi validato confrontando la posizione verticale con quella stimata tramite il Fascio di Ioni Pesanti (Heavy Ion Beam). L'algoritmo risultante è sufficientemente affidabile e capace di fornire informazioni sulla posizione del centroide della corrente di plasma sia per il controllo in tempo reale sia per analisi "off-line" post-scarica. È stato inoltre proposto un metodo più avanzato per la misura della posizione del centroide della corrente di plasma da usarsi dopo il miglioramento della diagnostica magnetica programmato nel prossimo futuro.

La parte successiva del lavoro è dedicata allo sviluppo degli strumenti per la ricostruzione della forma di plasma e per la misura di parametri macroscopici globali. È stata svolta su RFX-mod, attualmente il più grande dispositivo reversed field pinch (RFP), in grado di operare anche in configurazione Tokamak. In particolare, in questa seconda modalità è iniziato già da qualche anno un programma di scariche a doppio (DN) o singolo nullo (SN) con il fine di eseguire esperimenti di controllo attivo di modi MHD con plasmi in modo H. Questa parte dell'attività di ricerca si è focalizzata nello sviluppo di un algoritmo per una affidabile ricostruzione del contorno di plasma, da utilizzarsi sia in tempo reale che "off-line" in RFX-mod. Tale algoritmo si basa sull'estrapolazione in vuoto del flusso magnetico ed è stato validato confrontandone i risultati con quelli forniti dal codice di equilibrio MAXFEA, solutore a elementi finiti dell'equazione di Grad-Shafranov. L'algoritmo fornisce risultati molto buoni (errore sotto il 2 % del raggio minore di plasma) anche in presenza del limitato numero di sensori lungo la circonferenza poloidale in RFX-mod rispetto ai Tokamak standard (8 sensori biassiali per la misura delle componenti poloidale e toroidale del campo magnetico e 8 per la misura del flusso poloidale). Poiché l'algoritmo non fornisce solo la conoscenza del contorno di plasma, ma è in grado di calcolare il campo magnetico e il flusso ovunque nel vuoto, esso può essere usato per la stima di parecchi parametri di equilibrio come $\beta_p + l_i/2$ o q_{95} in analisi post-scarica. Per scariche elongate, β_p e $l_i/2$ possono essere separati. Il valore di β_p fornito da questo algoritmo è quasi identico a quello ottenuto tramite una misura diamagnetica indipendente. L'implementazione in tempo reale ha permesso il calcolo dei segnali di retroazione del sistema di controllo della forma di plasma progettato per l'esecuzione delle scariche con doppio o singolo nullo. Alcuni risultati delle operazioni con controllo di forma sono riportati nella tesi. Il lavoro iniziale sulla ricostruzione e il controllo in tempo reale della forma di plasma hanno aperto la strada agli esperimenti di transizione L-H in scariche puramente ohmiche. Questi esperimenti non hanno mostrato prove di accesso al modo H né durante la fase stazionaria né in quelle transitorie (principalmente crescita e decrescita

della corrente) della scarica. Tuttavia, poiché il controllo in retroazione della densità di plasma è stato migliorato in modo significativo, la possibilità di accedere al modo H in scariche puramente ohmiche non è esclusa in campagne future. Dopo questi tentativi iniziali senza buon esito, gli sforzi si sono concentrati sulla possibilità di ottenere la transizione L-H indotta da elettrodo di polarizzazione. Questi esperimenti hanno avuto successo, essendo stati osservati parecchi chiari segni di transizione L-H: la ripida caduta del segnale H_α, l'incremento della densità di plasma e la formazione del piedistallo al bordo. La descrizione di questi esperimenti è presentata nella tesi.

L'ultima parte della tesi è stata dedicata ad uno strumento in corso di sviluppo per migliorare gli attuali metodi di controllo dei profili di corrente, temperatura, pressione di plasma e prevenzione delle disruzioni, denominato RApid Plasma Transport simulatOR (RAPTOR). Questo codice fa da complemento a un semplice insieme di diagnostiche in tempo reale e calcola le informazioni mancanti utilizzando un ridotto insieme di equazioni di trasporto. La tesi contiene la descrizione del codice, specialmente le semplificazioni fisiche fatte per soddisfare i requisiti di velocità di calcolo posti da un'applicazione in tempo reale, e presenta possibili applicazioni nel campo della predizione e prevenzione delle disruzioni. Esperimenti dedicati sono stati eseguiti in RFX-mod per provare un metodo di predizione delle disruzioni dovute alle instabiltà Resistive Wall Mode (RWM) in scariche con $q(a) < 2$ e in TCV per la predizione di disruzioni dovute a limite di densità. In entrambe le classi di disruzione, i profili con denti di sega sono modificati significativamente prima della disruzione, ma la modifica non si riflette nella predizione di RAPTOR. Perciò il periodo dei denti di sega è stato usato come variabile di retroazione: una grande discrepanza tra RAPTOR e il periodo sperimentale dei denti di sega attiva l'allarme di disruzione. Gli esperimenti hanno mostrato che RAPTOR nel suo attuale stato di sviluppo è un valido strumento per la predizione delle disruzioni in plasma ohmici in modo L senza significative variazioni di forma: in RFX-mod, l'allarme di disruzione fu attivato parecchie decine di millisecondi prima della disruzione stessa e in TCV centinaia di millisecondi prima. Il maggiore vantaggio di questo metodo consiste nel suo essere basato sulla fisica del fenomeno, quindi non richiede enormi quantità di dati di scariche per addestrare reti neurali come gli attuali algoritmi. Esso è anche trasferibile da un dispositivo ad un altro, a differenza degli attuali strumenti di predizione delle disruzioni. Tuttavia i futuri strumenti di prevenzione delle disruzioni dovranno essere in grado di trattare plasmi molto più complessi di quelli studiati in questi casi di scariche in modo L ohmiche. L'ultima sezione di questa tesi dà esempi di predizione di disruzione in ASDEX-Upgrade e identifica le lacune che debbono essere colmate prima che RAPTOR diventi un strumento di predizione delle disruzioni pienamente maturo. Prima di tutto, sarà necessario includere tutte le sorgenti di riscaldamento e sostenimento della corrente ("current drive"). Un secondo importante

aspetto è l'inclusione della pressione degli ioni veloci, che contribuisce in modo significativo alla totale energia di plasma e influenza la dinamica dei modi MHD, per esempi stabilizzando i denti di sega. Un altro importante pezzo del puzzle è l'accoppiamento di un solutore dell'equazione di Grad-Shafranov in tempo reale con RAPTOR, che può migliorare la qualità della ricostruzione dell'equilibrio, collegata da vicino, per esempio, al controllo delle instabilità NTM. Ultimo, ma non meno importante, un enorme beneficio potrebbe essere ottenuto da una migliore stima in tempo reale del profilo di temperatura elettronica fornita dalla relativa diagnostica.

Resumo

Monitorização em Tempo Real do Estado do Plasma

por

Ondrej Kudlacek

Esta dissertação descreve vários métodos para monitorização do espaço de estados de um plasma de fusão para fins de controlo em malha fechada. Para a operação de um dispositivo têm de se adquirir informação relevante sobre o estado do plasma em tempo real. O volume da informação requerida aumenta com a própria dimensão física do dispositivo. Em pequenas máquinas com o ISTTOK, Lisboa e o Golem em Praga na República Checa pode ser suficiente a posição do centroide da corrente de plasma pois os fluxos de calor são baixos e o plasma está em regime de limitador. Em dispositivos de maior dimensão tais como o RFX-mod, TCV ou o ASDEX-Upgrade com perfis de plasma mais complexos e elevados fluxos de calor na primeira face das paredes internas é necessário medir e controlar o perfil de plasma e os locais de deposição de calor (pontos de impacto em regime diversor e ponto de contacto plasma-superfície em regime com limitador). A performance do plasma é também fortemente afetada pelo perfis internos de corrente e pressão no plasma. Adicionalmente a fração de corrente "boot-strap", que não pode ser medida diretamente, tem um papel significativo em regimes de operação avançada de tokamaks. Estas quantidades relacionadas com os perfis internos têm de ser devidamente diagnosticadas de forma a evitar disrupções de corrente e instabilidades MHD no plasma. Esta tese aborda estas complexidades no controlo mencionados em cima, partindo do problema da medição do centroide de corrente no ISTTOK passando por casos mais complicados de monitorização em tempo real de perfis e equilíbrio até à ferramentas mais avançadas utilizadas no diagnóstico, controlo e mitigação de instabilidade e disrupções. A primeira parte da tese aborda a medição em tempo real do centroide corrente de plasma no ISTTOK. No âmbito deste trabalho duas grandes problemas foram resolvidos. Em primeiro lugar tal como é comum na maioria dos pequenos tokamaks com uma carapaça altamente condutora está relacionada com o impacto da correntes de fuga induzida nas estruturas condutoras que corrompem fortemente os diagnósticos magnéticos e consequentemente inibem a medição fiável do centroide de corrente. Este aspecto foi resolvido por um modelo simples de espaço de estados aplicável em tempo real que toma em consideração a câmara de vácuo bem como a carapaça e que é capaz de "limpar" todos os sinais da 12 sondas magnéticas poloidais instaladas no ISTTOK afectadas pelas corrente de fuga. Este método foi também testado em RFX-mod e nos dados adquiridos previamente do tokamak Golem. O segundo problema é que

os diagnósticos magnéticos já não estão devidamente calibrados. Neste sentido um método simples menos sensível a erros de calibração foi desenvolvido e validado através da estimativa do posição vertical dada pelo diagnóstico de iões pesados do ISTTOK. O algoritmo resultante é suficientemente fiável e capaz de fornecer informação acerca da posição do centroide de corrente quer para controlo em tempo real do plasma quer para análise posterior de dados experimentais. Adicionalmente é proposto um método mais avançado de medição de centroide previsto para uma posterior remodelação futura dos diagnósticos magnéticos. A parte seguinte é dedicada ás ferramentas para diagnóstico de perfis e parâmetros macroscópicos globais do plasma. Foi desenvolvida para o RFX-mod, uma máquina de tamanho médio do tipo "Reversed field pinch" (RFP) mas passível de ser operado também em regime "tokamak", que é especialmente relevante pois nesse laboratório iniciou-se recentemente um programa experimental de descargas em regime diversor com o objectivo de alcançar o controlo ativo de plasmas em "modo-H". Estas atividades de investigação focaram-se no desenvolvimento de um algoritmo robusto de reconstrução da camada limite de plasma do RFX-mod quer em tempo real quer em análises diferidas. Um algoritmo de reconstrução da fronteira de plasma baseada na extrapolação do fluxo magnético na região de vácuo adaptado ao RFX-mod foi desenvolvido e validado pelo código de equilíbrio Grad-Shafranov MAXFEA. Este algoritmo fornece resultados de grande qualidade (erro inferior a 2 % no raio menor do Plasma) apesar de um número limitado de sensores (8 sondas "pick-up" e 8 lacetes de fluxo) quando comparado com outros grandes tokamaks. Como o algoritmo fornece não apenas a informação sobre a fronteira de plasmas mas também é capaz de calcular o campo magnético em todo o espaço de vácuo então é útil para o cálculo de um conjunto de parâmetros de equilíbrio plasma como o $\beta_p + l_i/2$ ou q_{95} durante a análise diferida. Para descargas alongadas o β_p e o l_i podem ainda ser isolados. O valor de β_p dado por este algoritmo é quase idêntico ao obtido de forma independente pelo diagnostico de lacete diamagnético. Foi também usado para obter os sinais de realimentação para o sistema de controlo de perfil de plasma projetado para as descargas em regime diversor do RFX-mod. Alguns resultados experimentais de operação de controlo de perfis são apresentados na Tese. Estes progressos iniciais no diagnóstico e controlo em tempo real de parâmetros de plasma abriu o caminho para as experiências de transição de modo $L->H$. Infelizmente estes ensaios não evidenciaram o "modo-H" quer em regime estacionário quer transitório das descargas do RFX-mod (principalmente as rampas de subida e descida da corrente de Plasma). No entanto este não irá necessariamente de ser o caso das próximas campanhas experimentais dado que o circuito de realimentação da densidade de plasma foi entretanto significativamente melhorado. Como as primeiras tentativas falharam focámo-nos nas indução da transição $L->H$ por eletrodos polarizados. Estas experiências foram bem sucedidas, dado que revelaram sinais claros da transição

$L->H$: a queda abrupta do sinal H_α, aumento da densidade e a formação de um pedestal na borda do plasma. A descrição destas experiências é apresentada nesta Tese. A última parte da dissertação é dedicada a uma ferramenta que está a ser desenvolvida para melhorar os métodos acuais de controlo da corrente de plasma, temperatura e mitigação de disrupções "Rapid Plasma Transport simulatOR" (RAPTOR). Este código complementa um conjunto reduzido de diagnósticos em tempo real e calcula a informação em falta usando um conjunto reduzido das equações de transporte. A tese contém a descrição deste software em especial as simplificações físicas usadas para adequa-lo às restrições impostas aos códigos em tempo real e reporta possíveis aplicações no domínios da previsão e prevenção das disrupções. Foram ainda realizadas experiências dedicadas no RFX-mod a provocar disrupções do tipo "Resistive Wall Mode (RWM) com $q(a) < 2$ e no TCV com disrupções induzidas por densidade-limite. Em ambos os casos o comportamento de dente-de serra é significativamente alterado antes da disrupção, mas esta modificação não é visível na previsão RAPTOR. Desta forma o período de dente-de-serra tem sido usado como variável de realimentação: grandes discrepâncias entre o RAPTOR e o período observado ativa o alarme de disrupção. As experiências mostraram que o RAPTOR no estado atual de desenvolvimento constitui uma ferramenta válida para a previsão de disrupções em descargas de plasma modo-L óhmica, sem alterações significativas do perfil: no RFX-mod o alarme de disrupção foi acionado largas dezenas de milissegundo antes da dirupção e sendo no TCV centenas de milissegundo. O principal benefício foi que este método tem base nas equações físicas do sistema e portanto não necessita de uma grande base de dados para treinar previamente uma hipotética rede neuronal. É também facilmente transferível de uma máquina para outra ao contrário de outras ferramentas de previsão de disrupções. Em qualquer caso futuras ferramentas deste tipo deverão de ser capazes de lidar com plasmas bem mais complexos que o modo-L óhmico estudado aqui. A última seção da tese aponta alguns exemplos de previsão de disrupções no ASDEX-Upgrade e identifica as lacunas que têm de ser satisfeitas para que o RAPTOR se torne numa ferramenta completa. Primeiramente a inclusão de todas as fontes de geração de calor e corrente terão de ser feitas. Um segundo aspecto é a inclusão da pressão dos iões rápidos que contribui significativamente para a energia total de plasma e afecta a dinâmica dos modos MHD que, por exemplo, estabiliza os dentes-de-serra. Uma outra importante peça do puzzle é o entrosamento dos códigos tempo real de Grad-Shafranov com o RAPTOR, que poderá melhorar a qualidade da reconstrução do equilíbrio que por sua vez é importante, por exemplo, para o controlo de instabilidades do tipo NTM. Em último lugar, mas não de somenos importância, enormes benefícios podem ser alcançados com melhores estimativas de perfis da temperatura electrónica a partir dos diagnósticos de plasmas.

TABLE OF CONTENTS

CHAPTER I

Introduction

1.1 Human energy demand

Human civilization has always needed energy to exist. In the prehistoric times, the energy had been used for food preparation and heating. With increasing level of civilization progress, the energy requirements were increasing: human started producing metals, more and more food was thermally processed and also the heating requirements were increased. During industrial revolution, more energy was desired to power new factories or railway transport. Since then, the technologies are developing rapidly in many different directions: industry, transport, communication. All of the new inventions need more and more energy. In the beginning of the 21^{st} century, the energy demands are so high that the situation is not sustainable anymore. This is especially due to rapid industralization of countries like China, India or Africa that has not been industrialized before, so the energy demands were much lower.

Presently, more than 80 % of the energy used by the mankind comes from fossil fuels: according to [1], 31.4 % of primary energy comes from oil, 29 % from coal and 21.3 % from natural gas. From the non-fossil sources, biomass and waste contributes by 10 %, nuclear by 4.8 % and other renewable sources by 3.5 %. Due to the limited resources and negative impact on enviroment, the fossil fuels will have to be replaced by other sources of energy in a few decades. The first option is to reduce the consumption. On the contrary, the quality of life is strongly correlated with the primary energy need [2]. Unless the society agrees on significant decrease of life standards, the only possibility is to find new ways of energy production. The present-day renewable and nuclear technologies can not justify the increasing hunger for energy due to limited resources or ecological loads. The mankind needs to find an energy source which is ecologically harmless, the input 'fuel' is available worldwide

in sufficient quantity and can produce desired amount of energy. One of the options is the nuclear fusion.

1.2 Nuclear Fusion

Nuclear fusion is a process where two light atomic cores merge and form one heavier atomic core with slightly lower mass than the mass of the two original elements. Consequently, some energy proportional to the mass reduction is released. The best example is the fusion of hydrogen to helium, which is the source of energy of the Sun and stars. This process consists of complicated chain of nuclear reactions, that are too slow to be used for a reactor on the Earth. For this purpose, the most convenient reaction is the fusion of two hydrogen isotopes: deuterium consisting of one proton and one neutron and tritium consisting of one proton and two neutrons. The reaction

$$D + T \rightarrow He(3.5MeV) + n(14.1MeV) \tag{1.1}$$

produces 17.6 MeV of energy which is carried by the fusion products to the wall of the reactor. The reactor would be cooled and the heat would be used to produce electricity.

Around 1/6000 of the hydrogen on the Earth consists of Deuterium. The situation with Tritium is more complicated. As the half-time of this isotope is 12 years, it does not naturally occur on the Earth. However, it can be produced by the fission of Lithium induced by neutron emerged in the fusion reaction:

$$\begin{aligned} n + {}^{6}_{3}Li &\rightarrow T + He + 4.8MeV \\ n + {}^{7}_{3}Li &\rightarrow T + He + n - 2.5MeV. \end{aligned} \tag{1.2}$$

Using these two reactions, the Tritium fuel can be produced on site in the burning rate. A positive side effect of this approach is that there is no need of transport or storage of radioactive fuels. Lithium is present is sufficient amount in the see water. The reaction of Deuterium and Tritium seems to be an optimal candidate for a future source of energy: the fuel is available in large amount, is relatively cheap and there are no harmful products. The problem is technical feasibility of such a reactor.

For fusion to happen, one needs to bring the reactants close enough: the cores can fuse just in case that the short range strong nuclear force overcomes the electrostatic repulsion caused by positive charges of both reactants. To break the electrostatic barrier, the particles must be fast

enough. This requires very high temperature of the fuel mixture. The optimal temperature for the fusion of Deuterium and Tritium is around 10 keV, which corresponds to approximately 100 000 000 K [3]. Each material at this temperature is in plasma state.

The reaction has already been achieved on the Earth in uncontrolled manner in thermonuclear bombs. Electricity production requires a method to release the fusion energy in controlled and continuous manner. This requirement encounters the high temperature needed for fusion. There is no material that can stand so high temperatures, thus a feasible way to isolate the hot fuel from the wall must be found. There are two completely different approaches to achieve this task: magnetic confinement that isolates the fuel using external magnetic field and inertial confinement that rely on the inertia of the fuel that remains together for some time.

1.2.1 Inertial Confinement

Inertial confinement is based on compression of the fuel concentrated in small pellets. The fuel is compressed to very high density and at least a part of the fuel is heated to thermonuclear temperatures. The driver of the compression can be either a set of laser beams or heavy ion accelerator. After the beam hits the surface of the fuel pellet, the outer parts of the capsule are ionized. The plasma starts expanding with a velocity 100-1000 km/s outwards [3]. As a reaction, the internal part of the capsule is accelerated inwards with a velocity of 300-500 km/s [3]. Consequently, the fuel gets compressed and heated. If sufficiently high temperatures are achieved, a thermonuclear microexplosion of the fuel occurs. The products carry the heat to the wall of the reaction chamber.

Another method of compression, called indirect drive, is based on laser heating of the heavy metal (often golden) cylinder (called hohlraum). The hohlraum hit by laser generates X-rays that heat a fuel capsule located inside the hohlraum. The advantage of this method is that the fuel heating and compression by X-rays is much more efficient than the direct heating by lasers. This method is used on National Ignition Facility, the main progress driver in inertial fusion research. More detailed information about this experiment can be found in [4]. In 2013, the fusion energy gain was higher than the amount of energy absorbed by the fuel [4]. Unfortunately, the amount of energy used to generate the laser pulse is still much higher than the fusion gain. Similar device, Laser Megajoule, started operation in France in October 2014 [5]. Presently, no results related to the inertial fusion have been published.

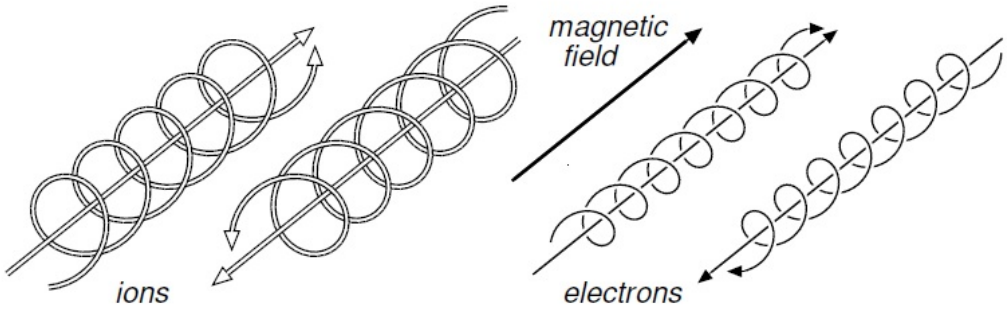

Figure 1.1: The trajectory of charged particles in presence of magnetic field. Figure taken from [6]

1.2.2 Magnetic Confinement

This method of plasma confinement uses the properties of charged particles in magnetic fields. The equation of motion of the particle in electromagnetic field is

$$m\frac{d^2\mathbf{r}}{dt^2} = q\mathbf{E} + q\mathbf{v} \times \mathbf{B}, \tag{1.3}$$

where m is the mass of the charged particle, $\mathbf{r}$ is the position vector, q is the charge of the particle, $\mathbf{v}$ is the particle velocity and $\mathbf{B}$ is the magnetic field. From this equation, one can see that a charged particle is accelerated along the electric field (in positive or negative direction depending on the charge). In the magnetic field, the motion along the constant magnetic field remains unaffected. On the contrary, the particle can not freely move perpendicularly to the magnetic field. In this direction, the particle is moving in a circle. The sum of these two motions forms a resulting particle trajectory with a spiral shape as shown in Fig. 1.1.

This property of charged particles motion is used to design the magnetic confinement devices: as the charged particles move freely along the magnetic field line and the motion perpendicular to the field lines is restricted, one can confine the particles on the magnetic field line that does not intersect the wall. This field configuration can be created by a set of toroidal field coils surrounding a tire-shape vacuum vessel, where the particles are confined (see Fig. 2.1).

However, in toroidal geometry, another component of the magnetic field must be added to guarantee plasma confinement. The reason of this are the particle drifts across the magnetic field because of the centrifugal force and ∇B drift in toroidal geometry. To compensate these drifts, upper and lower part of the device must be connected by a magnetic field line (see for example [9] for detailed explanation). The way of the field generation defines two families of toroidal magnetic confinement devices: tokamaks and reversed field pinches generate the field by the current induced in the plasma,

stellarators use external coils. As this thesis deals just with tokamak related issues, the description will be given just for this type of device.

CHAPTER II

Tokamaks

Tokamak has been the most successful device with plasma magnetic confinement and it is the main candidate for the first fusion reactor. The original concept was developed in 50^{th} in the Soviet Union. The scheme of tokamak is shown in Fig. 2.1. The confining field of the device is generated by the Toroidal Field Coils (TFC) and the poloidal component of the magnetic field is created by the plasma current and Poloidal Field Coils (PFC). Plasma current is induced by transformer: central solenoid serves as the primary winding and the plasma represents the secondary winding. There are also several methods for non-inductive current drive [3], [7]. As this thesis focuses mainly on plasma equilibrium control using external magnetic fields, a description of the theory related to this issue is given in this chapter.

2.1 Plasma equilibrium

In tokamaks, the particles follow magnetic field lines, whose direction is determined by the superposition of the toroidal magnetic field and poloidal magnetic field. The magnetic field lines are helically twisted and form a nested flux surface structure. Let us derive the equation that describes the shape of the flux surfaces.

Plasma equilibrium is described by the force balance MHD equation:

$$\nabla p = \mathbf{j} \times \mathbf{B}, \tag{2.1}$$

where p is the kinetic pressure and $\mathbf{j}$ is the current density. For computational purposes, it is more convenient to describe the tokamak equilibrium by scalar magnetic flux ψ than by vector magnetic

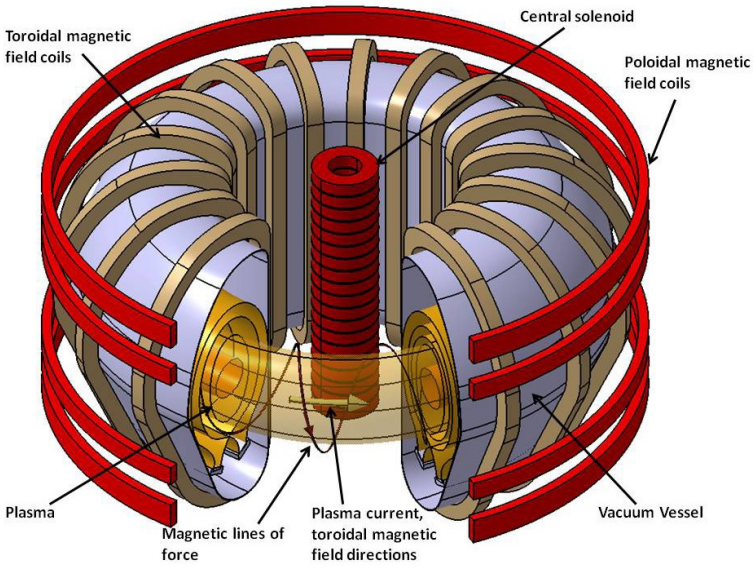

Figure 2.1: The scheme of tokamak. Figure taken from [3]

field.The following equation holds for ψ:

$$\nabla\psi \cdot \mathbf{B} = 0. \tag{2.2}$$

Using (2.1) and (2.2), one can derive two important properties of the flux surface. From (2.2), it can be directly deduced that the magnetic field lines stay on the flux surface with constant ψ. Scalar multiplication of (2.1) by $\mathbf{j}$ or $\mathbf{B}$ gives that the pressure gradient is perpendicular to both $\mathbf{j}$ and $\mathbf{B}$. Thus the current flows on the flux surface as well and the pressure is constant on the flux surface with constant ψ.

In general, magnetic field is the curl of the magnetic potential $\mathbf{A}$. Let us assume that the plasma configuration is axi-symmetric (the derivative $\partial/\partial\phi = 0$ in cylindrical coordinates) [10], [3]. The geometry of the problem is shown in Fig. 2.2. In this case, one can describe the situation just by $A_\phi(r, z)$ component of the magnetic potential. To justify (2.2), we choose $\psi(r, z) = rA_\phi(r, z)$ [10]. The magnetic field is expressed as

$$B_r = \frac{-1}{r}\frac{\partial\psi}{\partial z} \tag{2.3}$$

$$B_z = \frac{1}{r}\frac{\partial\psi}{\partial r}. \tag{2.4}$$

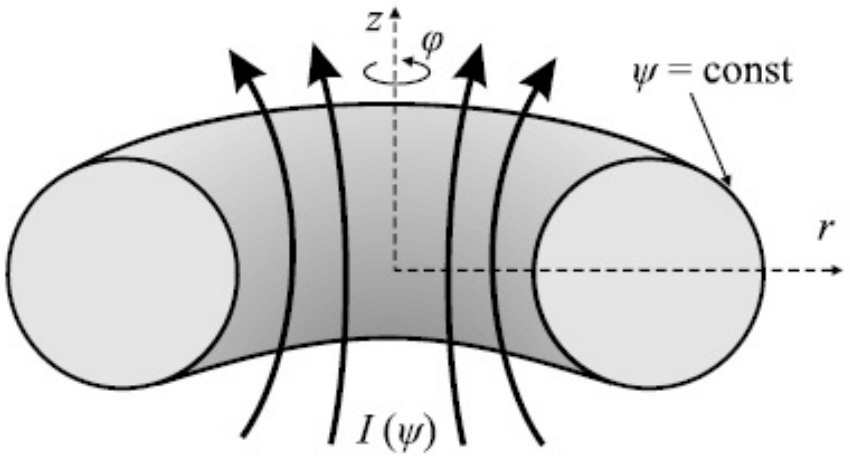

Figure 2.2: The geometry of tokamak flux surfaces. Figure taken from [10]

Using the radial component of (2.1) alongside with (4.2) and (2.4), one gets the basic equation describing the tokamak equilibrium, the Grad-Shafranov equation.

$$\frac{\partial^2\psi}{\partial z^2} + r\frac{\partial}{\partial r}\frac{1}{r}\frac{\partial\psi}{\partial r} + \frac{1}{2}\frac{\partial I^2(\psi)}{\partial\psi} + \mu_0 r^2\frac{\partial p}{\partial\psi} = 0, \tag{2.5}$$

where $I(\psi)$ is the current through poloidal layer bounded by the magnetic flux surface ψ (see Fig. 2.2). Solving this equation, one obtains the plasma boundary and flux surface geometry.

2.1.1 Equilibrium related quantities

Before further discussions of the equilibrium related problems, let us give some definitions of equilibrium related quantities that will be useful later in the thesis. The first important quantity is the poloidal beta β_p corresponding to the normalized kinetic pressure:

$$\beta_p = \frac{\bar{p}}{\frac{<B_a^2>}{2\mu_0}}, \tag{2.6}$$

where $\bar{p}$ corresponds to the mean value of kinetic pressure in the plasma and $< B_a^2 >$ is the average square poloidal magnetic field on the plasma boundary [7].

Another important quantity is the internal inductance l_i. This quantity describes how is the plasma current distributed and is defined as

$$l_i = \frac{\bar{B^2}}{< B_a^2 >}, \tag{2.7}$$

where $\bar{B^2}$ is the mean squared poloidal magnetic field inside the plasma. A combination of β_p and l_i

$$\Lambda = \beta_p + l_i/2 - 1, \tag{2.8}$$

will be used in the following text as well.

Further important property of the plasma is the safety factor defined as

$$q = \frac{d\Phi}{d\psi}, \tag{2.9}$$

where Φ is the toroidal magnetic flux [7]. This quantity is important because it describes plasma stability with respect to kink modes or tearing modes that will be discussed in section 2.4.

2.2 Plasma shaping

In the previous section, the Grad-Shafranov equation describing the full tokamak equilibrium was derived. This section will deal with more practical questions such as how to determine the plasma boundary or how to affect the plasma shape.

First of all, let us define two shape related quantities: plasma elongation and triangularity. Fig. 2.3 shows a shaped plasma with elongation k defined as

$$k = \frac{y_m}{R_2 - R_0} \tag{2.10}$$

and triangularity δ defined as

$$\delta = \frac{x_m}{R_2 - R_0}. \tag{2.11}$$

2.2.1 Plasma Boundary

Plasma boundary is defined by the last flux surface that does not intersect the wall. This is called the Last Closed Flux Surface (LCFS). The particles beyond the LCFS hit the wall, thus they are not confined anymore. The LCFS can be defined according to the configuration by two means determining also the regime of plasma operation: limited or diverted. Both are shown in Fig. 2.4 for ASDEX-Upgrade.

In the limiter configuration, plasma is restricted by a point on the first wall that is touching the LCFS.

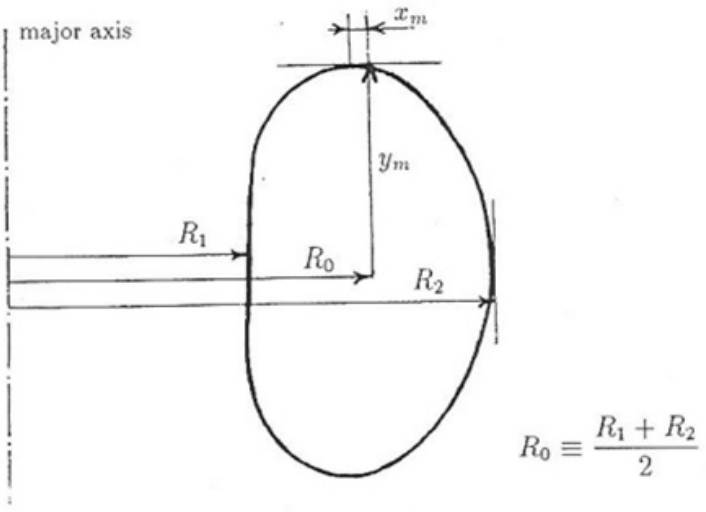

Figure 2.3: The shaped plasma.

In the diverted configuration, the plasma boundary is defined by combination of plasma and external magnetic fields: a point with zero poloidal magnetic field (referred as X-point) is created by a set of poloidal field coils between the plasma and the first wall. The last closed flux surface (which is in diverted configuration called separatrix) is the flux surface containing the X-point. All particles beyond this surface are diverted to the divertor target plates.

The limited configuration is used during the plasma start-up phase and in older devices and is simpler in terms of magnetic configuration generation. The diverted configuration needs several poloidal field coils to be created, on the other hand, the confined plasma is not in direct contact with the wall, thus the impurity content is reduced. In addition, it is much simpler to reach a regime with improved confinement (so called H-mode). On the other hand, all diverted plasmas are unstable in vertical direction. The origin of this instability will be explained in 2.2.3. However this instability is controllable and does not appear to be a severe issue for tokamak operation. Thus, diverted configuration is superior to the limited one and is used in modern machines as well as in future devices.

2.2.2 Radial Equilibrium

The plasma tends to expand in radial direction regardless plasma geometry. There are three reasons for this expansion: the first of them is the kinetic pressure, the second is the plasma current and the third one is the gradient of the toroidal magnetic field [8] (toroidal magnetic field is inversely proportional to the major radius). As mentioned above, the kinetic pressure is constant on the flux surface. Because the area of the outer part of the flux surface is lower than the inner one, the net

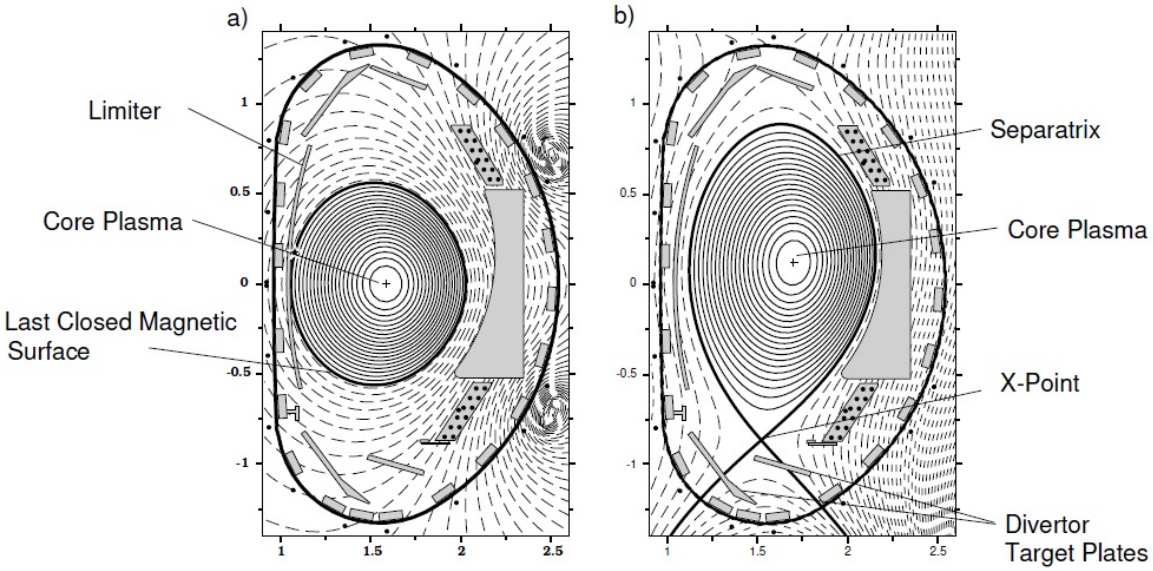

Figure 2.4: The regimes of plasma operation (a) limited operation and (b) diverted operation. Figure taken from [6]

effect of the pressure force causes radial expansion. Because any current loop tends to expand in radial direction to minimize the magnetic energy content of the system, the plasma current causes radial expansion as well. To compensate this effect a vertical field

$$B_z = \frac{-\mu_0 I_p}{4\pi R_0}\left(ln\left(\frac{8R_0}{a}\right) + \Lambda - 1/2\right) \tag{2.12}$$

must be generated by external poloidal field coils. In simplest case, this field can be created by a set of 2 poloidal field coils located on the low field side.

2.2.3 Equilibrium of Shaped and Diverted Plasma

In present day machines, the plasma shape is usually not circular, but deformed to a D-shape. In principle, this shape can be created by a set of 6 poloidal field coils as shown in Fig. 2.5. Real systems that generate such a shape are more complicated, the one in Fig. 2.5 is shown just for illustration.

Let us discuss one problem common for all machines with diverted regime or vertically shaped plasma, which is the case of all modern devices. The description is given for the devices creating the X-point, the explanation for vertically shaped plasma is analogical. As mentioned in section 2.2.1, X-point is generated by a set of poloidal field coils. The poloidal magnetic field at X-point is 0. Thus, the current direction in the poloidal field coil (coils) must be the same as the direction

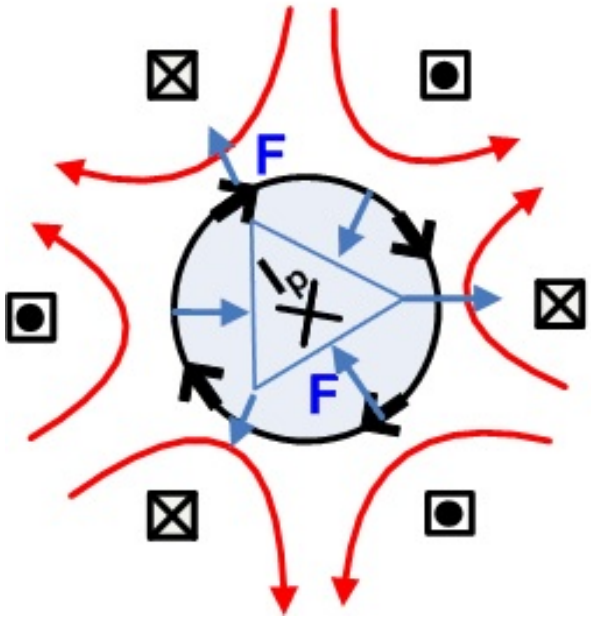

Figure 2.5: The principle of D-shape generation: plasma current (blue) is attracted by the currents with the same direction and repulsed by the currents with the opposite direction by the force F. Consequently, a D-shape is created (schematically represented by the blue triangle). The magnetic field of the poloidal field coils is represented by the red arrows. Figure taken from [12]

of the plasma current. The force between the coil and plasma is attractive as shown in Fig. 2.5. Additional coil (coils) must be placed to the device to compensate this effect. As the X-point is created on the upper/lower part of the device, upper part of the plasma will be attracted upwards and lower part downwards and the plasma shape will be elongated in vertical direction. The net force in equilibrium position will be equal to 0.

Let us discuss the stability of this equilibrium. Assume that the plasma is perturbed and moves downwards. In this case, the downward force will surpass the upward force and the plasma will move downwards. Consequently, the net force downwards will be bigger and bigger. In another words, the plasma position is unstable in vertical direction, as one can see also in Fig. 2.5.

2.3 Modes with improved confinement

One of the targets of tokamak operation is to improve the quality of the plasma confinement (maximize the energy content of the plasma for given toroidal magnetic field). Tokamaks can operate in several confinement regimes. The basic one, the mode with the lowest confinement, is called L-mode. If the power carried by particles through the separatrix exceeds certain threshold and the density is high enough, a mode with better confinement named H-mode is obtained [13]. This mode is characterized by reduced edge transport. In practice, it means that the same pressure profile as

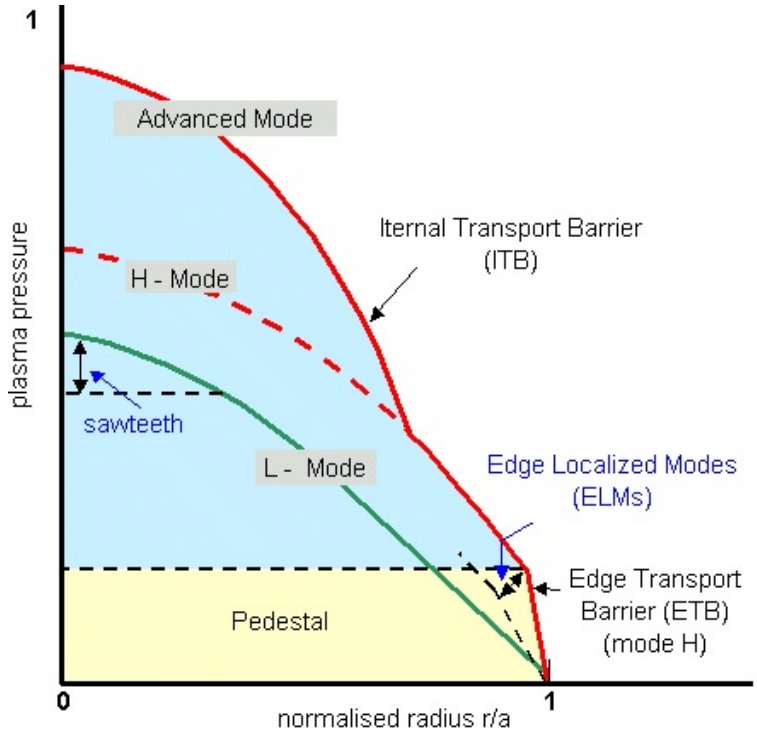

Figure 2.6: Plasma pressure profile as for different confinement modes. Figure taken from [16]

in L-mode stands on a pedestal at the edge as one can see in Fig. 2.6. Operating in this mode has a drawback of the Edge Localized Modes briefly described in section 2.4.

To improve the H-mode confinement, also an internal transport barrier can be generated. The internal transport barrier occurs in case that the current safety factor is elevated in the plasma core: naturally, the safety factor has the maximum at the edge (usually between 2 and 4) and minimum in the plasma core (usually around 1). If a convenient heating and current drive waveform is applied, this profile can be modified in such a way that the minimum of the safety factor is not in the core, but more towards the plasma edge. The internal transport barrier can be created at the same position as the minimum of the safety factor. More detailed information can be found in [14] for JET or in [15] for ASDEX-Upgrade.

2.4 Plasma Instabilities

Let us assume that the plasma macroscopic quantities like plasma edge position are controlled and we are trying to increase the performance of the device (plasma current and plasma kinetic pressure). Consequently, several internal MHD instabilities reducing the confinement quality or terminating the discharge can be triggered. The first instability to be mentioned is the sawtooth mode occurring in the plasma core.

2.4.1 Sawtooth Instability

The sawtooth instability appears as a periodic oscillation of the pressure in the plasma core. The instability is caused by magnetic field line reconnection close to the $q = 1$ flux surface [3]. It can be advantageous to remove the He ashes from the plasma core or to provide the power necessary to bring plasma to H-mode. The instability itself is not dangerous, but it can seed other more dangerous instabilities such as Neoclassical Tearing Modes.

2.4.2 Neoclassical Tearing Mode

These resistive MHD instabilities are caused by the reconnection of the magnetic field lines at rational q surfaces, in particular $q = 1.5$ and $q = 2$. Due to the magnetic reconnection, outer parts of the plasma are connected by a magnetic field line with the inner parts and the nested flux surface geometry is broken. It increases the heat conductivity outside the plasma core and thus deteroirates the confinement. The seed of the NTM is often the sawtooth instability.

The NTM's are stabilized by rotation. As long as the mode is rotating, the consequences of this instability are not severe, it just spoils the confinement. When the mode rotation is stopped (so called Locked Mode, LM), there is no stabilizing mechanism anymore and the plasma discharge can be terminated very quickly. This fast and uncontrolled plasma termination is called disruption and is discussed more in 2.4.5

2.4.3 Resistive Wall Modes

These modes appear in either plasma with very high β_N or very low edge safety factor. It determines the limits for plasma pressure. When occurs, it appears as unstable helical deformation of the plasma. The consequences of this instability are in general disruptive. The control is desired to increase the pressure limits and can be provided by active saddle coils located close to the plasma edge.

2.4.4 Edge Localized Modes

The Edge Localized Modes (ELM) are the instabilities of the plasma edge appearing in H-mode. ELM's are caused by the sudden collapse of the pedestal pressure gradient accompanied by ejection of part of the plasma energy to the first wall. ELM's do not have disruptive consequences, but the intensive and localized heat fluxes to the first wall can cause severe damage, which is not acceptable in

future devices. The ELM mitigation can be achieved for example by resonant magnetic perturbation created by saddle coils [17], [18].

2.4.5 Disruptions

Disruption is an event of sudden termination of the plasma discharge: the plasma current disappears within a few ms and the thermal energy is deposited to the first wall. It can be caused for example by vertical instability, RWM, LM, density above limit or too high impurity content. The waveforms of several relevant quantities during a JET density limit disruption are shown in Fig. 2.7. Before the disruption, some precursors appear: it can be for example density increase or 2/1 mode amplitude fluctuations as shown in Fig. 2.7. Afterwards, a disruption arrives.

The first phase of the disruption is the thermal quench: the magnetic field is ergodized due to an instability and the thermal energy is deposited on the divertor and limiter plates. This phase takes from hundreds of microseconds to few milliseconds and strongly depends on the machine size [3]. The most severe consequence can be melting of the first wall components. The next phase is called the current quench: as the plasma is cooled down, the resistivity is significantly increased. The ohmic heating winding is not capable to provide voltage that would compensate this resistivity drop. Consequently, the plasma current rapidly drops and currents are induced in the surrounding conductive structures. These currents interact with the toroidal magnetic field that does not disappear alongside the plasma creating huge $\mathbf{j} \times \mathbf{B}$ forces that can damage the support structure. Another dangerous consequence of disruption is the production of so called runaway electrons with energy in order of tens of MeV's that can take 2/3 of the pre-disruption current (10 MA on ITER) and destroy the in-vessel components [19].

Due to severe consequences on the machine, disruptions must be avoided in future power plants. On the contrary, future reactors are required to operate on as high plasma current and pressure as possible meaning that the system will be close to its operation limits. To fulfil both requirements, a reliable disruption prediction algorithms must be developed. One possibility will be proposed later in this thesis.

2.5 Experimental devices

The work on this thesis was elaborated on many experimental devices. The most basic part related to plasma current centroid measurement was performed on ISTTOK, most activities were related to RFX-mod and in the final part of the PhD, several experiments related to the disruption

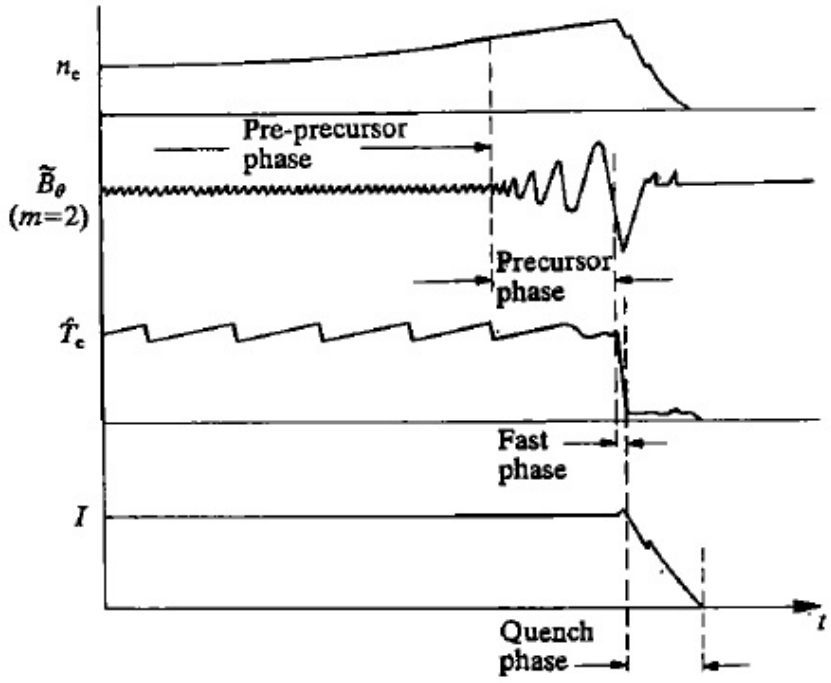

Figure 2.7: The waveforms of the electron density, 2/1 mode, core temperature, and plasma current for a JET density limit disruption. Image taken from [7].

avoidance were done on TCV and ASDEX-Upgrade. This chapter gives description of features of the devices that are relevant for the thesis.

2.5.1 ISTTOK

ISTTOK [20] is a small, large aspect ratio tokamak (major radius 0.46 m, minor radius 0.085 m, the highest plasma current I_p = 6 kA, toroidal magnetic field B_t = 0.5 T) operated in IPFN-IST, Lisbon, Portugal. The picture of this device is in Fig. 2.8. As the dimensions of the device are rather small, it concentrates mainly on the edge plasma studies using electrostatic probes and development of new diagnostics types, for example the heavy ion beam diagnostic [21], [22]. This diagnostics is able to measure the temperature, density, current profile and plasma vertical position simultaneously. The magnetic diagnostics consists of one array of 12 pick-up coils, one flux loop, a Rogowsky coil, one sine, and one cosine coil.

ISTTOK is using 3 poloidal field coils circuits: the magnetizing circuit that generates the loop voltage, vertical field circuit consisting of 4 poloidal field coils, each of them with 5 turns for the radial equilibrium and control of plasma radial position, and the radial field circuit for plasma vertical position control. This circuit consists of 2 poloidal field coils, each of them has 4 turns.

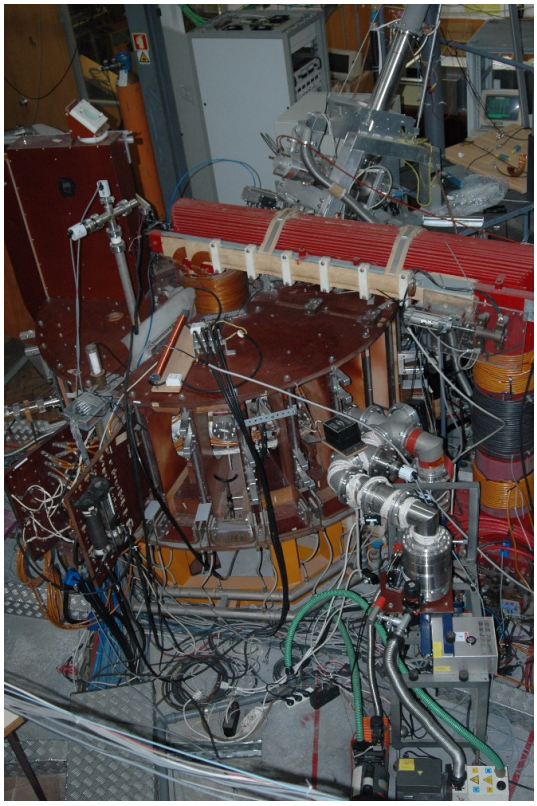

Figure 2.8: The ISTTOK machine.

One of the most interesting features of this tokamak is the capability of performing the alternate current discharges: as ISTTOK has an iron transformer core, the pulse length is limited by saturation. The longest pulse in the direct current regime is 100 ms. In the alternate current regime, the loop voltage and thus also the plasma current direction are reversed just before the core gets saturated. This process can be repeated several times, technical limits of the device restrict the discharge length to 3 s.

There are two conductive structures on ISTTOK: the highly conductive copper shell to stabilize the MHD modes with one poloidal and one toroidal gap and a continuous vacuum vessel. The toroidal gap enable plasma break-down and fast reversal of the current. The time constant of the shell is approximately 20 ms. On the contrary, the vacuum vessel is continuous to guarantee acceptable vacuum quality. The conductivity is rather low to enable plasma breakdown and fast reversals of the loop voltage. Its time constant is approximately 2 ms.

This thesis focused on a method of the current centroid measurement that can deal with both effects caused by conductive structures and current reversals.

2.5.2 RFX-mod

RFX-mod is a circular cross-section Reversed Field Pinch (RFP) [23] with major radius 1.995 m and minor radius determined by the graphite wall located at 0.459 m. The graphite tiles lie on the inner surface of an inconel vacuum-vessel, which is surrounded by a 3 mm thick stabilizing copper shell, and by an outer stainless-steel mechanical structure. There are 8 pairs of poloidal field shaping coils and 4 circuits of magnetizing coils symmetrical with respect to the midplane and located close to the support structure. RFX-mod can also be operated as a tokamak with toroidal magnetic field up to 0.55 T and using the poloidal field coils, circular, elongated and double null discharges can be performed. In addition, some pairs of the shaping coils can be disconnected to produce a single null discharge. The device is shown in Fig. 2.9.

One of the most interesting features of this device is the capability of performing tokamak discharges with edge safety factor below 2. This is enabled by a set of 192 independent active saddle coils and strategies developed for RFP discharges [24]. Using this set, the growth of the 2/1 RWM that naturally occurs for discharges with edge safety factor below 2 is avoided. In addition, the 2/1 mode locking in discharges with edge safety factor above 2 can be avoided. These results have been obtained for L-mode circular discharges, as reported for example in [25], [26].

The next target of this device is to repeat the same experiments for shaped plasma, possibly in H-mode. In addition to the operation with safety factor below 2, the RFX-mod saddle coils would be a very useful tool for ELM mitigation. As the device is different from other H-mode tokamaks, the RFX-mod could provide a useful input to the H-mode database.

Within this thesis, a new method of plasma boundary reconstruction was developed (see chapter IV). The results of this method have been used to provide feedback signals for a shape control system made up of a Kalman filter and a LQG controller (see chapter V). The new method was used to infer some plasma macroscopic parameters for general plasma shape (reported in chapter VI). The next part of the thesis was focused on computation related to H-mode accessibility taking advantage of both transient phases of the plasma discharge and biasing electrode that can bring the plasma to H-mode (detail are given in chapter VII).

2.5.3 TCV

A part of the activity on disruption avoidance developed within the thesis was elaborated on a medium sized machine, **T**okamak a **C**onfiguration **V**ariable (TCV). The major radius is 89 cm,

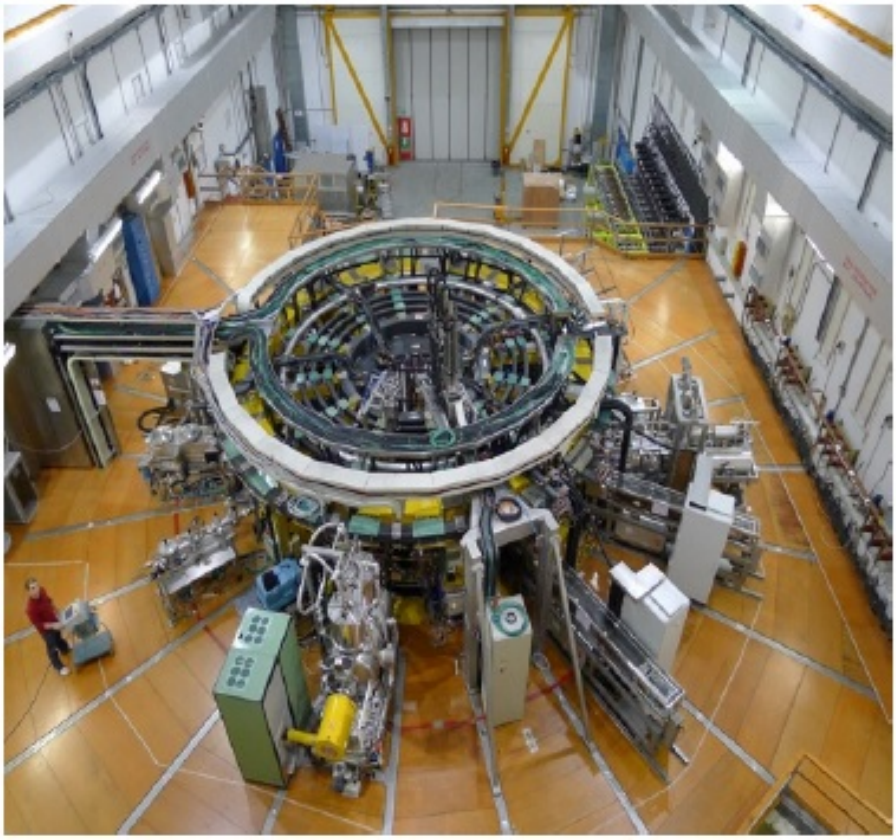

Figure 2.9: The RFX-mod device.

minor radius 25 cm and the highest achievable elongation is 2.8. This chapter gives a brief overview of issues relevant to the experiments performed on TCV, detailed information can be found in [27].

TCV was designed in order to maximize the operational flexibility [28] in terms of plasma shape and internal profiles. It is equipped with a set of 16 poloidal field coils with independent power supplies enabling various plasma shapes generation. TCV has 11 Electron Cyclotron Resonant Heating(ECRH)/Electron Cyclotron Current Drive (ECCD) gyrotrons launching the power from different positions, both on the low field side and upper side of the machine. The total power in the gyrotrons is 6.5 MW and the waves can be injected both on 2nd and 3rd X-mode harmonic frequency. Recently, a 1 MW of 35 keV neutral beam injector (NBI) has been installed. The first wall of the device is made of carbon.

TCV is also equipped with an advanced set of diagnostics. The electron temperature is measured by Thomson scattering [29] with repetition rate of 20 ms, density is determined at 20 kHz by multichord interferometer [30]. There are also several detectors measuring the soft X-ray and electron cyclotron emission.

2.5.4 ASDEX-Upgrade

The most complex and ITER-relevant (see section 2.5.5) device used during the work on this thesis is ASDEX-Upgrade operated at IPP Garching, Germany. The major radius is 1.65 m, minor radius 0.5 m and the elongation up to 1.8. The toroidal field can be ramped up to 3.1 T and the highest achievable possible plasma current is 1.6 MA. It is equipped by huge set of additional heating: 20 MW in NBI (60 and 100 keV), 6 MW in Ion Cyclotron Resonant Heating (ICRH) and 2 times 2 MW in ECRH/ECCD systems. It is equipped by an ITER-like wall made of tungsten. More information about the device can be found in [31].

Within this thesis, the capability of RAPTOR to predict disruptions on very complex device was demonstrated serving as inspiration for future work.

2.5.5 ITER

The next huge step towards a fusion reactor is a new tokamak being built in Cadarache located in the south of France. This device will be twice bigger in linear dimension than the biggest existing device, JET. The major radius will be 6.2 m, minor radius 2 m, elongation up to 1.85, toroidal magnetic field 5.3 T and plasma current 15 MA. It is expected to produce 500 MW of fusion power for at least 400 s. Present record is 16 MW for 1 s on JET. The produced fusion energy should be 10 times more than the energy input to the plasma. The image of ITER is shown in Fig. 2.10

This device is expected to demonstrate that the fusion reactor can produce sufficient amount of energy both in inductive and steady state regime with acceptable divertor heat loads due to ELMs and operate without disruptions. ITER will be also the first device heated dominantly by α particles. Another task of ITER is to study the neutron damage of the structure materials. This issue will be problematic for future reactors.

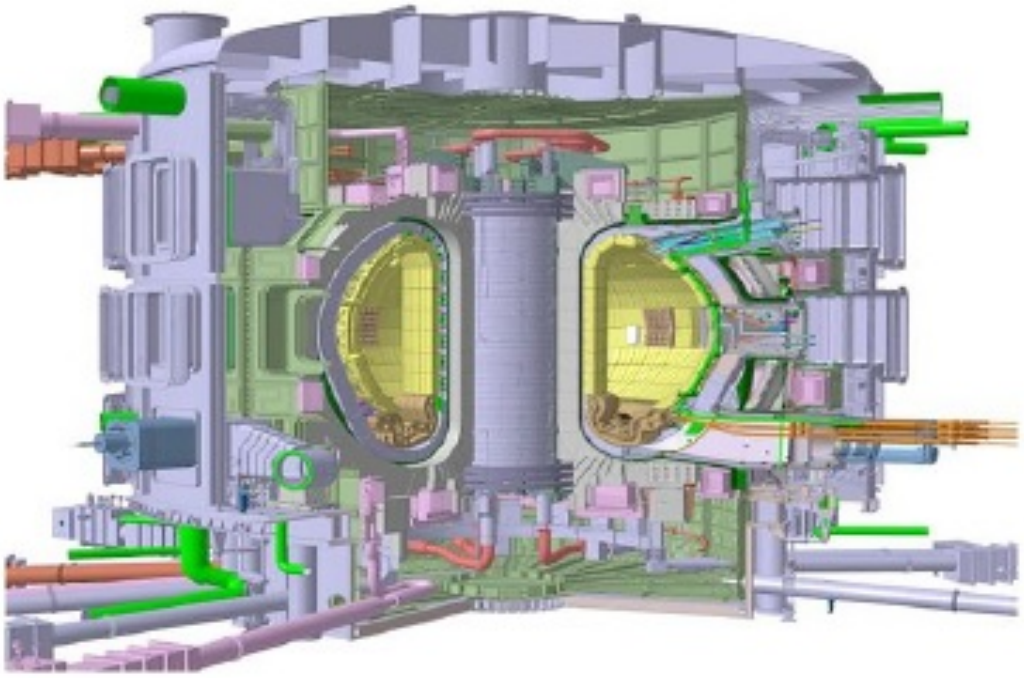

Figure 2.10: The scheme of ITER. Figure taken from [32]

Part I

Plasma Current Centroid Position Measurement on ISTTOK

CHAPTER III

Plasma Centroid Position Measurement on ISTTOK

In tokamak devices, the poloidal field coils control plasma position and shape. In air core machines, they are also used to induce the plasma current. The above mentioned quantities are usually computed using magnetic sensors. These sensors do not detect just plasma field, but also the field generated by the poloidal field coils and eddy currents induced in the passive structures of the device.

Some algorithms require the separation of different contributions for better precision. The reason is that the signal originating from currents in active coils and conductive structures can be determined by other means than the plasma signal. Consequently, the method recovering unknown plasma properties can provide better results if the known 'offset' from other sources is removed. An example of such algorithm for plasma centroid position measurement is given in [34], [35] for COMPASS. In some cases, such a procedure is applied also for equilibrium reconstruction, as for example in [36] for TCV. The effect of the passive structures is important especially for smaller devices where the discharge duration could be comparable to the time constants of the passive structures. Most of these devices are equipped with a continuous, low-conductive vacuum vessel and a highly conductive shell with several poloidal and toroidal gaps. The exact gap position and geometry is different for each device. Modelling of the currents in passive structures and their impact on the magnetic measurements is not straightforward. On the other hand, as we will show in this chapter, knowing the effect is essential in case of plasma centroid position control on ISTTOK. A detailed description of this issue by advanced numerical models is given in [37].

3.1 Model of Poloidal Field Coils and Passive Structure Signal

In this section, we will describe a simple, real time applicable method for computation of the signal originating from the eddy currents and poloidal field coils. First of all, let us introduce an important assumption that will be used later. We neglected the part of the signal generated by the eddy currents induced by plasma motion or changes in the plasma current. The reason of this assumption is that the eddy currents induced in the structures surrounding the plasma also significantly slow down the process of the plasma properties modification, thus the signal values cannot be that high. Therefore we consider that the effect of eddy currents induced by plasma has lower order of importance. Once we know the part of the signal generated by the poloidal field coils and the eddy currents, the computation of the pure plasma signal is straightforward: it is just the remaining signal on the sensor. The signal generated by the poloidal field coils circuit on a pick-up coil is the sum of the effect of the poloidal field coil current itself, the effect of eddy currents in the shell and the eddy currents in the vessel:

$$S = K_1 I_{PFC} + K_2 I_{shell} + K_3 I_{vessel} \tag{3.1}$$

where $K_{1,2,3}$ are the coupling coefficients between PFC, shell and vessel currents to the sensor. We assume that the system is far from the saturation of the transformer core so that the linearisation is still valid. The convenient representation of the system for real time implementation is the state-space model:

$$\begin{aligned} \dot{x} &= Ax + Bu \\ y &= Cx + Du \end{aligned} \tag{3.2}$$

where x is the state vector consisting of 2 components. We adopted a black-box approach, so the state vector has no physical meaning. u is the input to the model, that corresponds to the current in poloidal field coils circuit and y is the output, corresponding to the resulting signal on the pick-up coil produced by the poloidal field coils circuit and eddy currents. A is 2 x 2 matrix, B is 2 x 1 matrix, C is 1 x 2 matrix and D is 1 x 1 matrix. The components of the matrixes elements are estimated by Matlab routine *ssest* for a vacuum shot using just the selected poloidal field coils circuit.

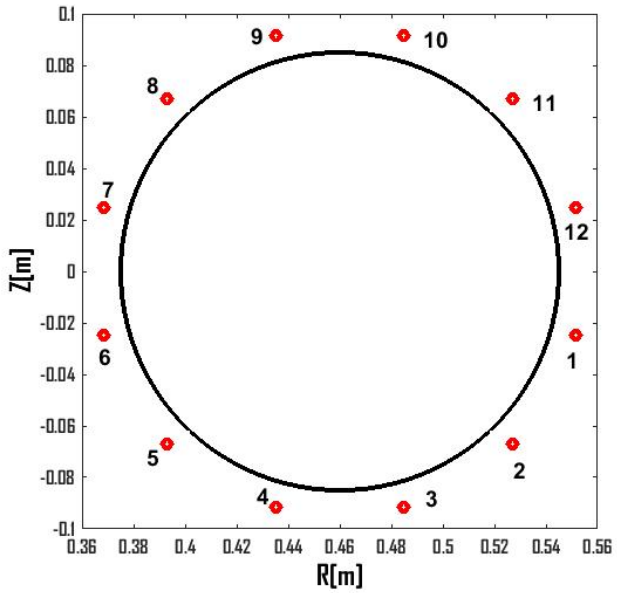

Figure 3.1: The positions of the 12 Mirnov coils (red squares) symmetrical with respect to the midplane

3.1.1 ISTTOK Results

The method was first tested on experimental data from ISTTOK. First of all, a set of dedicated vacuum discharges with rectangular current waveform in one of the poloidal field coils circuits was performed. The data from these discharges were used to identify the model introduced in 3.2. The positions of the 12 Mirnov coils symmetrical with respect to the midplane are shown in Fig. 3.1.

The results of the method for separation of plasma signal are shown in Fig. 3.2 for the vertical field circuit and in Fig. 3.3 for the horizontal field circuit. The result is always presented for Mirnov coil 1 located on the low field side, Mirnov coil 3 on the lower side, Mirnov coil 6 on the high field side and Mirnov coil 9 on the upper side of ISTTOK vessel. The results for the other sensors are comparably good. From Fig. 3.2 and Fig. 3.3, one can see that the simple model introduced in this section is sufficient to subtract most of the effect of poloidal field coils and eddy currents from the sensor signal on ISTTOK. Thus one can separate the signal generated by the plasma itself.

3.1.2 Verification on Other Devices

The method was also tested on RFX-mod data. Due to the large number of poloidal field coils, the data were provided by MAXFEA simulation [38]. MAXFEA is a finite element Grad-Shafranov equation solver that is used to design plasma discharges. This code contains information about the geometry of both poloidal field coils and passive structures of the RFX-mod. More information

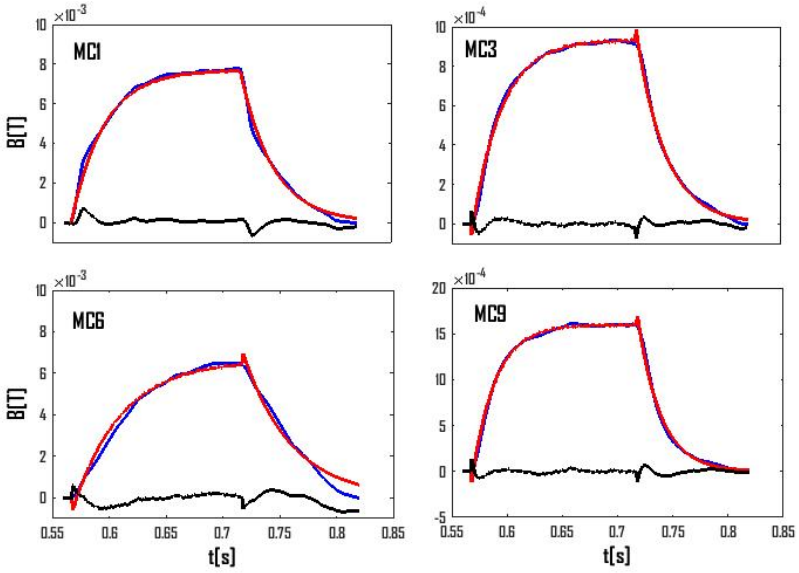

Figure 3.2: The measured signal (blue) modelled signal (red) and the remaining signal (black) on Mirnov coil 1, 3, 6 and 9 during a rectangular pulse in poloidal field coils for vertical field generation.

about the code are given later in section 4.1. As the model provides very good agreement with experiment, it can be also used to replace missing experimental data to identify the model in (3.2). For this purpose, we applied a rectangular pulse to each pair of the poloidal field coils and identified the model for each of the RFX sensor of interest (flux loops and Mirnov coils). The results are shown for Mirnov coil 1 (located on the low field side) and Mirnov coil 3 (located on the upper side of the device) in Fig. 3.4. Fig. 3.5 shows the results for flux loop 1 (located at low field side) and flux loop 4 (on the upper high field side) For the flux loop, the reference level of the magnetic flux is the flux on flux loop 6 located on the lower high field side. In both cases, we show a result for poloidal field coil number 7 that generates mainly vertical field and for poloidal field coil number 4 that creates mainly horizontal field. The result for the other sensors and other poloidal field coils are comparably good. From these figures, one can deduce that the model we have introduced is sufficiently good for separation of the signal from plasma on RFX-mod.

The method was also applied on another device, tokamak Golem in Prague. This device has similar dimensions as ISTTOK and the construction of the conductive structures of the device is similar as well: it consists of a low conductive vacuum vessel and a highly conductive copper shell with one toroidal and one poloidal gap. The problem with the current centroid position measurement is the same as on ISTTOK: magnetic signals are corrupted by the eddy currents induced in the conductive structures. A method for plasma centroid position measurement elaborated within [33]

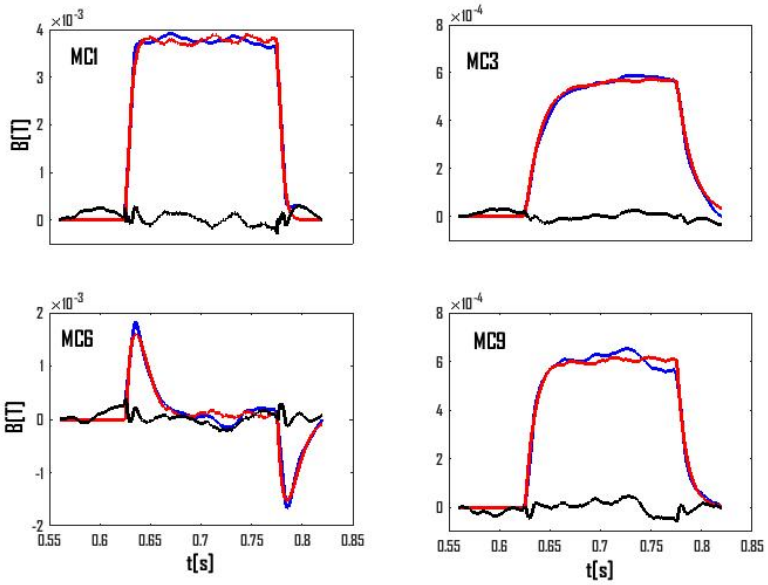

Figure 3.3: The measured signal (blue) modelled signal (red) and the remaining signal (black) on Mirnov coil 1, 3, 6 and 9 during a rectangular pulse in poloidal field coils for horizontal field generation.

fails in the plasma radial position estimate after the current in radial equilibrium circuit is changed. The method described within this chapter was applied to clean the signal on sensor measuring the mean vertical field. This entry is required by the method in [33] and the diagnostic consists of 4 flux loops, the first located in upper low field side, second in lower low field side, third upper high field side and the last on lower high field side.

The signal on this sensor combination in presence of a pulse in radial equilibrium field circuit is shown in Fig. 3.6. One can see very good agreement between the measured and simulated field. The remaining signal originating from the radial equilibrium field circuit and the corresponding eddy currents is almost vanished.

3.2 ISTTOK Current Centroid Position Measurement

Let us discuss the application of the algorithm described in previous section on the current position estimate on ISTTOK. There are several existing methods for either plasma equilibrium reconstruction such as LIUQE [36], EFIT in [39] or simplified semi-analytical methods for the plasma boundary computation such as Equivalent Currents [40], Toroidal Harmonics [41] or Local Field Expansion [42]. As ISTTOK is a very small device just with circular plasma and limited amount of actuators, the measurement and control of the current centroid presented below appears to be fully sufficient. As the signal on the magnetic sensors has been corrupted by the eddy currents especially

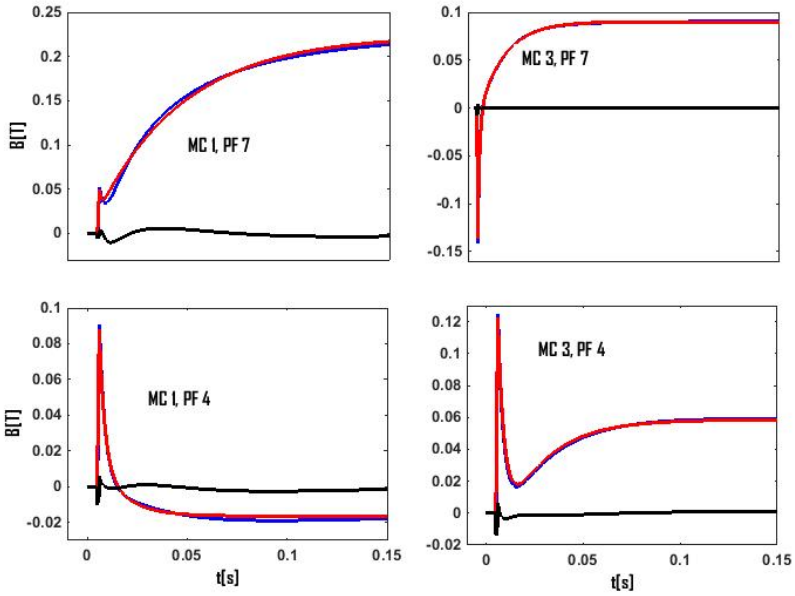

Figure 3.4: The measured signal (blue) modelled signal (red) and the remaining signal (black) on Mirnov coil 1 and 3 and for pulse in poloidal field coil number 7 (used for vertical field generation) and for poloidal field coil 4 (used for radial field generation).

after the plasma current reversal, the plasma centroid position measurement has not been performed by magnetic diagnostics, but by Langmuir probes. In this section, we will introduce a simple method for plasma centroid position measurement and show that the method provides meaningful results in case that the magnetic signals are cleaned from the contribution of the poloidal field coils and eddy currents induced in the conductive structures.

3.2.1 Current Centroid Measurement by Magnetics

In this part, the plasma centroid position will be estimated using cylindrical geometry approximation (which is reasonable given the very high aspect ratio of ISTTOK). Another assumption we will use is that the plasma shifts are small compared to the minor radius of the vessel. This is not always true, but it is sufficient for the first demonstration. In cylindrical geometry, the magnetic field of a straight conductor (corresponding to the poloidal field in tokamak) can be computed by

$$B = \frac{\mu_0 I_p}{2\pi(r_v - \delta)} \tag{3.3}$$

where r_v is the minor radius and δ is the shift of the plasma current centroid towards the sensor. Let us assume that we have four measurements of the poloidal magnetic field, B_1 on the low field side, B_2 on the high field side, B_3 on the upper side of the tokamak and B_4 on the lower side. We

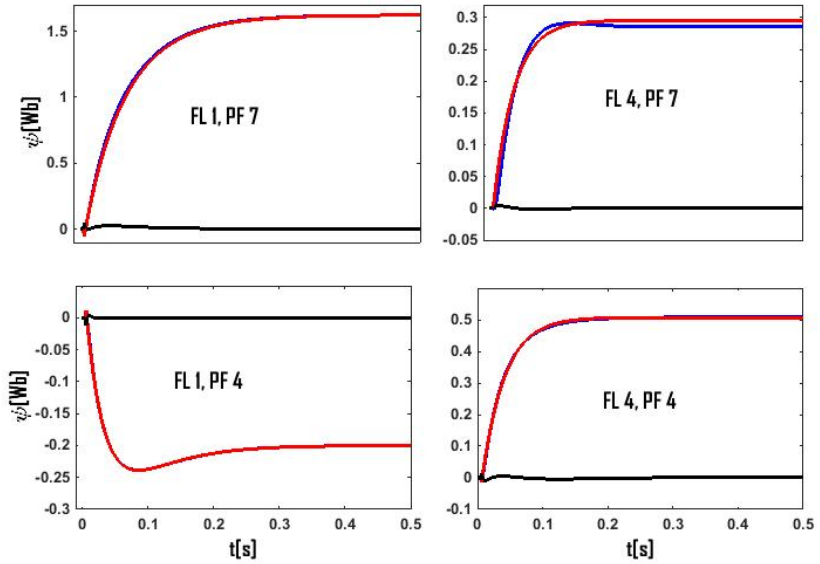

Figure 3.5: The measured signal (blue) modelled signal (red) and the remaining signal (black) on flux loop 1 and 4 and for pulse in poloidal field coil number 7 (used for vertical field generation) and for poloidal field coil 4 (used for radial field generation).

use the ratio of B_1 and B_2 to recover the plasma radial shift δ_r and the ratio of B_3 and B_4 to recover the plasma vertical shift δ_z. Using (3.3) for small shifts, we obtain

$$\delta_r = r_v \frac{B_1/B_2 - 1}{B_1/B_2 + 1} \tag{3.4}$$

$$\delta_z = r_v \frac{B_3/B_4 - 1}{B_3/B_4 + 1} \tag{3.5}$$

In radial direction, positive shift is considered the shift outwards. On ISTTOK, as one can see in Fig. 3.1 the measurements located directly on the midplane or on the uppermost, lowermost vessel position are not available. Thus, we consider B_1 equal to the average of the field on sensor 9 and 10 and B_2 is the average field on sensor 3 and 4. Similarly, B_3 is equal to the average field on sensor 1 and 12, B_4 is the average field on sensor 6 and 7. As we will show later, this simple method is sufficient to provide an estimate of plasma centroid position. In vertical direction, also a comparison with the Heavy Ion Beam Diagnostics (HIBD) will be done.

3.2.2 Vertical Position Measured by Heavy Ion Beam

The HIBD at ISTTOK [21],[22] is able to measure the profiles of temperature, density, plasma current and plasma potential. Currently, the HIBD, using Xenon ions, is configured to measure

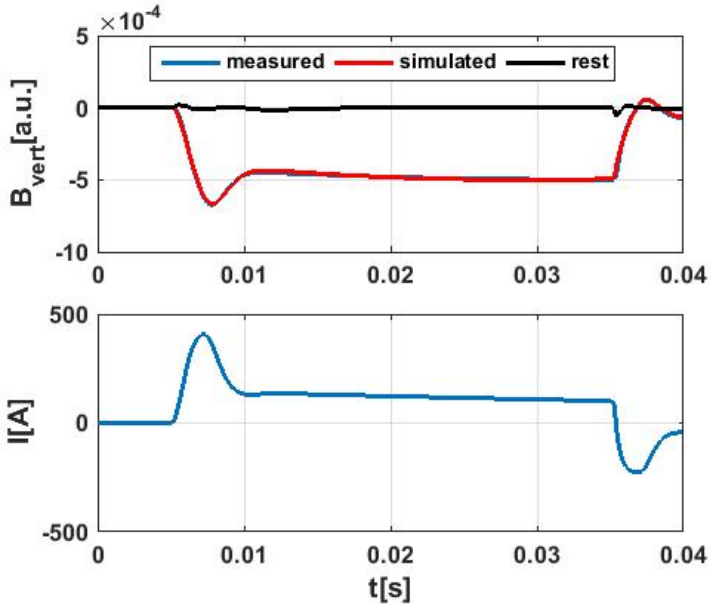

Figure 3.6: The time evolution of current in the vertical field circuit and the field detected by the sensor for vertical field estimation in a vacuum shot. The measured and simulated signal are almost overlapping.

the $n_e\sigma_{eff}(T_e)$ profile. $n_e\sigma_{eff}(T_e)$ is a convoluted measurement of the electron density (n_e) times the effective ionizations cross-section ($\sigma_{eff}(T_e)$) for the single to double ionization process, $Xe^{+} \rightarrow Xe^{2+}$. $\sigma_{eff}(T_e)$ is a known function monotonically increasing with the electron temperature (T_e) for the typical ISTTOK electron temperature ranges (up to core temperature 200 eV). In this way, the $n_e\sigma_{eff}(T_e)$ product can be regarded as a proxy for the plasma pressure. The HIBD performs measurements in 12 sample volumes (1cm length each) along the primary beam trajectory inside the plasma obtaining a profile between $-0.7a$ and $0.7a$. The primary beam trajectory in the region of measurements can be considered as a straight line in the vertical direction. Since HIBD is measuring a "pressure-like" profile along a vertical line, it is possible to recover the plasma vertical position assuming that it is directly related to the plasma pressure. The method used here to recover the plasma vertical position from HIBD data is to calculate the centroid through the "centre of mass" of the $n_e\sigma_{eff}(T_e)$ profile:

$$\delta_z = \frac{1}{\sum_j n_e(j)\sigma_{eff}(j)} \sum_j n_e(j)\sigma_{eff}(j)z(j) \tag{3.6}$$

where z_j is the vertical position of the sample volume j. This plasma position calculation method uses the whole profile for determining the vertical position. Because of that, it is expected that the variations of the centroid position have lower amplitude than the variations of the plasma centre (the maximum of the pressure).

3.2.3 Experimental Results

In this section, we will show the results of ISTTOK current centroid position measurement and demonstrate the necessity of subtraction of the signal originating from the poloidal field coils and eddy currents in passive structures. First of all, let us compare plasma position estimated by the heavy ion beam with the plasma vertical position estimated by magnetic diagnostics with and without subtraction of the signal from poloidal field coils and eddy currents. As the estimates by the magnetic and by the HIBD are of different nature, we can compare just the dynamic behavior: both estimate families are normalized with respect to the highest displacement measured by given method. The normalization factor for both magnetic methods is the highest displacement when the eddy current and poloidal field coil effect is subtracted. In Fig. 3.7, one can see that the estimate by magnetic diagnostic without subtraction of eddy currents and poloidal field coils effect gives unrealistic results. The estimated centroid shift a few ms after the current reversal are more than 50% of the minor radius of the vessel and the plasma current is already in the flat-top phase. Such plasma cannot be stable and would immediately disrupt. The peaks in vertical position are significantly decreased if the effect of eddy currents and poloidal field coils is subtracted. One can also see decent agreement of the currrent centroid relative vertical displacement with the relative vertical displacement measured by the HIBD.

For the radial position, there is no independent reliable measurement. Therefore we compare the estimated plasma radial position normalized in the same way as for the vertical position during perturbations induced by vertical magnetic field. An example of such a shot is in Fig. 3.7. In this shot, one can see that the estimated plasma position follows the trends of the current in the vertical field circuit. As in the previous case, the result using signal without removal of the eddy currents and poloidal field coils effect gives some unrealistic peaks after the current reversal. In absolute numbers, the highest radial shift in the current flat-top phase is 2.8 cm for the signal without eddy current and poloidal field coils effect and 4.2 cm for the other signal. The effect of eddy currents and poloidal field coils subtraction is much less important than for the vertical position, but it must be taken into account anyway. In this section, we have shown that for the plasma current centroid position measurement the subtraction of the effects of poloidal field coils and eddy currents is essential. The estimate for both radial and vertical position is realistic and at least the trends appear to be correct.

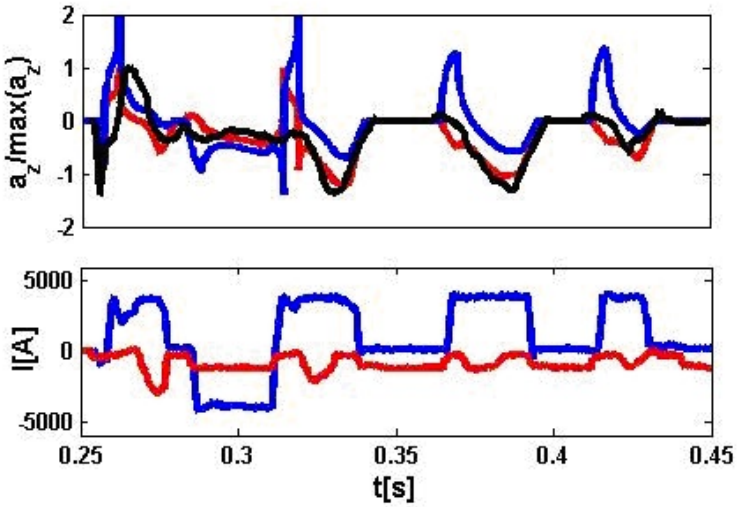

Figure 3.7: Upper plot: plasma current centroid vertical position from magnetic diagnostics without subtraction of the signal from eddy currents and poloidal field coils (blue), with this subtraction (red) and from the HIBD (black). Magnetic results are normalized to the highest displacement of the position determined from signals without the effect of eddy currents and poloidal field coils (red curve); the HIBD is normalized by the highest displacement detected by the HIBD. Lower plot: plasma current (blue) and the current in horizontal field circuit (red) multiplied by 20 for better visual resolution for shot 38445.

3.3 Alternative Method for Plasma Centroid Position Estimate

The method of plasma centroid position measurement by magnetics presented in section 3.2.1 has several disadvantages: it does not take into account the real toroidal geometry of the plasma and one needs to assume that the plasma shifts are small compared to the minor radius of the vessel. It was used due to poor precision of the calibration of the Mirnov coils. The Mirnov coils are expected to be re-calibrated in near future. This will open an opportunity to use more advanced technique for plasma centroid position measurement. This section proposes one of the possibilities. The same principle is used on COMPASS in more advanced geometry [34], [35].

In this method, the plasma current density j is approximated by:

$$j(\delta) = j(0)\left(1 - \frac{\delta^2}{r_v^2}\right)^{\nu} \tag{3.7}$$

where δ is the distance from the current centroid, r_v is the minor radius of the plasma and ν is the peaking factor. Using this profile, we assume that the current profile deformation caused by plasma pressure and internal inductance is negligible. This is acceptable, as shown in [34] for COMPASS. As COMPASS is an H-mode tokamak, one can reasonably assume that the effect of plasma pressure on current distribution will be higher than on ISTTOK. Thus, application of this method on ISTTOK

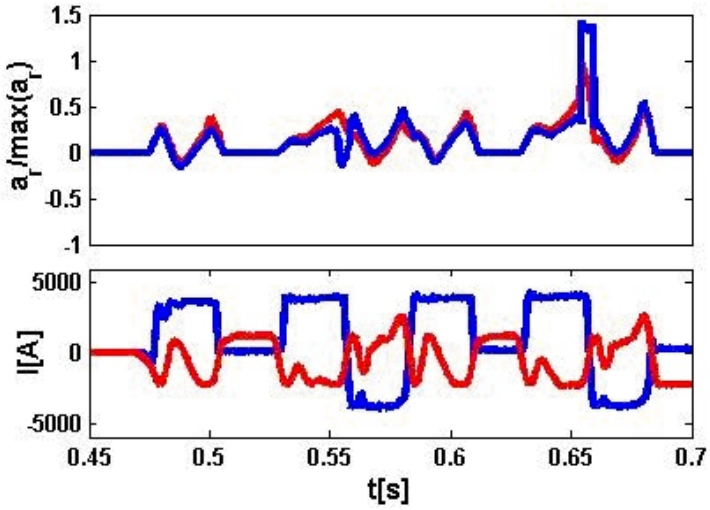

Figure 3.8: Upper plot: plasma current centroid radial position from magnetic diagnostics without subtraction of the signal from eddy currents and poloidal field coils (blue) and with plasma signal separation (red). The results are normalized to the highest displacement of the position determined from signals without the effect of eddy currents and poloidal field coils (red curve). Lower plot: plasma current (blue) and the current in vertical field circuit (red) multiplied by 10 for better visual resolution for shot 38442.

is meaningful. In this method, we place the plasma centre to various locations in the vessel and calculate the signal on each Mirnov coil generated by a unit plasma current. As ISTTOK operates just in limiter regime, minor radius is given by the distance between the plasma centre (the position is given) and the nearest limiter point. In ISTTOK, limiter is defined by the carbon tiles located at radius 8.5 cm from the vessel centre. Afterwards, $j(0)$ is computed to conserve the plasma current: as the signal generated by the unit current is computed, the plasma current value must be conserved regardless the plasma centroid position. There is always some uncertainty in the peaking profile of the plasma current. The value might change from one discharge to another. To deal with this, we performed the computation for $\nu = 3$ and $\nu = 5$. We expect that the current profile will be within the limits given by these two peaking factors. In addition, as we show later, the impact of this parameter is not very significant, so even if the real current profile is outside the limits, it should not cause significant errors.

Finally, once the plasma centroid is placed in the vessel and the current profile is constructed, we compute the signal on each of the 12 pick-up coils using Biot-Savart law. Afterwards, we find two combinations of the signals, one to recover the plasma centroid position in radial direction and one in horizontal direction. The radial position is recovered from the following signal combination

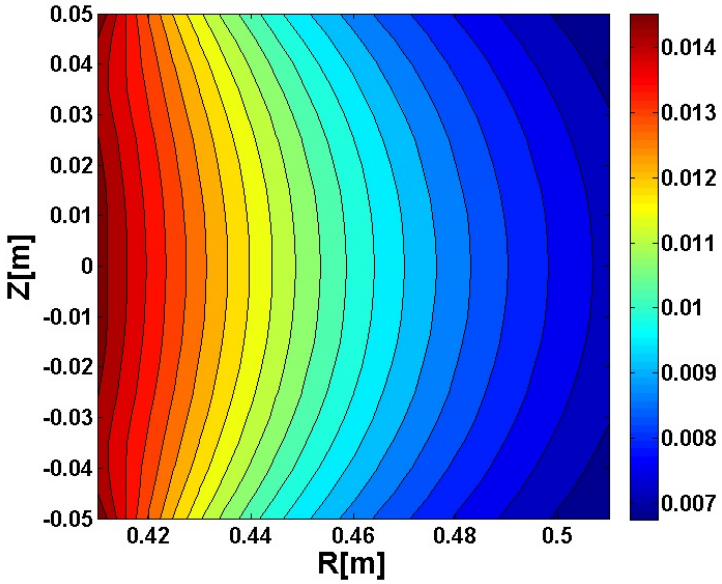

Figure 3.9: The signal measured by the combination of the pick-up coils used for radial position determination as a function of radial and vertical position of the plasma centre for $\nu = 3$.

(the subscript of signal S denotes the pick-up coil number):

$$S_R = S_6 + S_7 + 0.8(S_5 + S_8). \tag{3.8}$$

The vertical position is recovered from

$$S_V = S_9 + S_{10} - (S_3 + S_4) + 0.5(S_8 - S_5). \tag{3.9}$$

The used pick-up coils and corresponding weight coefficients were chosen in order to maximize the sensitivity of S_R resp. S_V for radial resp. vertical position and minimize its sensitivity for vertical, resp. radial position. The contour plot of the signal for the radial position from (3.8) is in Fig. 3.9 and the one for the vertical position (3.9) is in Fig. 3.10.

One can see that the signal measured by the combination in Fig. 3.8 is dependent mostly on the radial position of the plasma and the signal measured by the combination in Fig. 3.9 depends mostly on the vertical position of the plasma. Having the combination of these two measurements, the plasma position can be recovered using the look-up table as on COMPASS device [34], [35].

Let us also discuss the effect of the plasma current profile on the result of the reconstruction. Same plots as Fig. 3.8 and Fig. 3.9 were computed for $\nu = 5$. To see the difference, we compared the estimated radial position with vertical position fixed and estimated vertical position with fixed

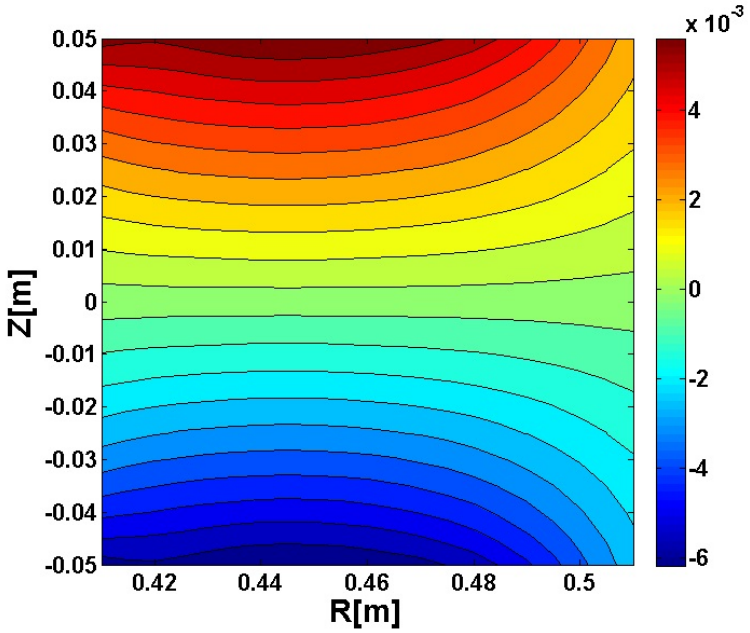

Figure 3.10: The signal measured by the combination of the pick-up coils used for vertical position determination as a function of radial and vertical position of the plasma centre for $\nu = 3$.

radial position for $\nu = 5$ and $\nu = 3$. The difference is negligible as shown in Fig. 3.11 for radial position. One can see that the modification in current profiles do not perturb the results of the method.

3.4 Conclusion and Outlook

This section introduces an algorithm for separation of the plasma signal and the signal generated by the currents in the passive structures and poloidal field coils. It was shown that such a separation is essential for obtaining reliable measurement of plasma position. Such a separation enables the plasma centroid position measurement by magnetic diagnostics on ISTTOK. This method is more precise and reliable than the present method using Langmuir probes. It will open new space for extended physical analysis of ISTTOK data and as the method is suited to be implemented in the real time control system, it is expected to improve the feedback control of the ISTTOK plasma position. After the calibration of the magnetics is improved, a new method of plasma centroid position measurement proposed in this section can be used.

The method for the eddy current and poloidal field coil effect subtraction is general and can be easily transferred to another device, as we have shown on the example of the RFX-mod. Presently, the algorithm for subtraction of the eddy current and poloidal field coils contribution is being used

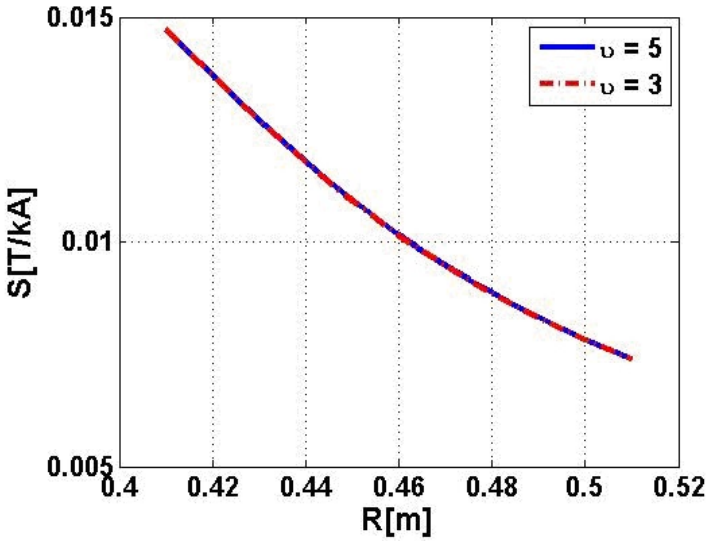

Figure 3.11: The estimated radial position of the plasma centre (vertical position fixed at Z = 0) for $\nu = 5$ and $\nu = 3$.

to improve the measurement of the plasma centroid position on Golem tokamak located in Prague, Czech Republic.

Part II

Plasma Equilibrium Monitoring in RFX-mod Tokamak Regime

CHAPTER IV

Boundary Reconstruction in RFX-mod Tokamak Regime

In the previous chapter III, the elementary layer of measurement of quantities needed for tokamak plasma feedback control was described. However, such a basic control is not satisfactory for larger devices such as RFX-mod. In these devices, the discharges are longer and the heat fluxes on the first wall higher, therefor there is high risk of the first wall damage. Due to these restrictions, it is essential to know the location of the plasma energy deposition. The only way to do this is to measure in real time and feedback control the plasma boundary. The precise knowledge of the plasma boundary is also a crucial requirement for reliable computation of plasma macroscopic parameters. A method of plasma boundary reconstruction developed within this thesis is presented in this chapter and the evaluation of plasma parameters using the reconstructed plasma boundary is described in next chapters.

In present machines, several methods have been developed for the equilibrium reconstruction. The equilibrium can be inferred from iterative methods based on the solution of the Grad-Shafranov equation (2.5) and best fitting of equilibrium quantity measurements. Some algorithms based on this principle are EFIT [39], used for example in DIII-D [43], JET [44] and LIUQE used in TCV [36]. Basic description of LIUQE is given in Appendix B. Another method is based on estimating the magnetic field in the vacuum and imposing the Cauchy condition on the plasma boundary. The general principles of the latter method are explained in [46] and applications are reported in JT-60U [47], in Tore Supra [48], in FTU [41] and several other devices [40], [42]. In RFX-mod the original boundary reconstruction algorithm belonged also to the second group and it was applicable only to quasi-circular plasmas [49]. As shaped and diverted tokamak experiments started in 2011, a new method for both real time and offline plasma boundary reconstruction was required. Due to the limited number of magnetic sensors along the poloidal direction, none of the existing methods are directly applicable. Thus a significant extension of the original algorithm was developed, with a

view for its implementation in the RFX-mod real-time control system, which works at a sampling frequency of 5 kHz [54]. Preliminary work was presented in [50] and in [51]. The final version based on [52] with the latest results is presented here.

4.1 MAXFEA code

For offline estimation of the plasma shape and macroscopic quantities, a finite element Grad-Shafranov solver, MAXFEA [53], is routinely used in RFX-mod [38] with given pressure and plasma current profile. Other code inputs are the plasma current, the PFS currents and the magnetic axis position. The outputs are the plasma boundary, the poloidal flux surface map and the value of poloidal magnetic field and poloidal magnetic flux at any position.

The code can be operated in either static equilibrium mode, used for plasma shape design, or evolutive equilibrium mode, used to test the plasma control system performance and to estimate the effect of the conducting structures on the field penetration.

In this thesis, MAXFEA was used as a benchmark for the proposed algorithm.

4.2 Poloidal flux and magnetic field extrapolation in vacuum

The determination of the plasma boundary is based on the extrapolation of the poloidal magnetic flux ψ and magnetic field $\mathbf{B}$ in the vacuum region inside the sensors. Adopting the pseudo-toroidal coordinates (r, θ, ϕ), being r the distance from the vessel centre, and θ, ϕ respectively the poloidal and toroidal angles, the extrapolation technique exploits a hybrid toroidal-cylindrical formalism. In fact, the relationship between ψ and $\mathbf{B}$ proper of the axisymmetric toroidal geometry ($\frac{\partial}{\partial \phi} = 0$) is used (see equation (4.1) below), but the magnetic field poloidal harmonics are given the radial dependence imposed by Maxwell's vacuum equations in cylindrical geometry. As shown by the analysis presented in Fig. 4.1 and discussed later in this section, this approximation is accurate enough, given the relatively low inverse aspect ratio a/R_0 of RFX-mod. Moreover, it allows the derivation of analytic extrapolation formulas, suitable to be implemented in a real-time control system. Finally, it is an improvement of the technique operating in RFX-mod since 1997 [49] for standard circular plasmas, which instead considered constant with r the θ-dependent harmonic component of B_θ.

The starting point is the axisymmetric representation of $\mathbf{B}$ in terms of the poloidal flux:

$$\mathbf{B} = \frac{1}{2\pi R(r,\theta)} \nabla\psi \times \mathbf{e}_\phi + B_\phi \mathbf{e}_\phi, \tag{4.1}$$

where $R(r,\theta) = R_0 + r \cdot cos(\theta)$ and $\mathbf{e}_\phi$ is the unit vector in the toroidal direction. Using a left-handed co-ordinate system like the RFX-mod one, (4.1) gives the following relations:

$$B_r = \frac{-1}{2\pi r R(\theta)} \cdot \frac{\partial \psi}{\partial \theta} \tag{4.2}$$

$$B_\theta = \frac{1}{2\pi R(\theta)} \cdot \frac{\partial \psi}{\partial r}. \tag{4.3}$$

The knowledge of ψ at any angle θ at the sensor radius r_ψ is obtained from the 8 flux measurements, and from the PFS currents. As explained in section 4.4, the flux measurements allow the determination of the first three poloidal harmonics, whereas the PFS currents allow the estimate of further higher poloidal harmonics, which are necessary both to correctly reconstruct the plasma boundary and to remove the aliasing effect in the first three harmonics. Then, the value $\psi(r_\psi, \theta)$ is extrapolated at radii $r < r_\psi$ by integration of (4.3):

$$\psi(r,\theta) - \psi(r_\psi,\theta) = \int_{r_\psi}^{r} 2\pi R(\rho,\theta) B_\theta(\rho,\theta) d\rho \tag{4.4}$$

To perform this integration, knowledge of B_θ in the considered vacuum region is required. As explained above, we adopt the approximation represented by the standard expressions for the vacuum magnetic field in cylindrical geometry, constrained by the measurements at the sensor radius r_B. These expressions stem from the Laplace equation for the magnetic scalar potential [46], [55]:

$$\begin{aligned} \mathbf{B} &= \nabla \Phi \\ \Delta \Phi &= 0, \end{aligned} \tag{4.5}$$

whose solution in cylindrical geometry admits an expansion in poloidal harmonics (we assume $\partial/\partial\phi = 0$), plus a non-periodic term:

$$\Phi(r,\theta) = \Phi_0 \theta + \sum_{m=1}^{\infty} \Phi_c^m(r,\theta) + \Phi_s^m(r,\theta), \tag{4.6}$$

$$\Phi_c^m = (A_c^m r^m + B_c^m r^{-m}) \cdot cos(m\theta) \tag{4.7}$$

$$\Phi_s^m = (A_s^m r^m + B_s^m r^{-m}) \cdot sin(m\theta). \tag{4.8}$$

Derivation of this solution is given in Appendix A. The radial dependence of the poloidal harmonics of B_θ is readily obtained from (4.5):

$$\begin{aligned} B^m_{\theta;c} &= mA^m_s r^{m-1} + mB^m_s r^{-m-1}; m \neq 0 \\ B^m_{\theta;s} &= -mA^m_c r^{m-1} - mB^m_c r^{-m-1}; m \neq 0 \\ B^0_\theta &= \frac{\Phi_0}{r}; m = 0 \end{aligned} \tag{4.9}$$

Likewise, the poloidal harmonics of B_r, knowledge of which is required, as we shall see, to determine the plasma boundary in the X-point configuration, are

$$B^m_{r;c,s} = \frac{\partial \Phi^m_{c,s}}{\partial r} = mA^m_{c,s} r^{m-1} - mB^m_{c,s} r^{-m-1}; m \neq 0. \tag{4.10}$$

The unknown coefficients Φ_0, A^m_c, A^m_s, B^m_c, B^m_s are obtained by matching formulas (4.9) and (4.10) to the experimental harmonics. As done for the flux, the poloidal harmonics of B_θ are estimated at r_B by combining the 8 pick-up coils signals and the high-order harmonics produced by the field shaping coils. The poloidal harmonics of B_r are obtained at r_ψ from the knowledge of $\psi(r_\psi, \theta)$ by means of equation (4.2). In particular, due to the angular dependence of the factor $1/R(r,\theta)$, it is convenient to re-arrange (4.2) in the following way:

$$\begin{aligned} B_r &= \frac{-1}{2\pi r R_0}\left(\frac{\partial \hat{\psi}}{\partial \theta} - \tilde{\psi}\right), \\ \hat{\psi} &= \frac{R_0}{R(r,\theta)}\psi \\ \tilde{\psi} &= \frac{r R_0 sin(\theta)}{R^2(r,\theta)}\psi \end{aligned} \tag{4.11}$$

The experimental harmonics are simply given by

$$\begin{aligned} B^m_{r;c} &= -\frac{1}{2\pi r R_0}\left(m\hat{\psi}^m_s(r_\psi) - \tilde{\psi}^m_c(r_\psi)\right) \\ B^m_{r;s} &= \frac{1}{2\pi r R_0}\left(m\hat{\psi}^m_c(r_\psi) - \tilde{\psi}^m_s(r_\psi)\right) \end{aligned} \tag{4.12}$$

The quantities $\hat{\psi}$ and $\tilde{\psi}$ are obtained by multiplication of the flux and geometrical factors. Following this procedure ψ, B_θ, and B_r are extrapolated from the sensors location into the innermost vacuum region. The radial dependence of the magnetic field is expressed by elementary power functions,

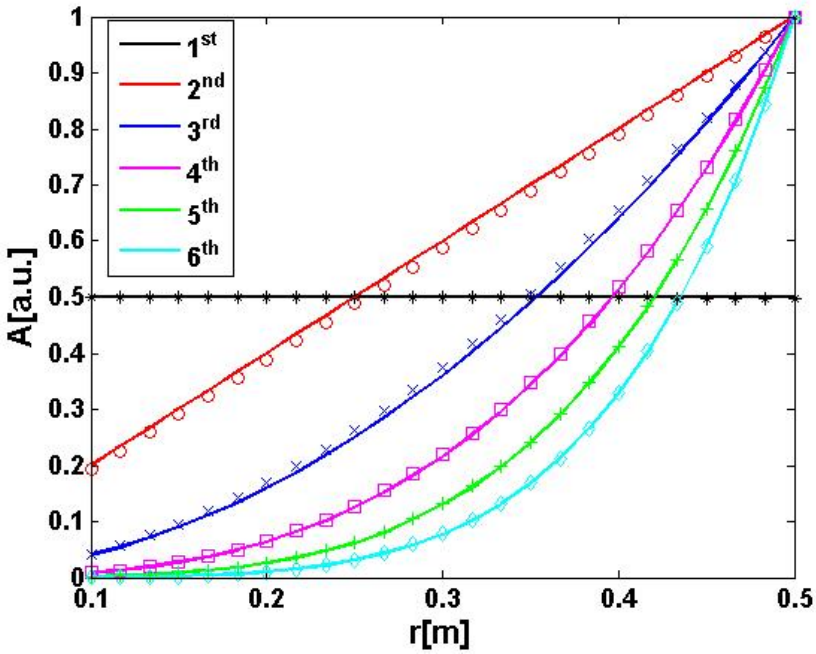

Figure 4.1: Comparison of the radial dependence of the first 6 harmonics of B_θ computed by elliptic integrals (markers) and the estimated radial dependence given by eq. (4.9) (solid lines). Figure taken from [52].

which allow performing analytically the integration in (4.4). This radial dependence is proven to be justified for the RFX-mod geometry as the following analysis will show.

To this purpose the vacuum B_θ, and B_r produced by the PFS currents have been computed at equally spaced poloidal angles along different circumferences with radius $0.1m \leq r \leq r_B$, by using the standard elliptic integral formulas [56] for the magnetic field generated by a circular current loop. This allows the determination of the radial dependence of the poloidal harmonics of B_θ, B_r in toroidal geometry, though in a case without plasma. This dependence has been compared with the prediction of the cylindrical formulas (4.9), (4.10) constrained by the measurements (virtual in this case). The results for B_θ are displayed in Fig. 4.1, considering the $m = 1 - 6$ harmonics, which, as we shall see later, are those required for good reconstruction of the plasma boundary in the more demanding cases, such as the X-point configurations. The excellent agreement of the two estimates (for B_r the result is the same) ensures that the adopted cylindrical dependence approximation for the magnetic field harmonics is accurate enough in the RFX-mod geometry. However, the approximation would not work for very low aspect ratio devices- for example for R/a below 2, the cylindrical approximation presented in this section would not be satisfactory anymore.

4.3 Plasma boundary reconstruction

In this section, the knowledge of extrapolated B_θ, B_r, and ψ in the vacuum will be used to compute the plasma boundary coordinates. The plasma boundary is defined as the last closed poloidal flux surface that does not intersect the first wall. We will show that the hybrid cylindrical-toroidal method for determining the fields in vacuum, described in the previous section, is well suited to accomplish this task. In subsection A the procedure to determine the plasma boundary is described in both limiter and X-point configurations. In subsection B the computation of the plasma boundary coordinates is performed using a large number of virtual measurements provided by different MAXFEA simulations. The comparison between the plasma boundaries reconstructed by this method and by MAXFEA allows validation of the algorithm and determination of the minimum number of harmonics required to achieve a satisfactory agreement.

4.3.1 Plasma boundary in limiter and X-point configurations

In the limiter regime, ψ_b is the maximum flux at the graphite tile radius. By using equation (4.4) the measured fluxes (8 in the real case, much more in the virtual case) are extrapolated at the first wall. Then the maximum extrapolated value and its two adjacent values along the poloidal direction are interpolated by a parabolic spline, whose maximum is considered as ψ_b . In the diverted regime, ψ_b is the flux value at the X-point, whose position must be determined. The X-point position also defines the operating regimes: X-point outside the vessel indicates the limiter regime, while inside the vessel and with the flux higher than the maximum flux at the first wall indicates the diverted regime. Two conditions hold at the X-point:

$$B_\theta = B_r = 0. \tag{4.13}$$

These two conditions form a set of two equations whose unknowns are the X-point (r, θ) coordinates. However, solving this system in the whole vacuum region is computationally too exhaustive. Thus, the following simplification was implemented: as the position of the X-point is approximately fixed by the discharge setting up, both radial and poloidal magnetic field are computed at a regular grid of 6 x 6 points covering a square of 15 x 15 cm around the expected X-point location. The grid parameters were selected to provide sufficient computational speed, precision and reliability. Since the grid points are fixed, most of the time consuming functions (sines, cosines) can be pre-calculated. The pre-calculation has to be performed again just in case that the discharge properties

are significantly modified (for example a change from upper to lower X-point). Using this grid, both B_r and B_θ are approximated by a quadratic form

$$B^*_{\theta,r} = a_{\theta,r}R^2 + b_{\theta,r}Z^2 + c_{\theta,r}RZ + d_{\theta,r}R + e_{\theta,r}Z + f_{\theta,r}, \tag{4.14}$$

where R and Z are the Cartesian coordinates on a poloidal section. The coefficients in (4.14) are found using the least squares method for both B_r and B_θ. The least squares method is implemented as a computationally efficient matrix multiplication. The set of equations (4.13) in the form of (4.14) has 4 analytic solutions. The solution located inside the initial grid is considered the X-point. If all solutions are located outside that region, the plasma is considered to be in the limiter regime. As ψ_b is known, the plasma boundary coordinates (r, θ) can be found by solving equation (4.4) for the upper extreme of the integral on the right hand side at various θ, with the left hand side equal to ψ_b - $\psi(r_\psi, \theta)$. To this purpose a Newton-Raphson method is exploited.

4.3.2 Comparison with MAXFEA

The equilibrium code MAXFEA allows the introduction of an arbitrary number of virtual pick-up coils and virtual flux loops at the same radii of the measurements of the experimental device. We considered 100 virtual measurements of both magnetic field and flux to estimate their poloidal harmonic spectra. In Fig. 4.2, the $\hat{\psi}$ harmonics are shown in a logarithmic scale for a MAXFEA simulation of a single null discharge. This configuration in fact is the richest in harmonic content (in this figure the plasma contribution to the spectrum and the spectrum calculated from a subset of 8 measurements corresponding to the positions of the real ones are also plotted; they both will be discussed in the next section). The results for B_θ, $\tilde{\psi}$ are comparable. It can be appreciated that only the first 6 harmonics are important: all higher harmonics are at least by factor of 4 lower than the 6^{th}. Therefore, we infer that this is the minimum number of harmonics needed to reconstruct the magnetic field and flux with satisfactory accuracy, within the proposed algorithm. The results of the full boundary reconstructed from the MAXFEA 100 virtual measurements (static equilibrium mode) are presented for different plasma configurations in Fig. 4.3, 4.4 and 4.5 (along with those obtained with the 8 experimental measurements, which will be commented later). The difference between the MAXFEA and the reconstructed boundaries is lower than 3 mm for all studied cases. The difference is higher just in the case of double null discharge (Fig. 4.4) in the region of lower X-point. The reason of this difference is likely due to the MAXFEA mesh density in the X-point

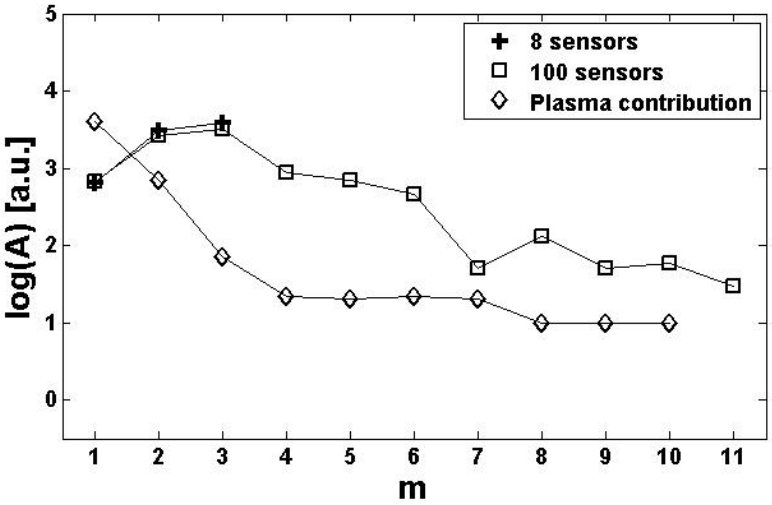

Figure 4.2: Poloidal harmonics of $\hat{\psi}$ in logarithmic scale computed from a MAXFEA simulation of a single null plasma discharge. Different number of virtual sensors are considered for the harmonic calculation and the plasma contribution is highlighted. Figure taken from [52].

regions. As the flux profile is flat around the X-point, a minor error in the flux calculation leads to a large difference in the boundary estimate. To deal with this, a much denser mesh would be needed, but it would lead to a significant increase of the computation time.

4.4 Removing aliasing effect from the harmonics computation and higher harmonics estimate

In order to apply the boundary reconstruction technique described in the previous paragraph, all the six relevant harmonics need to be determined from the real set of sensors in RFX-mod: 8 pick-up probes and 8 flux loops. The standard approach, which corresponds to using a number of sensors at least twice that of the highest relevant harmonic cannot be applied in RFX-mod shaped plasmas, because the harmonics order extends beyond the Nyquist limit. We have developed a method to determine the relevant harmonics, which complements the insufficient sensors information with the additional measurements of the PFS currents. This method is similar to the sidebands de-aliasing algorithm used for tearing mode control in RFX-mod [57].

When the harmonic content extends beyond the Nyquist frequency, not only is the measurable spectrum truncated at this limit, but it is also affected by a systematic error due to the aliasing produced by the harmonics above the Nyquist frequency. In fact, each "measured" harmonic m_{low} (0,1,2,3 for 8 sensors) is the sum of the m_{low} "true" harmonic plus an infinite series of sidebands $m' = |m_{low} + jM|$ where j is a signed integer and M is the number of sensors. In practice, only the

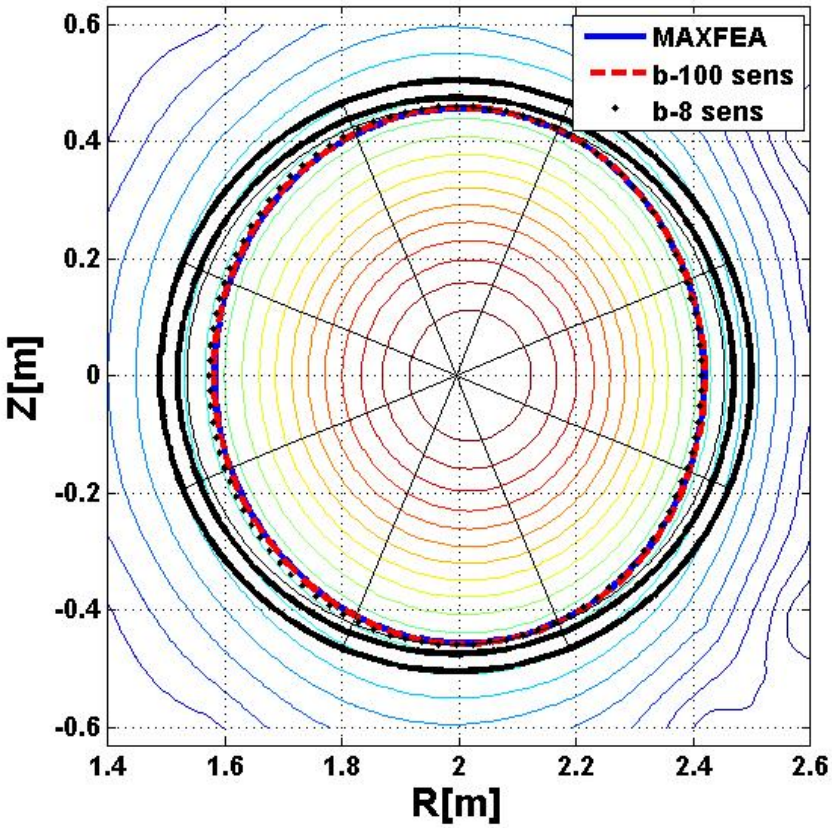

Figure 4.3: MAXFEA poloidal flux contour plot for the elongated limiter shot 38410 at t = 1.0 s. The solid blue line is the MAXFEA plasma boundary, the red line is the reconstructed boundary using the MAXFEA 100 virtual measurements of both ψ and B_θ, the black dotted line is the computation by the 8 experimental measurements of the same quantities. These 3 lines are nearly overlapping. The 8 black lines starting from the centre of the vessel represent the lines of sight along which the gaps are reconstructed in the real time version of the code. Figure taken from [52].

first sidebands are significant: in the particular RFX-mod case, the $m = 1$ "measured" harmonic has contributions from the $m = 7$ and the $m = 9$ "true" ones, the $m = 2$ is polluted by the $m = 6$ and $m = 10$ while the $m = 3$ include contributions by the $m = 5$ and $m = 11$. The effect of sidebands aliasing is illustrated in Fig. 4.2 where "true" harmonics taken from a MAXFEA equilibrium with 100 sensors (squares) are compared with the "measured" harmonics as estimated by taking the Discrete Fourier Transform of 8 measurements (crosses). While the measured first harmonic almost coincides with the true one, we find a difference of 16 % and 21 % for the 2^{nd} and the 3^{rd} harmonic, respectively.

The estimate of the true harmonics starting from the measured ones is based on the subtraction of the aliased sidebands from the measurement. This is possible because high order harmonics are mostly produced by external currents and the signal does not include a significant contribution of

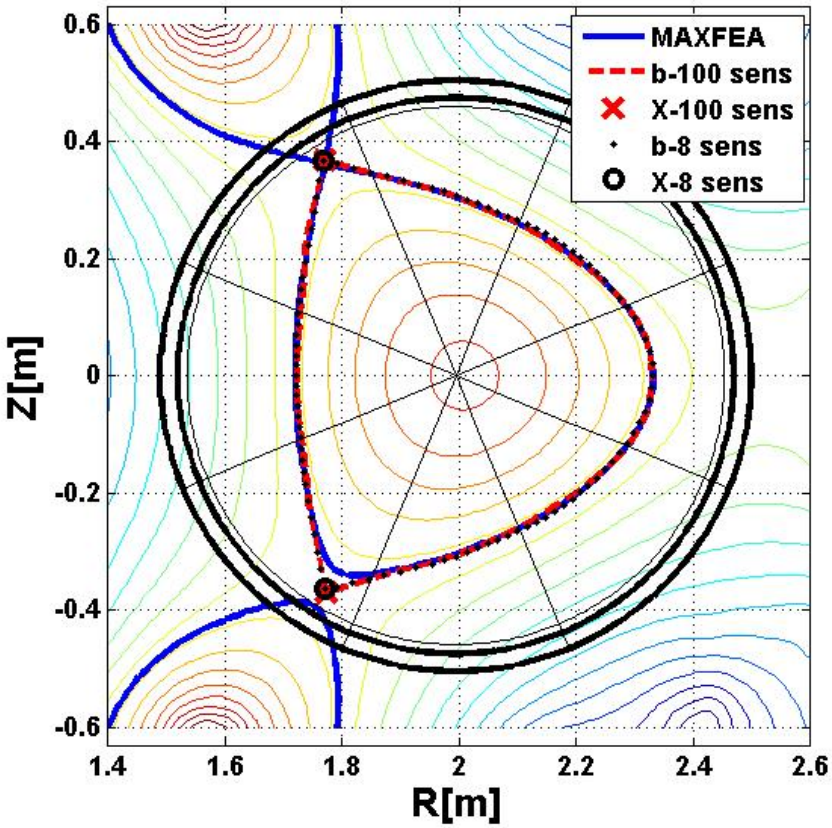

Figure 4.4: Same quantities as in Fig. 4.3 for the Double Null shot 36336 at t = 0.7 s. In addition, red X's are the X-points computed by the virtual sensors and black O's are the X-points determined by the experimental measurements. Figure taken from [52].

the plasma. In order to prove this, a vacuum MAXFEA run has been performed with the same PFS currents of the shot considered in Fig. 4.2 and its spectrum has been subtracted from the one with plasma: in this way we extract the plasma contribution shown with diamonds in the same figure. With the exception of the first two harmonics, the plasma contribution is always much lower than the total harmonic. This confirms that high order harmonics are safely estimated on the basis of the PFS currents only.

Therefore the required spectrum of 6 harmonics is estimated as follows: the m=1,2 and 3 harmonics are estimated by subtracting from the measured ones the corresponding aliased vacuum harmonics, while the m=4,5 and 6 are taken just as the vacuum harmonics. This is done for B_θ, $\hat{\psi}$ and $\tilde{\psi}$ signals.

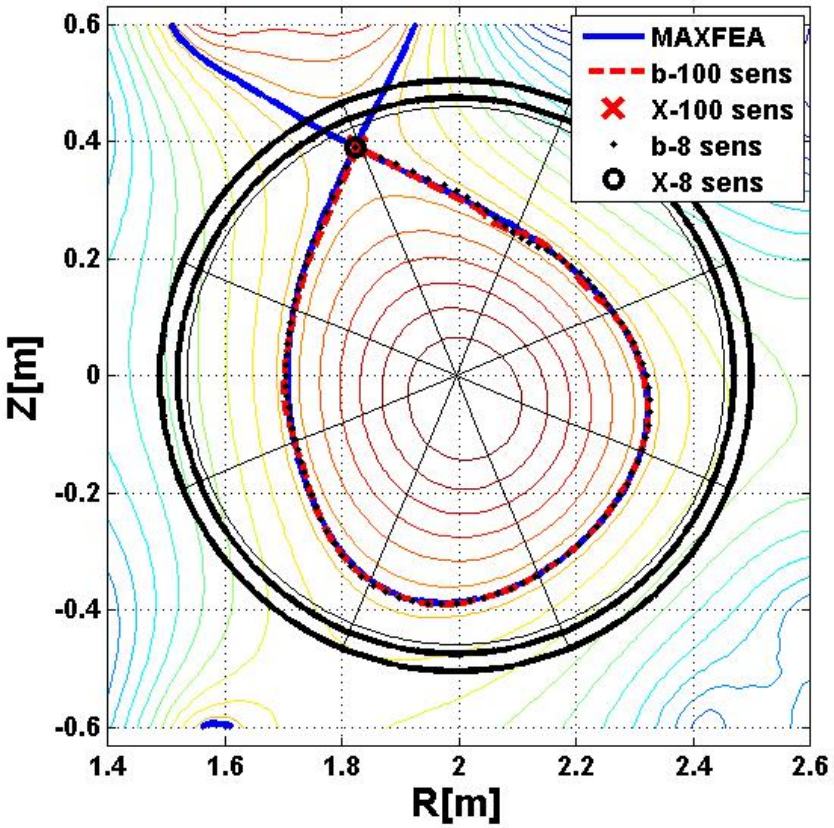

Figure 4.5: Same quantities as in Fig. 4.4 for the Single Null shot 37032 at t = 0.8 s. Figure taken from [52].

The signal S^j_{low} of sensor j (this stands for B_θ, $\hat{\psi}$ and $\tilde{\psi}$) corresponding only to the low harmonics is computed in the following way:

$$S^j_{low} = S^j - \sum_{i=1}^{N_{PFS}} H^j_i I_i, \tag{4.15}$$

where S^j is the measured signal, I_i is the $i-th$ current in the PFS, N_{PFS} is the number of PFS currents (12 in case of RFX-mod) and H^j_i is the higher harmonic contribution generated by the PFS $i-th$ unit current at the sensor j:

$$H^j_i = s^j_i - \sum_{m=0}^{3} hc^m_i cos(m\theta_j) - \sum_{m=0}^{3} hs^m_i sin(m\theta_j), \tag{4.16}$$

where s^j_i, hc^m_i, and hs^m_i are the total signal of sensor j and the cosine and sine harmonics generated by the PFS $i-th$ unit current, respectively.

When this method of harmonic computation with 8 sensors instead of 100 is used, the discrepancy with MAXFEA in the boundary reconstruction increases from 3 mm to 8 mm. This precision is considered sufficient for the feedback control of the RFX-mod tokamak discharges. However, to obtain accurate results in the non-stationary phases of the discharge, some modifications must be introduced into the algorithm to take into account the field penetration effect through the conductive structures.

4.4.1 Effects of Currents in Conductive Structures

The field generated by the PFS currents is screened by all the innermost passive structures. Therefore the $m > 3$ harmonics of this field, which are used both to remove the aliasing in the measurements and to provide the additional information for the boundary reconstruction are filtered by these structures. The corresponding time constants were determined using a vacuum MAXFEA evolutive simulation where a step-wise waveform of the PFS currents was applied. The results for the harmonics of interest are shown in Table 4.1. The harmonics $m > 6$ are characterized by a very low amplitude. They are used just in the de-aliasing procedure using the same filter as in the $m = 6$ case.

n	$\tau_{B_\theta} = \tau_{\hat{\psi}}[ms]$	$\tau_{\tilde{\psi}}[ms]$
4	16	28
5	13	16
6	10	13

Table 4.1: The time constants for penetration of B_θ, $\hat{\psi}$ and $\tilde{\psi}$ through the passive structures.

After including all the corrections mentioned in this section, the first 6 series of the harmonics are computed with the best possible accuracy. In the transient phases, the effect of the harmonics filtering on the plasma boundary can be up to 3 mm.

The toroidal current produced in the continuous vessel by the applied toroidal loop voltage also needs to be taken into account, since it determines a jump of B_θ. This can be estimated from the ϕ component of the Ampere's law $\nabla \times \mathbf{B} = \mu_0 \mathbf{j}$ by assuming the thin-shell approximation. The correction for the B_θ inside the vessel is the following extra term

$$B_\theta^v = \frac{\mu_0 V_t(\theta)\delta_v}{\rho \cdot 2\pi(R_0 + r_v cos(\theta))} \frac{r_v}{r}, \tag{4.17}$$

where V_t is the toroidal loop voltage and ρ, δ_v, and $r_v = 0.49$ m are respectively the vessel toroidal resistivity, thickness and average minor radius. The above correction is considered for $r < r_v$, and its impact on the plasma boundary reconstruction amounts to 5 mm.

4.5 Real time application

Besides the offline analysis, the method has been used for the real time control of the distance between the first wall and the plasma boundary. In order to limit the computational load just 8 gaps along the lines of sight connecting the flux loops and the centre of the vacuum vessel are considered, as shown in figures 4.3, 4.4 and 4.5. For this purpose, the present algorithm has been implemented in the MARTE framework [54] on a platform using two Intel Xeon Processor X5660 (12 M Cache, 2.8 GHz, 6 cores, 6.4 GT/s Intel QPI) with 12 GB RAM and a Scientific Linux distribution with real time patches from CERN as the operating system. The calculation has to be performed in less than 200 μs to provide the values of the plasma-wall distances for the controller. This requirement is fulfilled by a large margin, as the calculation takes approximately 100 μs. This algorithm has been used during the last year of RFX-mod operation without facing any problems.

4.5.1 Noise effect

It is also important to assess the robustness of the algorithm with respect to the noise that is present in all the magnetic measurements. Therefore a random noise with different amplitudes was added to the measurements. First of all, we considered the pick-up probes and the flux loops signals. The effect on the plasma boundary is shown in Fig. 4.6 for noise levels equal to 3 %, 6 % and 9 % of the signal. The maximum differences from the case with no noise are 1 cm and 2.5 cm for the 3 % and the 6 % noise levels, respectively. These errors are still acceptable for the real time control of the plasma boundary. The maximum difference increases to an exceedingly large value of 5 cm for the 9 % noise case. On the other hand, the real noise level in RFX-mod is below 1 % among both pick-up coils.

Moreover, the noise in the measurements of the PFS currents could also affect the robustness of the algorithm. The results are shown in Fig. 4.7 for noise level of 15 %, 30 % and 50 %. The maximum differences from the no-noise case amount to 0.5 cm and 1.5 cm for the 15 % and 30 % noise levels, respectively. These discrepancies are largely acceptable. The 4 cm difference obtained in the 50 % noise case approaches the maximum acceptable error. However, this is not an issue in RFX-mod, since the noise in the PFS current measurements is well below any of these levels. The errors in the PFS current measurements have a smaller influence than those on the flux and field measurements considered above because they are used just to estimate the high harmonics and to correct the aliasing.

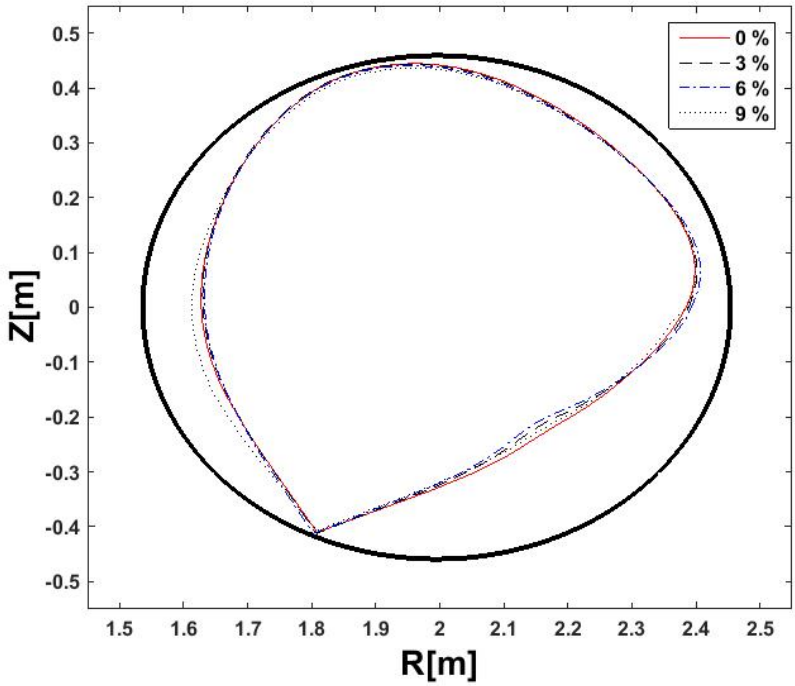

Figure 4.6: Effect of different noise levels in pick-up probe and flux loop measurements on the plasma boundary reconstruction. Single-null shot 38306 is considered. Figure taken from [52].

From this analysis we can conclude the RFX-mod measurement noise is not a problem for the boundary reconstruction.

4.5.2 Experimental results

The RFX-mod shape controller was designed following a model-based approach as described in [51]. Its input signals are the 8 differences between the gap references and those reconstructed by the algorithm. Its outputs are the 8 voltage references for the 8 field shaping coil power supplies. An example of the controller action in response to a reference change of the four upper gaps in a lower Single Null discharge is presented in Fig. 4.8. One can appreciate the good tracking accuracy provided by the control system. The resulting difference of a few millimeters is negligible for the experiment.

4.6 Conclusion and Future Work

This chapter introduced a novel method of plasma boundary reconstruction developed for RFX-mod. The main advantage of this algorithm for boundary computation is that it provides reliable results even in case that a limited set of magnetic sensors is installed. This method was used for

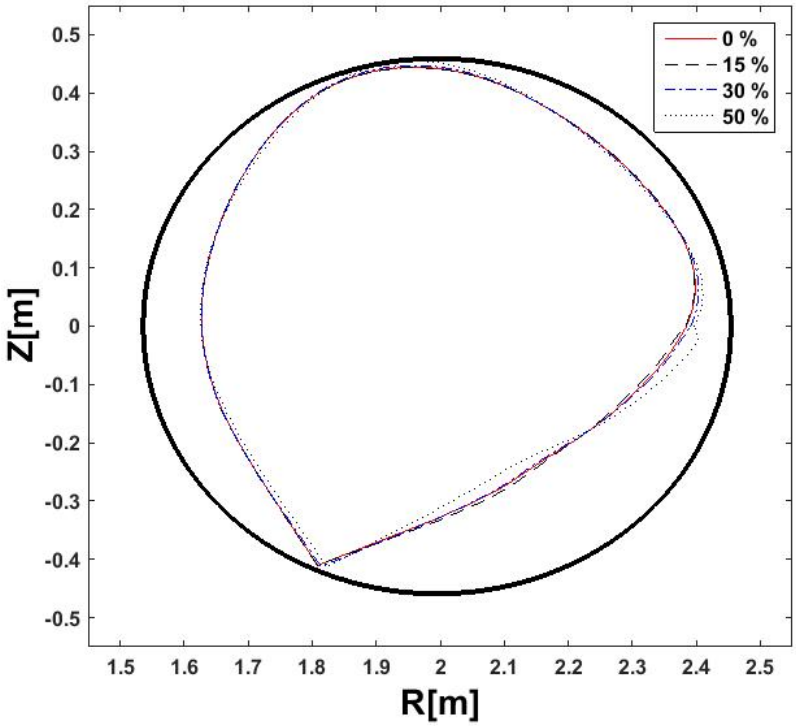

Figure 4.7: Effect of different noise levels in PFS current measurements on the plasma boundary reconstruction. Single-null shot 38306 is considered. Figure taken from [52].

extended physical analysis of RFX-mod discharges described in chapter VI and for the feedback control of the plasma shape described in chapter V.

In future, it is expected to be used as a benchmark for a full equilibrium reconstruction code LIUQE that is being implemented on RFX-mod. LIUQE contains much more information about the geometry of conductive structures on RFX, the comparison might be used to find possible imprecision in the method during the transition phases due to simplified model of the conductive structures we used.

Last, not least, the method could be possibly extended to D-shape devices.

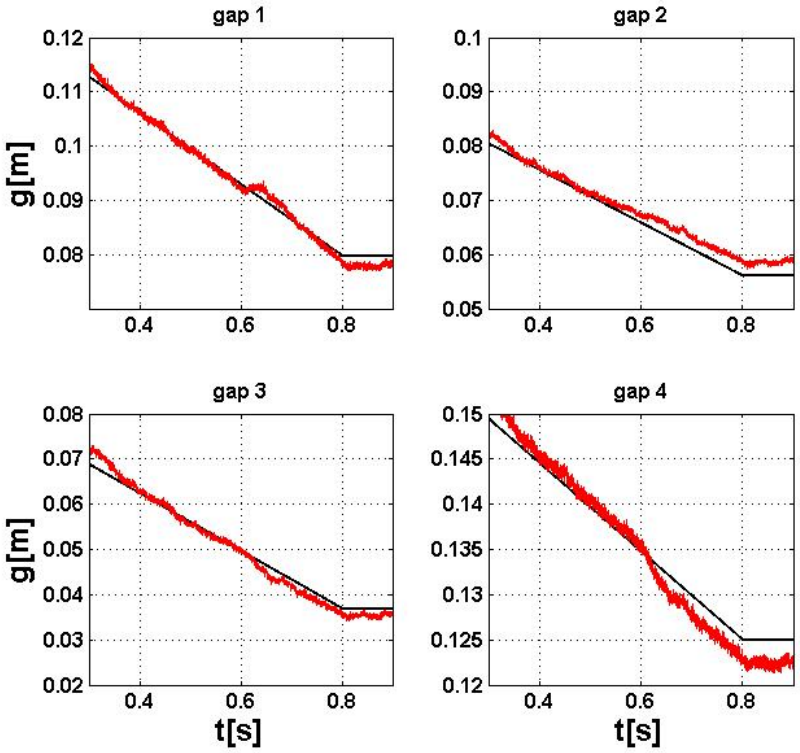

Figure 4.8: The time evolution of the 4 upper gaps between the plasma and the first wall for the single null shot 38163. The references and the real values are represented by the black and the red lines, respectively. In addition to the reference variation, the gas puffing was modified at $t = 0.6$ s. The numbering of the gaps goes from the low field side towards the high field side. Figure taken from [52].

CHAPTER V

Plasma Position and Shape Control in RFX-mod Tokamak Regime

This chapter will deal with plasma vertical position and shape control issues that appeared with shaped experiments. The control system design is fully model based, therefore it is possible to deal in advance with some problematic issues such as the presence of the conductive structures that slow down the changes of the plasma properties (like growth of unstable modes) and the field penetration from field sources located outside the shell. Other critical issues that must be considered are the coupling, both magnetic and resistive, between the poloidal field coils and the voltage limits of the power supplies. As for the controller, a linear quadratic regulator and a Kalman state estimator were designed. This chapter gives a brief overwiev of this activity. It is based on [61], which provides further details.

5.1 Design of the Plasma Shape Control System

5.1.1 Linearized Plasma Response Model

For the controller design, first of all a linearized plasma response model had to be derived and validated. The model was derived using code CREATE-L [62]. This code was extensively applied and validated on TCV [63] and JET [64]. The JET eXtreme Shape Controller (XSC) [65] is also based on this linearized model.

The model of the RFX-mod plant consists of 193 states: 8 currents of the poloidal field shaping coils, 4 of the magnetizing coils, 2 currents corresponding to the 2 virtual circuits obtained by the anti-series connection of the saddle coils belonging to the up-down and outer-inner arrays, respectively, 60 currents in the vacuum vessel, 59 in copper shell and 59 in the support structure. The last state variable is the plasma current. The current of the outer-inner array of the saddle coils

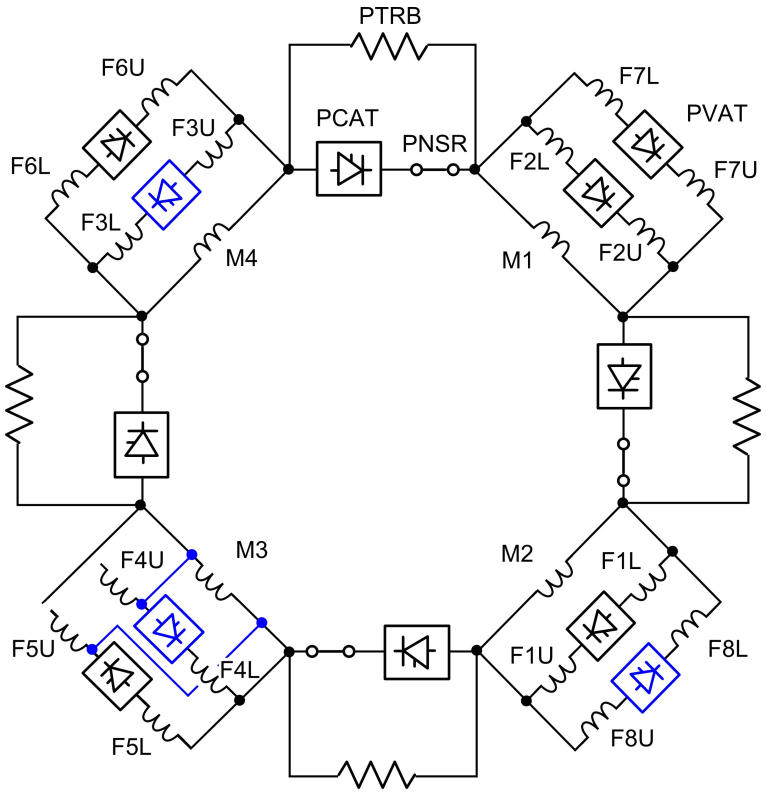

Figure 5.1: The electrical network of RFX-mod poloidal field coils. the modifications in single null configuration are depicted by blue color. Image taken from [61].

generate the radial field component needed to control the vertical instability. In fact, the model shows presence of a vertical unstable mode with a growth rate about 10 s^{-1}. A proper reconnection matrix was included to take into account the topology of the poloidal field electric system made up by four sectors where elements of the magnetizing coils and couples of field shaping coils are directly connected. The connection is shown in Fig. 5.1.

The linearized model on RFX-mod was validated against evolutive finite element MAXFEA code (see part 4.1 for more information). Poloidal flux, poloidal field and gap evolutions are shown in Fig. 5.2, Fig. 5.3 and Fig. 5.4, respectively, in the case of ramp variations of some poloidal field coils currents. The sensor position angle written in the figures is considered from the midplane in counter-clockwise direction. The linear approximation holds for small variations. The deviation can become critical if the unstable modes are free to evolve.

5.1.2 Vertical Position Stabilization

Before designing shape controller, it is necessary to remove the vertically unstable mode. In general, the vertical position control must be performed on a much shorter time scale than the shape control (see for example [34], [35]). In RFX-mod, the growth rate of the vertical instability

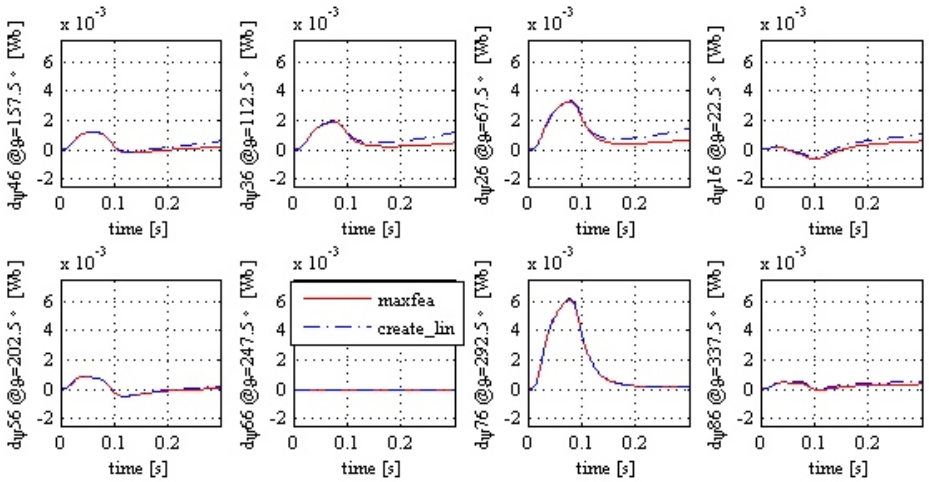

Figure 5.2: Time evolution of the poloidal magnetic flux in the presence of current variation in poloidal field coils estimated by MAXFEA and the linearized model used for shape controller design. The reference flux level is at flux loop number 6. Image taken from [61].

is not a major issue due to the presence of the conductive copper shell and the fact that RFX-mod plasmas are just weakly elongated.

For vertical stabilization, one needs to generate a radial magnetic field that produces a force counteracting the plasma motion. This field is provided by the currents flowing in the inner and outer array of the saddle coils. An additional advantage of the saddle coil system is their short time response enabling a safer operation.

The plasma vertical shift was chosen as the feedback variable. Proportional gain is sufficient to stabilize the plasma along the vertical direction [61]. The response time of the model is about 15 ms, much less than the characteristic time of the instability.

5.1.3 Model Order Reduction and LQG controller

To implement the controller in real time, it is convenient to reduce the model order as much as possible. Since the order of modern controllers is approximately the same as the order of the plant model, a solution is to apply model order reduction methods either on the plant model or the controller. There are 188 states in the basic version of the model (the upper-lower saddle coils are not used and the current evolution in the 4 magnetizing coils can be derived from Kirchhoff's circuit law for the poloidal field coils electrical network) that is not manageable in terms of computational speed of the controller. On the other hand, a compromise must be found between precision improved with increasing number of states. In this case the plant model order was reduced using Hanckel Singular Value Decomposition on the vertically stabilized plant response model. Acceptable

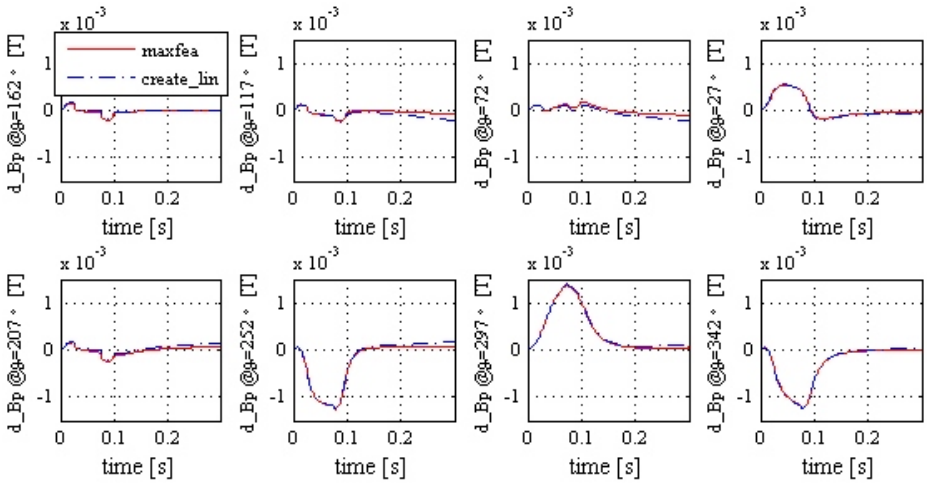

Figure 5.3: Time evolution of the poloidal magnetic field in the presence of a disturbance estimated by MAXFEA and the linearized model used for shape controller design. Image taken from [61].

agreement between the full and reduced model with satisfactory execution time was obtained for 38 states. These states do not have any particular physical meaning.

The reduced order model was used to design the Linear Quadratic Gaussian (LQG) controller consisting of a Kalman state estimator and a LQ optimal gain matrix calculated by minimizing a quadratic cost function. A steady state Kalman filter (details about Kalman filters are given in Appendix C) was designed. The output quantities covariance matrix needed for Kalman filter computation was derived from relevant quantities measurement: gaps, plasma position and current, poloidal field coils currents [61]. The covariance matrix relative to the states was tuned during the first experiments to improve the disturbance rejection in experimental conditions on RFX-mod.

Another important feature of the controller is the capability to track variations in the reference value. For that, a reference input array was included. The output signal reference transformed into a set of state references (remember that we use different states in the model) using matrix $\mathbf{N_x}$ and into a set of feedforward inputs using matrix $\mathbf{N_u}$. The details about the matrix computation can be found in [61]. Integral part had to be added to the controller to provide sufficient steady state accuracy. The control scheme is shown in Fig. 5.5. To choose the integral gain, the state was extended by the 8 real time gap measurement (see chapter IV for details).

5.2 Experimental Results of the Shape Control

The designed control system has operated on RFX-mod for more than one year. It must be capable to deal with many situations: current control in the shaping coils during transition from

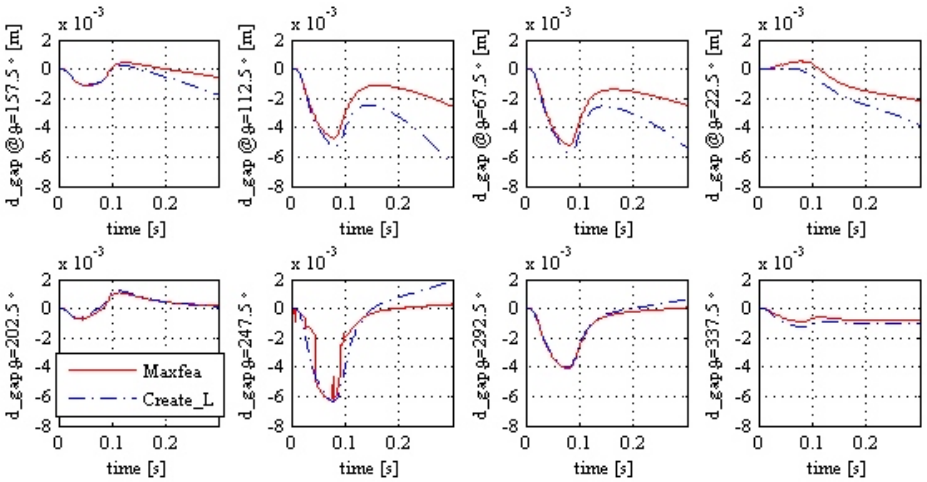

Figure 5.4: Time evolution of the gaps between separatrix and the first wall in the presence of a disturbance estimated by MAXFEA and the linearized model used for shape controller design. Image taken from [61].

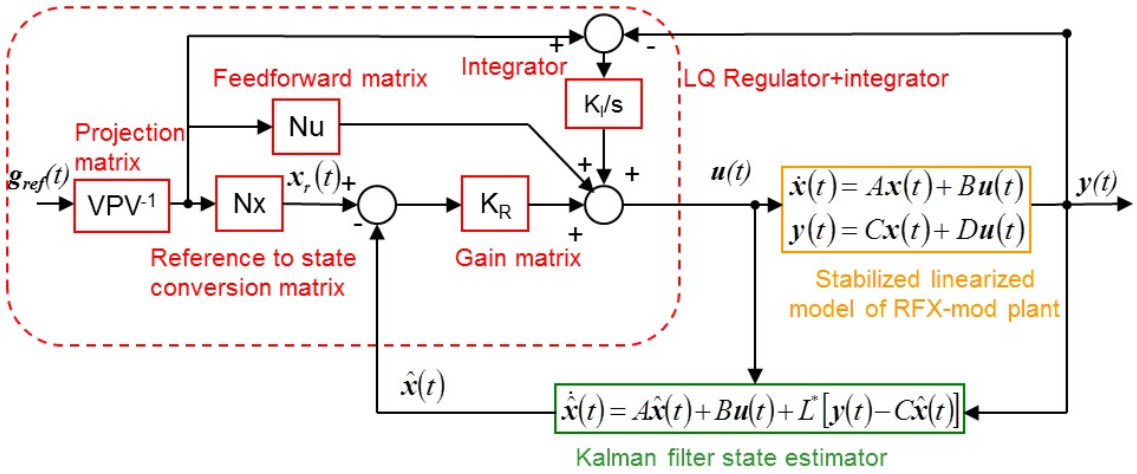

Figure 5.5: The scheme of the shape controller implemented on RFX-mod. Image taken from [61].

limited to diverted regime, perturbations of plasma shape or reference changes in the flat top phase (for example due to gas puff). This section provides a brief overview of the experimental results.

In Fig. 5.6, one can see the plasma shape at the beginning of the discharge and the shape after transition to diverted regime. After the controller being inserted at the end of the transition, the shape control system must be capable to maintain the gaps close to the reference values. Only limited oscillations which die out within 100 ms are observed.

The control system can also operate in tracking mode. An example of a good reference tracking is shown in Fig. 4.8. Such a good agreement has been routinely obtained for single null, double null, and limited discharges.

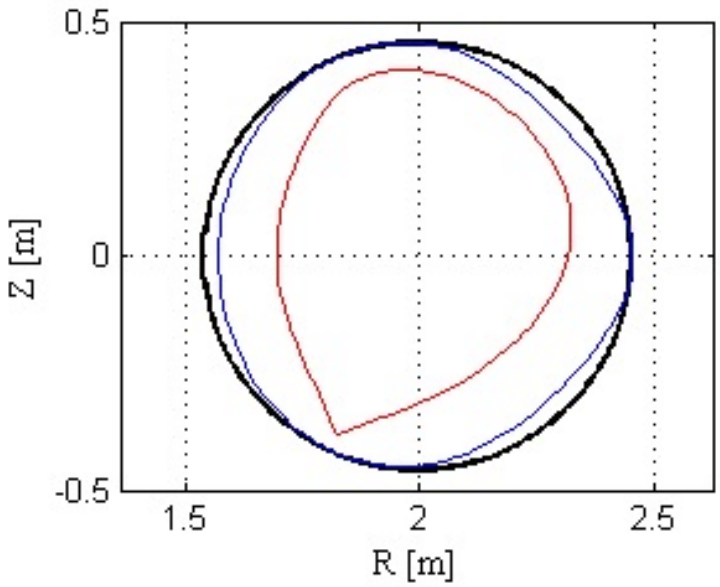

Figure 5.6: The plasma shape at the beginning of the discharge (blue) and after transition to diverted regime (red) in shot 37829. Image taken from [61].

Last important property of the system is the behavior in presence of disturbance. We have tested the evolution of the gaps after a gas puff, that perturbs both β_p and l_i, therefore the equilibrium related quantity $\beta_p + l_i/2$ is perturbed as well. As we will show in chapter VI, $\beta_p + l_i/2$ can be computed using the boundary reconstruction method. The perturbation of this quantity by a gas puff is shown in Fig. 5.7 for three discharges: 37834, 37835, and 37837. In 37835, the shape control was switched off, in the other two discharges the controller was active with different parameters. The modification of the $\beta_p + l_i/2$ modifies the gaps as well. The time evolutions of the Euclidean norms of the array calculated as the difference between each measured gap and reference gap for the three discharges are shown in Fig. 5.8. A large error is temporarily present after the gas puff, but the consequent steady state error is reduced by 19 % for 37834 and by 30 % for 37837 after slight modification of the control parameters. This indicates that the performance of the controller can be improved by parameter tuning.

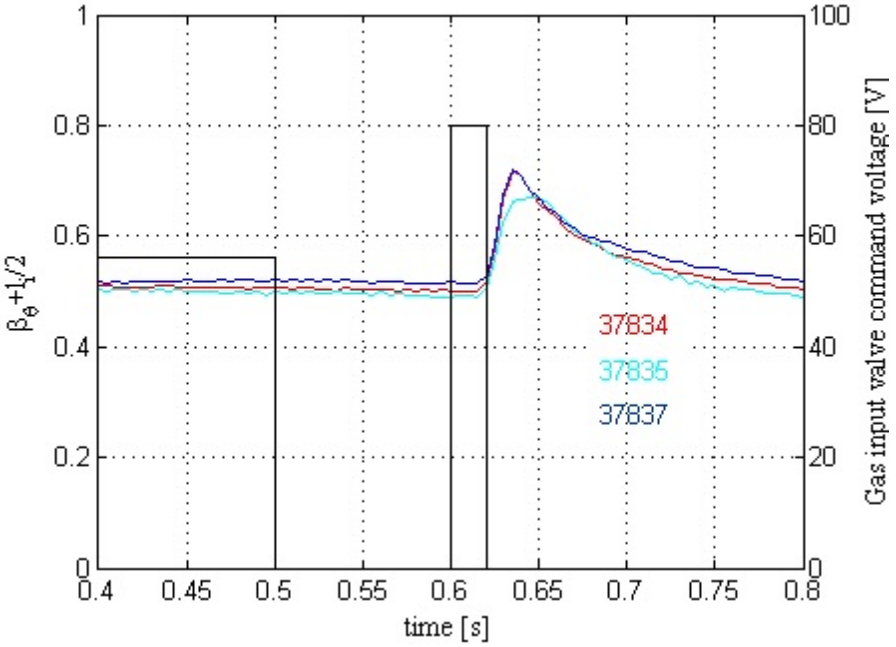

Figure 5.7: Time evolution of $\beta_p + l_i/2$ and gas valve voltage for discharges 37834, 37835, 37837. In all three discharges, the valve is open at t = 0.6 s for 2 ms to perturb the $\beta_p + l_i/2$ that affects the plasma equilibrium. Image taken from [61].

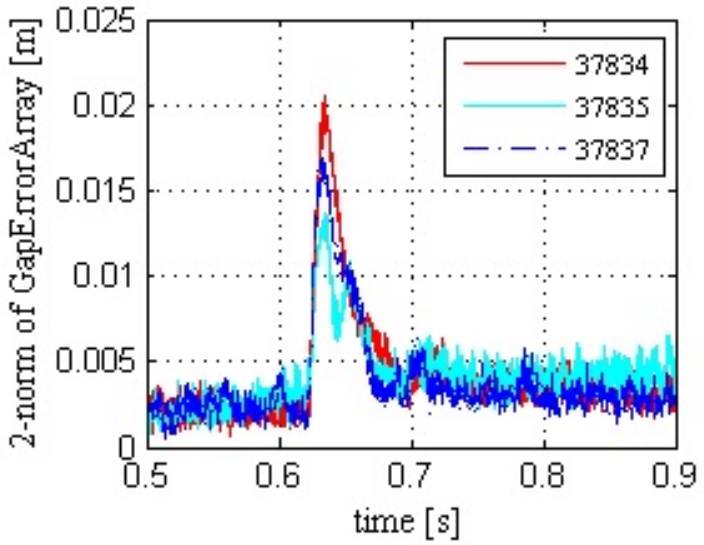

Figure 5.8: Time evolution on the Euclidean norm of array calculated as differences between actual and reference gap value for discharge 37834, 37835, 37837. Image taken from [61].

CHAPTER VI

Computation of Plasma Macroscopic Parameters in RFX-mod Tokamak Regime

In chapter IV, a method for precise and reliable plasma boundary computation was proposed. In this chapter, we will use the knowledge of the plasma boundary alongside with the diamagnetic measurement to recover some plasma macroscopic parameters such as β_p, internal inductance l_i, edge safety factor q_{95}, and an important quantity for the LH transition, the power through separatrix carried by charged particles.

First of all, let us describe the computation of the edge safety factor q_{95}.

6.1 Determination of the edge safety factor

Since tokamak discharges at very low edge safety factor are routinely executed in RFX-mod [24], [26], it is important to have a good estimate of this quantity both in limiter and X-point discharges. Here, a method to evaluate the standard edge safety factor q_{95} is presented. Define the following normalized flux-surface coordinate

$$x = 100\frac{\psi_0 - \psi_x}{\psi_0 - \psi_b}, \tag{6.1}$$

where ψ_b is the boundary poloidal flux and ψ_0 is the poloidal flux at the magnetic axis. Let us recover the safety factor using (2.9).

To calculate q_{95}, ψ_{95} and ψ_0 are needed. The difference between the poloidal flux at the magnetic axis and at the plasma boundary is given by [60]

$$\psi_0 - \psi_b = \frac{l_i \mu_0 R_0 I_p}{2} \cong \frac{B_{t0} k a^2}{2 q_0} \cdot C I_p. \tag{6.2}$$

Here B_{t0} is the toroidal magnetic field in the vessel centre, inferred from the measurement of the currents in the toroidal field coils, I_p is the plasma current, k is the elongation, C is a constant, determined using MAXFEA, a is the plasma minor radius and q_0 is the on-axis safety factor. The last quantity is assumed equal to 1, since sawteeth activity is usually observed. Since the measurement of l_i is not reliable enough in all RFX-mod discharges, we adopted the final approximation in formula (6.2) which exploits the Solovev solution of the Grad-Shafranov equation [60], [59] with an additional explicit dependence on the plasma current.

Using (6.1) and (6.2), ψ_{95} can be expressed in terms of the boundary flux and other global plasma parameters:

$$\psi(95) = \psi_b + 0.05 \cdot \frac{B_{t0} k a^2}{2} \cdot C I_p. \tag{6.3}$$

Knowing this value, the geometric coordinates of the ψ_{95} flux surface are estimated in exactly the same way as the plasma boundary. Despite that the reconstruction method described in chapter IV is valid just in vacuum, in this case it is also applied in the edge region of the plasma due to the low current density assumed there. The difference between the estimated ψ_{95} flux surface and MAXFEA is below 1.5 cm for all the studied cases. To perform the derivative in (2.9) a narrow region between the flux surfaces corresponding to $\psi_{95} + \epsilon$ and $\psi_{95} - \epsilon$ is considered. Accordingly, $d\psi = 2\epsilon$. To estimate $d\Phi$ we proceed as follows. The width of the annular region between the two flux surfaces is computed by

$$w(\xi) = \frac{2\epsilon}{2\pi R(\xi)\sqrt{B_\theta^2(\xi) + B_r^2(\xi))}}, \tag{6.4}$$

where ξ is a coordinate along the curve which identifies the ψ_{95} flux surface in a poloidal plane. The toroidal flux through this region is given by

$$d\Phi = \int B_t(\xi) \cdot w(\xi) d\xi, \tag{6.5}$$

where B_t is the toroidal magnetic field whose radial dependence is approximated by the vacuum expression.

$$B_t(R) = \frac{B_{t0} R_0}{R}. \tag{6.6}$$

Finally, q_{95} is computed from the estimated $d\psi$ and $d\Phi$ according to equation (2.9). As far as the approximation used in (6.2) is concerned, we notice that it is not significant. In fact, even a 20 % error in $\psi_0 - \psi_b$ causes a difference lower than 2 % in the q_{95} computation.

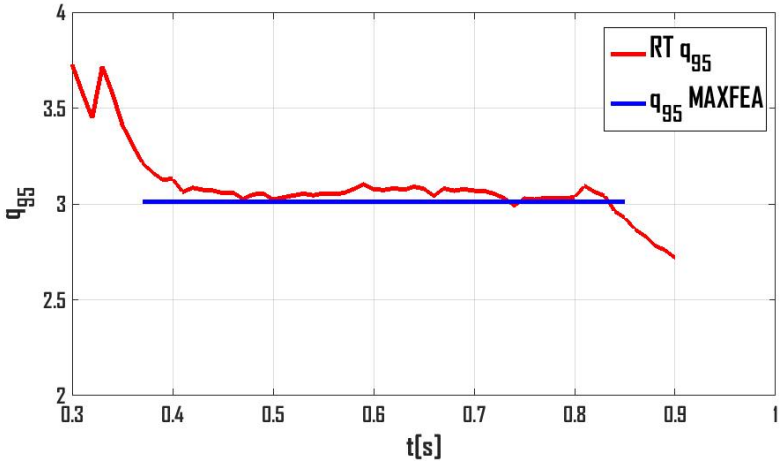

Figure 6.1: Comparison of q_{95} estimated by the present algorithm (red) and by MAXFEA (blue) for discharge 36380.

The time evolution of the estimated q_{95} is shown in Fig. 6.1 alongside with the MAXFEA output. The comparison can be made only in the flattop phase, when the final configuration is reached. The agreement is satisfactory, despite the perturbation due to the gas puff applied between 0.63 and 0.71 s in this shot (the same as considered later in Fig. 6.2). In general, the discrepancy is found below 4 % for a wide range of plasma parameters.

6.2 Evaluation of $\beta_p + l_i/2$

The reconstruction of the plasma boundary can be used to determine quantities, such as β_p and the internal inductance l_i, which involve surface integrals, in both limiter and diverted configurations. Only the combination $\beta_p + l_i/2$ can be generally derived from the magnetic measurements used for the plasma boundary reconstruction. In fact, they affect the equilibrium value of the plasma major radius in the same way. The separation can be performed either using diamagnetic loop to measure the value of β_p (see section 6.3) or by an approach similar to the one used in this section for elongated plasmas (see section 6.4) To recover $\beta_p + l_i/2$, we adopted the following equation, valid for general plasma shape [58]:

$$\frac{s_1}{2} + s_2 = \beta_p + \frac{l_i}{2}. \tag{6.7}$$

It is based on the calculation of the following two integrals along the plasma boundary:

$$s_1 = \frac{\pi}{V < B_p^2 >} \int R(s) B_p(s)^2 \mathbf{n}(s) \cdot \mathbf{p}(s) ds, \tag{6.8}$$

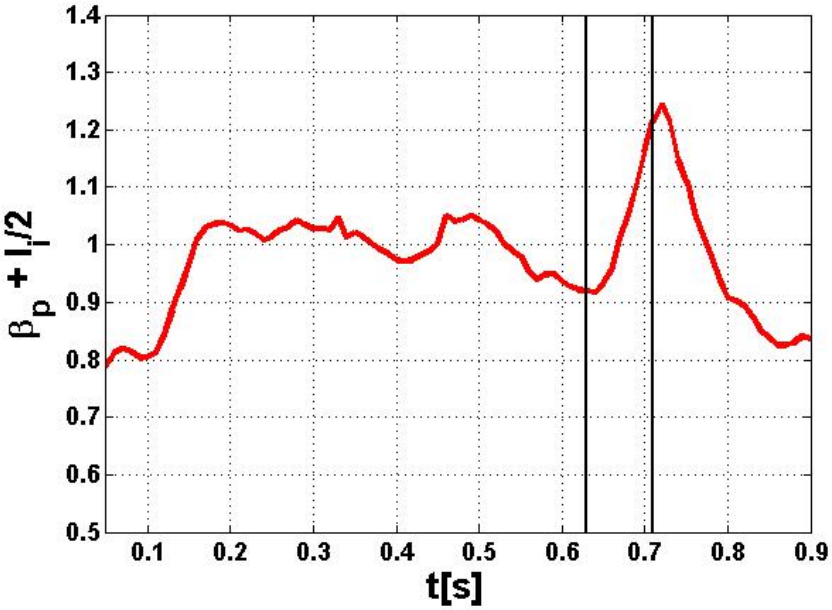

Figure 6.2: Time evolution of $\beta_p + l_i/2$ for the discharge 36380. The gas valve was open in the time interval between the two black vertical lines.

$$s_2 = \frac{\pi R_{ax}}{V < B_p^2 >} \int R(s) B_p(s)^2 \mathbf{n}(s) \cdot \mathbf{e_R} ds, \tag{6.9}$$

where V is the plasma volume, B_p is the poloidal magnetic field on the plasma boundary and $<>$ denotes its mean value along the plasma boundary, R_{ax} is the radial coordinate of the magnetic axis, R is the radial coordinate of the plasma boundary, $\mathbf{n}$ is the normal vector to the plasma boundary, $\mathbf{p}$ is the vector connecting magnetic axis and the plasma boundary, $\mathbf{e_R}$ is the unit vector in radial direction and ds refers to the integration along the plasma boundary. To evaluate this integral we exploit the estimate of the plasma boundary and the poloidal magnetic field on it provided by the present reconstruction algorithm. The position of the magnetic axis is approximated by the plasma boundary geometric centre.

This computation was first compared with a set of MAXFEA simulations, performed with a wide range of β_p and l_i values. The differences are lower than 1 % for standard RFX-mod discharges ($\beta_p + l_i/2$ between 0.8 and 1) and increase up to 4 % for the extreme cases considered (values of $\beta_p + l_i/2$ between 0.5 and 1.3).

The method was also tested experimentally. In the shot shown in Fig. 6.2 a gas puff was applied between $t = 0.63$ s and $t = 0.71$ s. The computed quantity $\beta_p + l_i/2$ started to increase 2 ms after the opening of the gas valve and started dropping 2 ms after its closure. This is exactly the behaviour expected from a plasma density increase.

6.3 Measurement of β_p by Diamagnetic Loop

The diamagnetic loop consists of a wire wrapped around the vacuum vessel in poloidal direction. It measures the total toroidal magnetic flux Φ through the surface enclosed by the wire. Φ is governed by toroidal magnetic field generated by external coils. However, there are also two small contributions from the plasma: one arises from the plasma current, the other one from the chaotic Larmor motion of the charged particles.

The effect of the plasma current enhances the externally applied toroidal magnetic field, i.e. the plasma acts as paramagnetic material. The paramagnetic flux equals to [66]

$$\Phi_{par} = \frac{\mu_0^2 I_p^2}{8\pi B_{t0}} = \frac{\pi(r_m < B_\theta(r = r_m) >)^2}{2B_{t0}}, \tag{6.10}$$

where B_{t0} is the toroidal magnetic field on the axis and $B_\theta(r = r_m)$ is the mean poloidal magnetic field at the diamagnetic loop radius $r_m = 0.5085m$.

The effect of the Larmor motion is opposite as it tends to reduce the size of the toroidal magnetic field, i.e. it acts as a diamagnetic material. The diamagnetic flux is equal to [66]

$$\Phi_{dia} = \beta_p \Phi_{par}. \tag{6.11}$$

In reality, we can measure just the difference between these two fluxes defined as

$$\delta\Phi = \Phi - \Phi_{vac}, \tag{6.12}$$

where Φ is the total toroidal magnetic flux measured by the diamagnetic loop and Φ_{vac} is the vacuum toroidal flux that is computed from the current in the toroidal field coils. The knowledge of these two quantities is used to derive $\delta\Phi$. Another expression for $\delta\Phi$ reads as

$$\delta\Phi = \Phi_{dia} - \Phi_{par} = \Phi_{par}(\beta_p - 1). \tag{6.13}$$

and is used for recovery of β_p by diamagnetic loop using formula

$$\beta_p = 1 + \frac{2B_{t0}}{\pi a_p^2 B_a^2}\delta\Phi, \tag{6.14}$$

where a_p is the mean plasma radius and B_a is the mean field on the last closed flux surface. For shaped plasma, the equation (6.14) is modified as follows:

$$\beta_p = s_1 + \frac{2B_{t0}}{\pi a_p^2 B_a^2}\delta\Phi. \tag{6.15}$$

Practical implementation of this method is complicated in some cases since the effect of the toroidal field is 3-4 orders of magnitude higher than the paramegnetism/diamagnetism of the plasma. In most tokamaks, this property of the measurement is dealt by advanced electronic systems such as diamagnetic loop with compensating coil [66] and advanced mathematical models to get rid of all parasitic effects as shown for example in [67].

In RFX-mod, there are 10 diamagnetic loops located at different toroidal sections, none of them connected with the advanced electronic systems mentioned above. The quantity $\delta\Phi$ is recovered from the average magnetic flux measured by the 10 diamagnetic loops. First of all, the vacuum magnetic flux needs to be estimated:

$$\Phi_{vac} = k \cdot I_{TF}, \tag{6.16}$$

where I_{TF} is the current feeding the toroidal field coils and k is the constant estimated in the initial part of the discharge when the toroidal magnetic field is already in the flat-top, but the plasma current is not induced yet. Due to severe requirement in the precision of k, it is necessary to make a new estimate at the beginning of each discharge as k is slightly different: even a small difference in this estimate can cause severe error on β_p measurement. The time evolution of β_p is shown in Fig. 6.4.

Using this procedure, we obtain reasonable estimates of β_p most discharges. The problem sometimes appears in very low current shaped discharges. Therefore an alternative method elaborated in the following section was implemented as well.

6.4 Separation of β_p and l_i for Elongated Plasmas

In this section, the method of β_p and l_i separation in RFX-mod shaped discharges by surface integrals computation will be presented. As mentioned in previous section, the β_p evaluation by diamagnetic loop is not reliable for RFX-mod low current shaped discharges due to the hardware limitations. Therefore a method of β_p and l_i separation presented in [68] was implemented and used. This method is based, similarly as the method described in section 6.2, on computation of integrals

along the plasma boundary. Let us introduce a new integral,

$$s_3 = \frac{2\pi R_0}{V < B_p^2 >} \int z(s) B_p(s)^2 \mathbf{n}(s) \cdot \mathbf{e_z}(s) ds, \tag{6.17}$$

where $z(s)$ is the vertical position and e_z is the unit vector in vertical direction. The l_i is expressed as

$$l_i = \frac{1}{\alpha - 1}\Big(s_1 + s_2(1 - \frac{R_t}{R_0}) - s_3\Big), \tag{6.18}$$

where R_t is the plasma centroid position and

$$\alpha = \frac{2\kappa^2}{1 + \kappa^2}, \tag{6.19}$$

where κ is the plasma elongation. Knowing l_i, the computation of β_p from (6.7) is straightforward.

The main drawback of this approximation is that the estimates of l_i are not generally valid. The comparision of computation error of l_i and $\beta_p + l_i/2$ using the integrals along separatrix as a function of elongation is shown in Fig. 6.3. One can see that the computation of $\beta_p + l_i/2$ is valid for any type of plasma, but the computation of l_i does not hold for discharges with very low elongation.

Last, let us compare the results of the two above mentioned methods of β_p computation. Discharge number 39143 was chosen for demonstration, as both methods are expected to provide reliable results: it is a shaped discharge and the time of toroidal field flat-top is long enough to provide reliable estimate of k. We can see good agreement between these two methods everytime but a short time instance when the elongation is low, so the l_i computation in (6.18) is not valid.

6.5 Energy Confinement Time

The knowledge of the plasma boundary and β_p can be also used to recover an important parameter describing the quality of the plasma confinement, energy confinement time τ_E. It is defined as

$$\tau_E = \frac{W_p}{P_{in}} = \frac{\beta_p V < B_a^2 >}{2\mu_0 V_t I_p}, \tag{6.20}$$

where W_p is the kinetic energy content of the plasma and P_{in} is the energy input to the plasma. As RFX-mod does not have any additional heating sources,

$$P_{in} = I_p V_t. \tag{6.21}$$

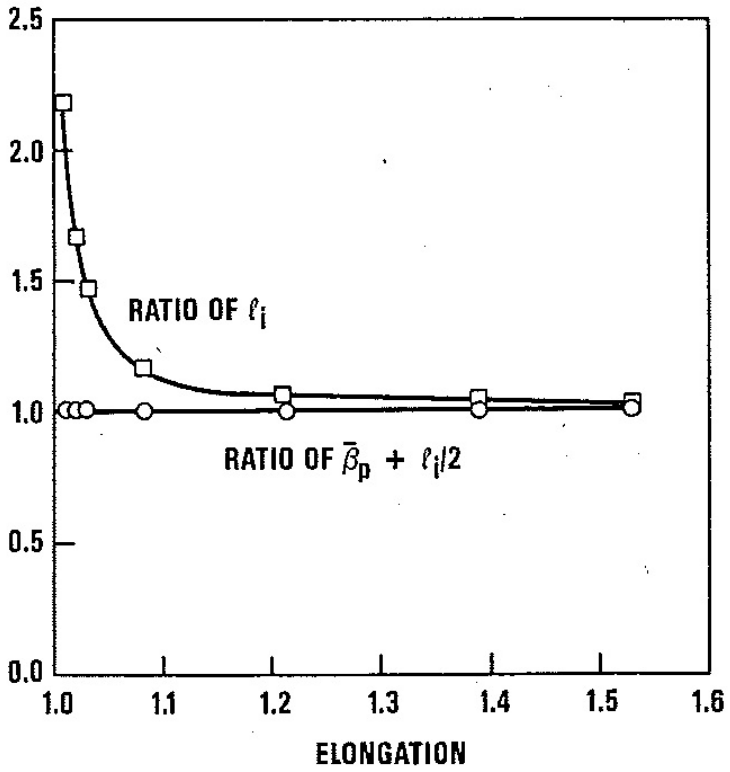

Figure 6.3: Ratios of l_i and $\beta_p + l_i/2$ computed by surface integrals to their exact values for different plasma elongations. Figure taken from [68].

6.6 Computation of Power Through Separatrix Carried by Charged Particles

One of the necessary conditions for the LH transition to be met is that the power through separatrix carried by charged particles P_{sep} has to be above a critical value. As RFX-mod aims at reaching H-mode, a part of this work was dedicated to the estimate of this quantity.

To compute the P_{sep}, we start from the power balance equation [69]:

$$V_t I_p = P_{sep} + I_p\Big(L\frac{dI_p}{dt} + I_p\frac{dL}{dt}\Big) + \frac{dW}{dt} + P_{rad} \tag{6.22}$$

where L is the plasma inductance, W is the plasma kinetic energy and P_{rad} is the power radiated by the plasma. All the quantities besides P_{sep} in (6.22) can be either measured (this is the case of V_t, I_p and P_{rad}), or computed by the combination of the boundary reconstruction method mentioned in section IV and the β_p and l_i computation described in the previous section. This is the case of L and W. The plasma inductance is given by the sum of internal inductance l_i determined in previous section and external inductance that can be computed by elliptic integrals using the knowledge of

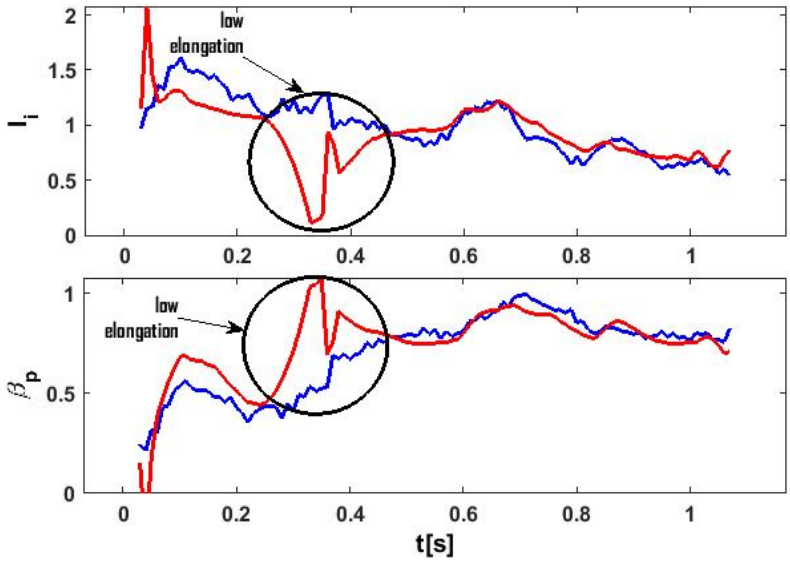

Figure 6.4: The time evolution of β_p and l_i measured by diamagnetic loop (blue) and computed by integral methods (red) for shot 39143.

plasma boundary coordinates. The plasma kinetic energy W can be computed using the value of β_p: the ratio of the plasma kinetic pressure and the poloidal magnetic field pressure on the plasma boundary. As β_p is known and magnetic field at the plasma edge can be provided by the boundary reconstruction code, the computation of W is straightforward. The importance of this calculation will be shown in the following chapter VII where the experiments aiming at L-H transition will be described.

CHAPTER VII

First LH Transition Experiments in RFX-mod Tokamak Regime

7.1 Motivation for LH Transition Experiments on RFX-mod

One of the targets of the diverted experiments on RFX-mod is achievement of reproducible H-mode condition. Besides the obvious motivation of having a confinement as good as possible, there are several other specific aspects.

First of all, the RFX-mod is equipped by the largest set of saddle coils of all existing devices. If ELMy H-mode were achieved, the RFX-mod saddle coils set could be used for ELM mitigation by resonant magnetic perturbation. Possibly, experiments to identify the optimal number and position of the saddle coils for the mitigation could be performed.

Secondly, the configuration of RFX-mod is rather different from other devices routinely reaching H-mode: the toroidal magnetic field is weaker, therefore the density limit is lower, the plasma shape and aspect ration are also not typical. This feature could be useful for tuning of the scaling laws determining which conditions must be fulfilled to reach H-mode.

7.2 Conditions to Reach H-mode

The boundary between the L-mode and H-mode configuration is approximately defined by a set of several plasma parameters. Let us describe these parameters and discuss the location of the RFX-mod discharges in this parameter space.

The first condition is related to the power through separatrix carried by charged particles partially described in 6.6. If this quantity is high enough, the LH transition may appear (depending on density

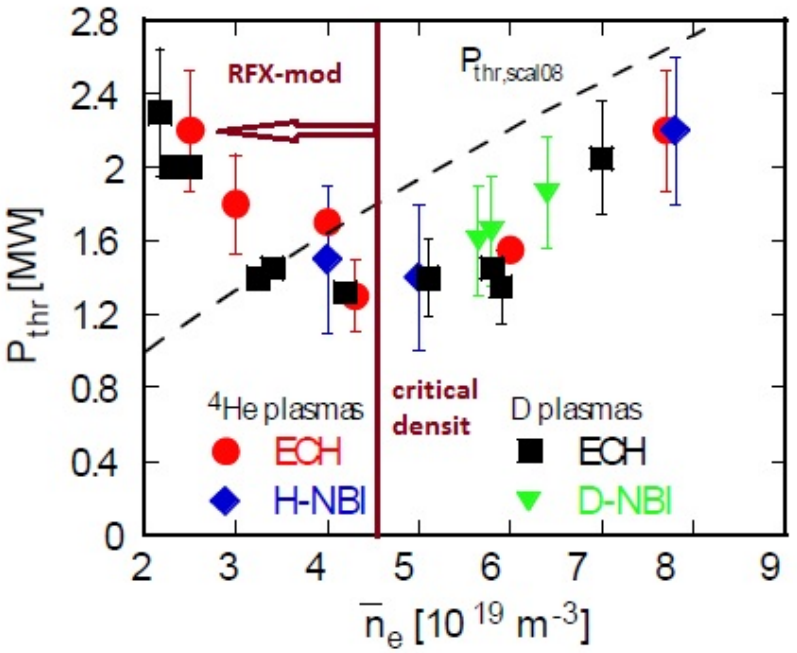

Figure 7.1: The dependence of the P_{thr} on average electron density for ASDEX-Upgrade. The critical density is represented by the violet vertical line and the violet arrow shows the region where the RFX-mod parameters are located. Figure taken from [72].

discussed later in this section). The threshold power is given by the following scaling law [70]:

$$P_{thr} = 4.9 \cdot 10^4 \cdot B_t^{0.8} \cdot \left(\frac{n_e}{10^{20}}\right)^{0.72} \cdot S^{0.94}, \tag{7.1}$$

where S is the plasma surface. However, this expression is valid just for density above the following limit [71]:

$$n_{crit} = 0.7 \cdot 10^{19} \cdot \left(\frac{I_p}{10^6}\right)^{0.34} \cdot B_t^{0.62} \cdot a^{-0.94} \cdot \left(\frac{R_t}{a}\right)^{0.4}. \tag{7.2}$$

For typical RFX-mod discharge, the density threshold is $n_{crit} = 10^{19}\ m^{-3}$. However, the average density can hardly exceed $5 \cdot 10^{18}\ m^{-3}$. Therefore the formula (7.1) is not valid for the RFX discharges.

The behavior of P_{thr} as a function of density is shown in Fig. 7.1. For $n > n_{crit}$, the density follows the scaling law in (7.1). For $n < n_{crit}$ the P_{thr} is increasing with decreasing density. There is a boundary limit for minimal density value below which the H-mode is not accessible anymore regardless the value of P_{sep}. This is caused by decoupling of electrons and ions in low density discharges [73].

This knowledge defines the approach in H-mode scenario development: one should maximize the density, minimize the P_{thr} and maximize P_{sep}.

The density can be increased if the first wall is properly conditioned. First of all, a boronization before every campaign is needed. The boronization enables reliable density control and reduces the impurity content in the plasma.

There are several possibilities to decrease the value of P_{thr}. First of all, it is preferred to use diverted plasma, even if the LH transitions are reported also in limiter configurations [74]. Another important factor is the use of deuterium as a process gas because the value of P_{thr} is lower in deuterium than in hydrogen from AUG [75] and JET [76]. The orientation of the toroidal magnetic field should be chosen in such a way that the ion ∇B drift has the direction towards X-point [3]. The DIII-D experience suggest locating the X-point close to the wall.

For the increase of P_{sep}, there is one critical ingredient: reduction of the plasma radiation. First important part of the puzzle is proper wall conditioning. It consists of the above mentioned boronization and helium glow discharge performed to clean the wall after every few discharges. The COMPASS experience suggests switching off the gas puff in the current flat-top phase. Admittedly, it would decrease the radiated power, however, this is in conflict with the high density requirement on RFX-mod. Next possibility, elaborated in part 7.4, is to take advantage from transient phases of the discharge when the value of P_{sep} can be temporarily increased. As the LH transition is a hysteresis process meaning that the value of $P_{thr}(L->H)$ is greater than $P_{thr}(H->L)$. In the other words, the value of P_{sep} needed to reach H-mode is higher than the value needed to sustain it as reported in [78].

Another, rather exotic method described in section 7.5 is based on biasing electrode inserted into the plasma.

7.3 H-mode Detection

This section is going to answer the following question: how to recognize H-mode First of all, let us show an example of one of the first COMPASS H-mode shots obtained in 2012. The waveform of plasma current, electron density and H_α is shown in Fig. 7.2.

The most typical sign of the LH transition is the fast drop (taking no more than 1-2 ms) of the H_α signal and reduced fluctuations after the transition. The transition is also followed by increase of plasma confinement (appearing as density increase in Fig. 7.2). Another clear sign of the LH transition is the decrease of the visible light emission from the plasma edge. Due to

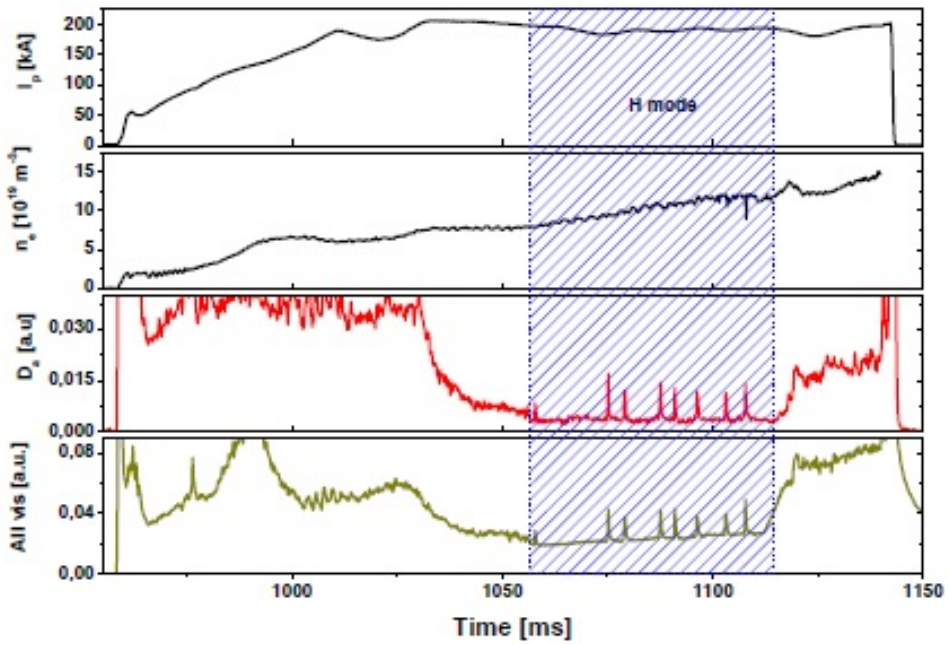

Figure 7.2: The time evolution of plasma current, average electron density and D_α radiation for COMPASS discharge 4334 with the LH transition. The peaks of D_α and all visible signal during the H-phase are Type-III ELMs. Image taken from [79]

improved confinement, one would expect also an increase of the soft X-ray emission, β_p or the core temperature.

Another figure of merit for the LH transition is the factor

$$H_{89} = \frac{\tau_E}{\tau_{89}} \tag{7.3}$$

where τ_{89} is the scaling confinement time for L-mode ohmic discharges [77] defined as

$$\tau_{89} = 3.8 \cdot 10^{-2} \cdot M^{0.5} \cdot \left(\frac{I_p}{10^6}\right)^{0.85} \cdot R_0^{1.2} \cdot a^{0.3} \cdot E^{0.5} \cdot \left(\frac{n_e}{10^{19}}\right)^{0.1} \cdot B_t^{0.2} \cdot \left(\frac{I_{OH}}{10^6}\right)^{-0.5}, \tag{7.4}$$

where M is the relative atomic mass. For RFX-mod, we consider the value equal to 1.8. I_{OH} is the ohmic heating power. After the LH transition, the H_{89} is expected to increase by a factor of 1.3-1.5.

7.4 LH Transition Attempts in Transient Phases of the Discharge

The LH transition in current flat-top phase has not been observed for any discharge in any plasma configuration. However, several suspicious events that could be the LH transitions were detected

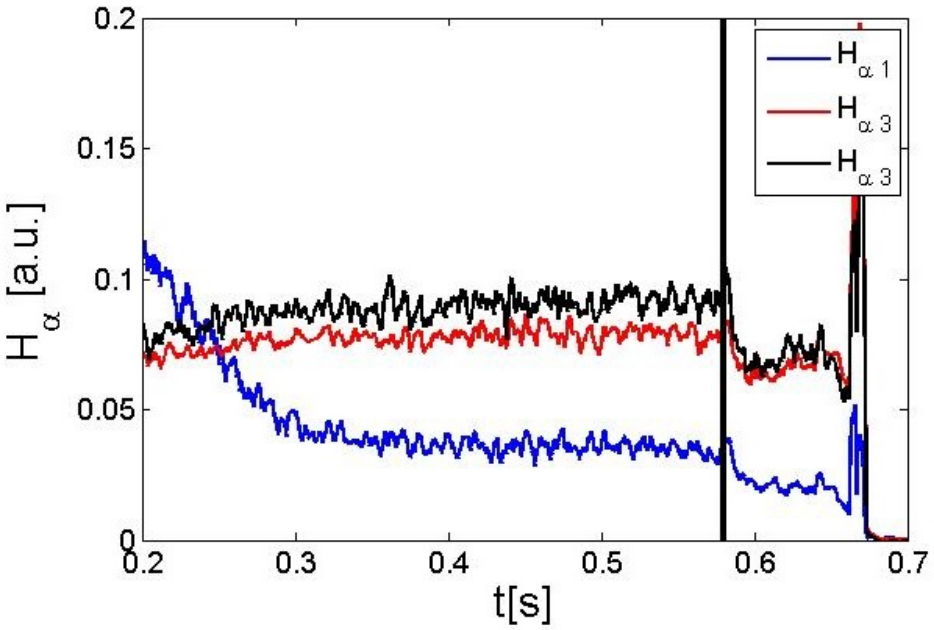

Figure 7.3: Time evolution of the H_α signal for discharge 36914. The controlled current ramp-down started at $t = 0.58$ s and the drop of H_α that could be connected to the LH transition appeared approximately 5 ms afterwards on all 3 channels measuring H_α signal.

during the controlled ramp-down phase of single null discharges. An example of such an event is in Fig. 7.3. In this case, the drop of H_α signal takes around 10 ms. The evolution of other plasma parameters is shown in Fig. 7.4: this discharge has higher plasma density than usually, the density does not decrease after the current ramp-down and the fast drop of H_α is accompanied by stronger SXR emission and H_{89} increase. The last two refer to improved confinement that accompanies the LH transition. Another important sign supporting the LH transition is the fact that the value of P_{sep} was significantly increased after the ramp-down started as shown in Fig. 7.5. Note that the LH threshold is depicted just as a figure of merit since the formula (7.1) is not valid in the density region on RFX-mod.

In the previous paragraph, we summarized all the arguments supporting the statement that the LH transition was observed in the ramp-down of 36914. On the other hand, there are also some opposing arguments. First of all, the drop of H_α is too long- around 10 ms. Instead, we would expect a drop taking no more than 2 ms. We have not observed any ELM's (we might have reached ELM-free H-mode). As the experiments were not reproducible and we observed such an event just in a few cases, it is not possible to make a clear conclusion: further validation, for example pressure profile measurement by Thomson scattering or observance of pedestal formation would be required.

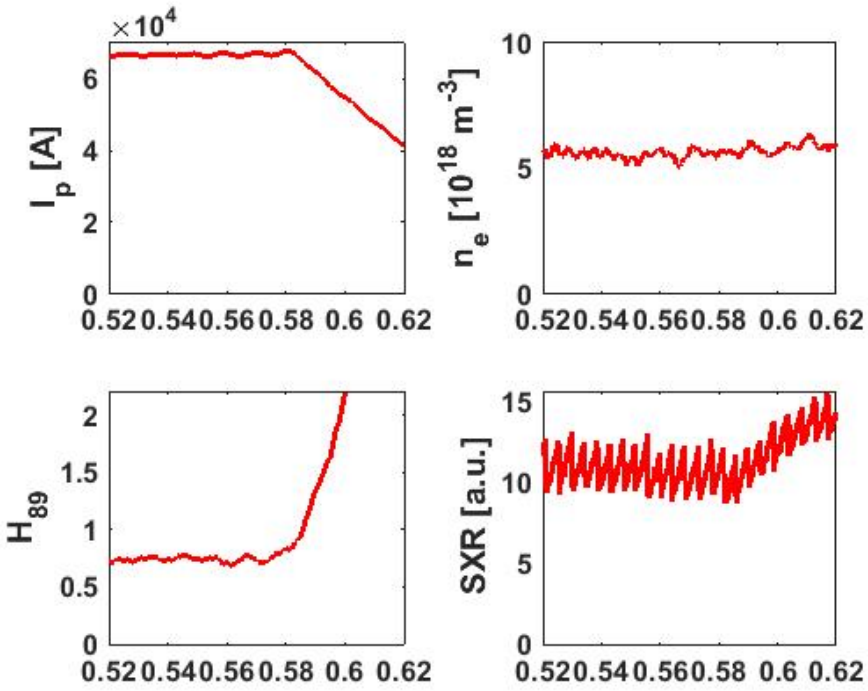

Figure 7.4: Time evolution of the SXR signal, electron density and H_{89} index during the current ramp-down.

7.5 Transition Attempts by Biasing Electrode

Since RFX-mod did not reach H-mode in the flat top phase, another attempt was made using biasing electrode. The idea behind is that the power flux through separatrix generating the radial electric field is replaced by biasing electrode inserted into the plasma and generating the radial field. Successful experiments were performed on Continuous Current Tokamak (CCT) [80], TEXTOR [81] and more recently from T-10 [82]. On the other hand, H-mode was not obtained on CASTOR [83] or ISTTOK [84].

In RFX-mod, the electrode is inserted from the lower side and kept at the edge of the plasma. The first results were presented in [85]. The position of the electrode with respect to the machine is shown in Fig. 7.6 and the plasma shape used for the biasing electrode experiments is in Fig. 7.7 The algorithm for plasma boundary reconstruction described in chapter IV was useful to control the plasma shape and estimate the depth of the electrode inside the plasma.

7.5.1 H-mode Access Condition Using Electrode

During autumn 2015, it was demonstrated that RFX-mod can reach H-mode using biasing electrode. However, there are two conditions that must be fulfilled. The first is related to the density,

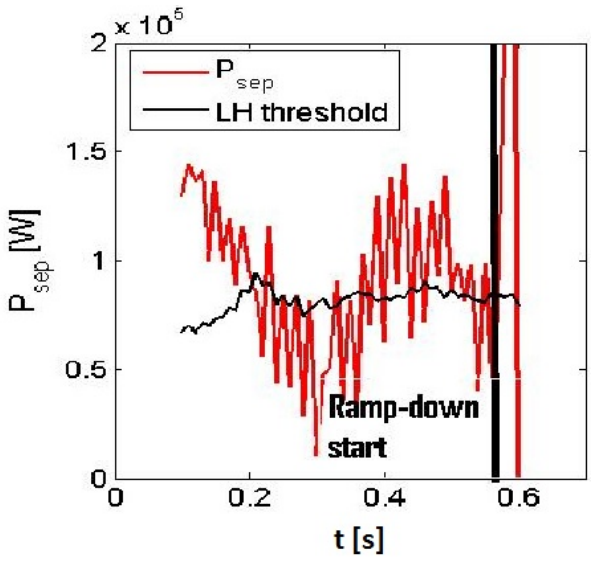

Figure 7.5: Time evolution of P_{sep} and the threshold for LH transition from (7.1).

which must be above the threshold as indicated in part 7.2. The second is related to the electrode voltage that must be high enough to generate sufficient radial electric field that provides the shear flow and generates the pedestal. The later condition is equivalent to the condition on the particle power flux through separatrix.

The density condition can be demonstrated on discharge 39090 and 39091. The only difference between these two discharges is the plasma density, which is much lower in 39090 as shown in Fig. 7.8. When the voltage is applied on the electrode (see Fig. 7.8), the LH transition appears in high density discharge 39091, but not in the low density case 39090. This demonstrates that the density is an important ingredient in the LH transition experiments.

Let us demonstrate the validity of the second condition on two discharges: 39082 and 39083. These two discharges have the same plasma shape, almost the same density when the electrode is switched on, but the voltage applied on the electrode is lower in case of 39083. The waveform of plasma density, H_α, electrode voltage and current are shown in Fig. 7.9. Despite the fact that all parameters but the electrode voltage are the same, the LH transition appears just in 39082. This type of behavior was observed also in other cases, therefore we conclude that the electrode voltage is a key ingredient in the LH transition.

7.5.2 Pedestal Formation and H-mode Confinement

As stated in the previous section, it is possible to reach H-mode on RFX-mod using biasing electrode. In addition to H_α drop, the pedestal formation was observed by a set of Langmuir probes

as shown in Fig. 7.10. In this figure, $r = 0$ corresponds to the separatrix position estimated by the boundary reconstruction algorithm from chapter IV, negative values of r indicate measurement inside the plasma and positive values outside the plasma.

However, despite the fact that we can clearly see the pedestal formation by the Langmuir probes, we did not observe improved confinement by inspecting of H_{89} as shown in Fig. 7.11 for discharge 39135. This behavior is suspicious and presently we do not have clear explanation.

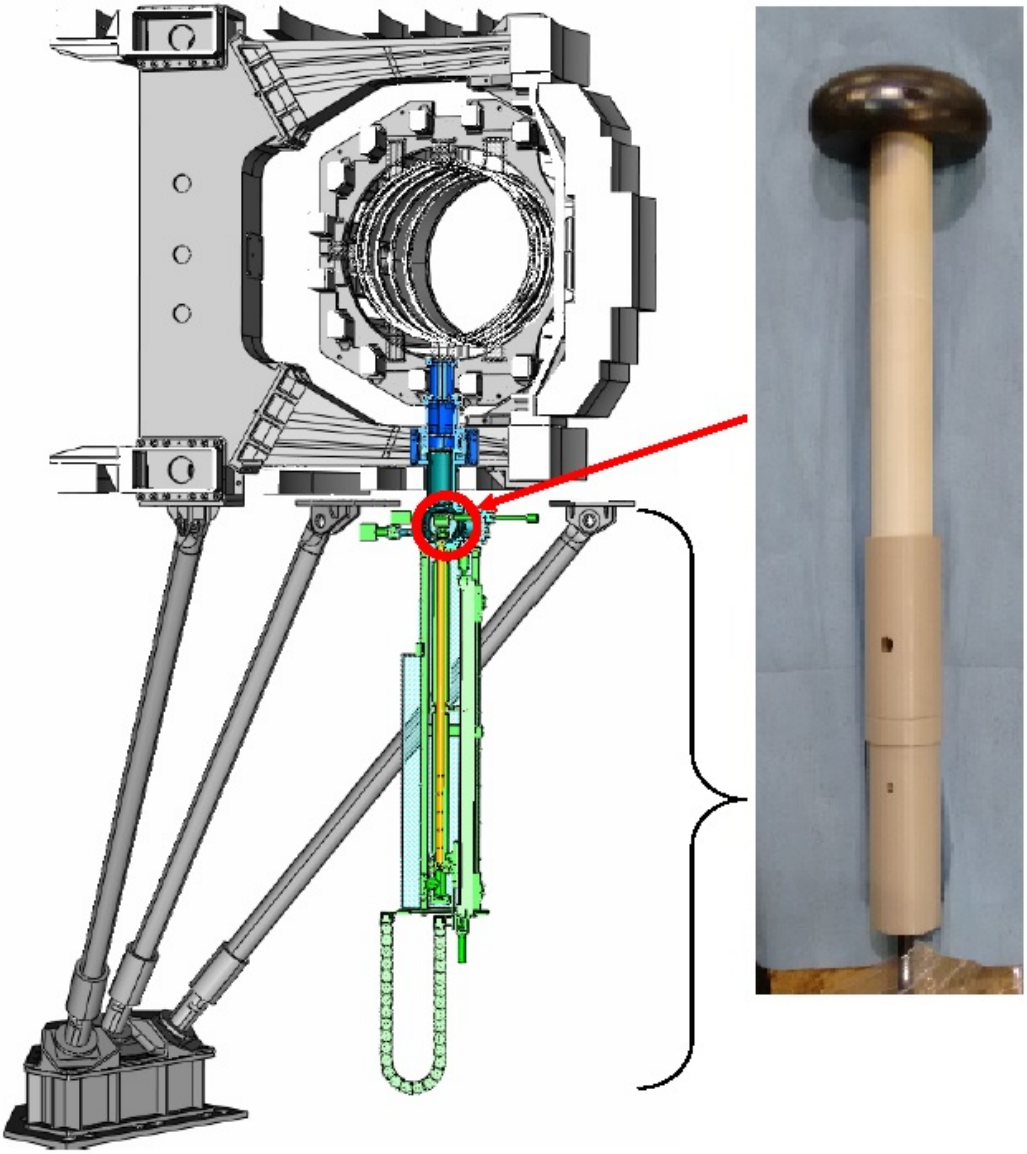

Figure 7.6: The position and construction of the biasing electrode installed on RFX-mod. Image taken from [85]

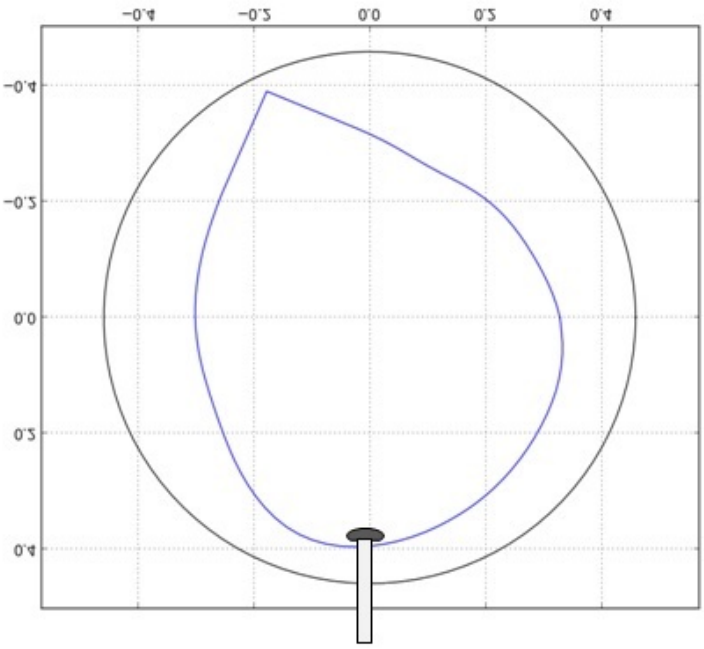

Figure 7.7: The plasma shape used for the biasing electrode experiments and the electrode location with respect to the plasma. Image taken from [85]

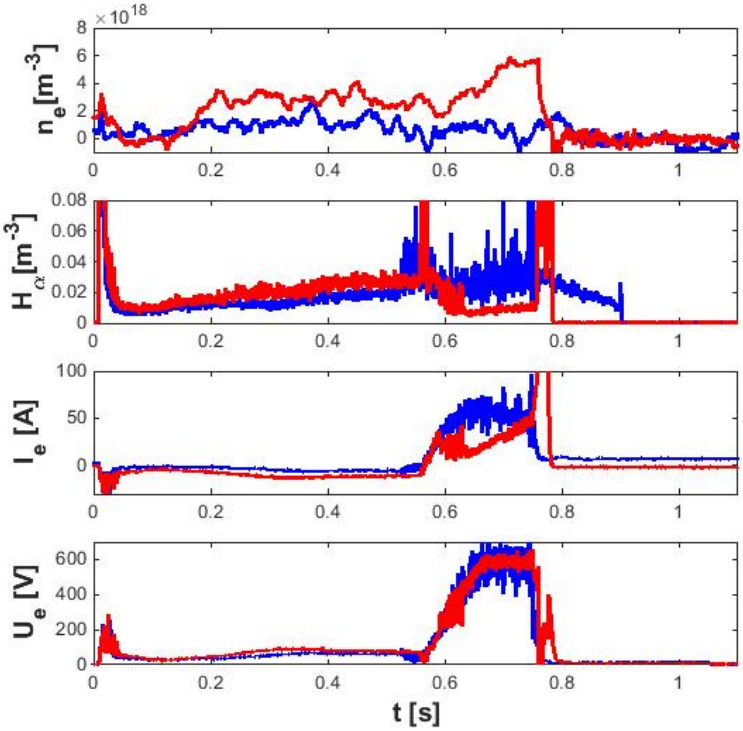

Figure 7.8: The waveform of electron density, H_α, electrode current I_e, and electrode voltage U_e for RFX-mod discharge 39091 (red) and 39090 (blue). Note that the LH transition appears in 39091 around $t = 0.6$ s

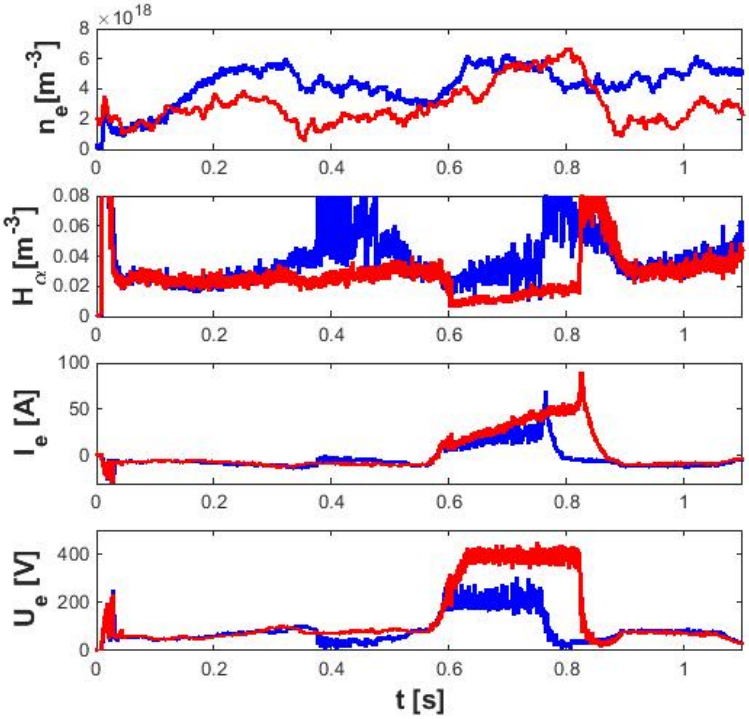

Figure 7.9: The waveform of electron density, H_α, electrode current I_e, and electrode voltage U_e for RFX-mod discharge 39082 (red) and 39083 (blue). Note that the LH transition appears in 39082 around $t = 0.6$ s

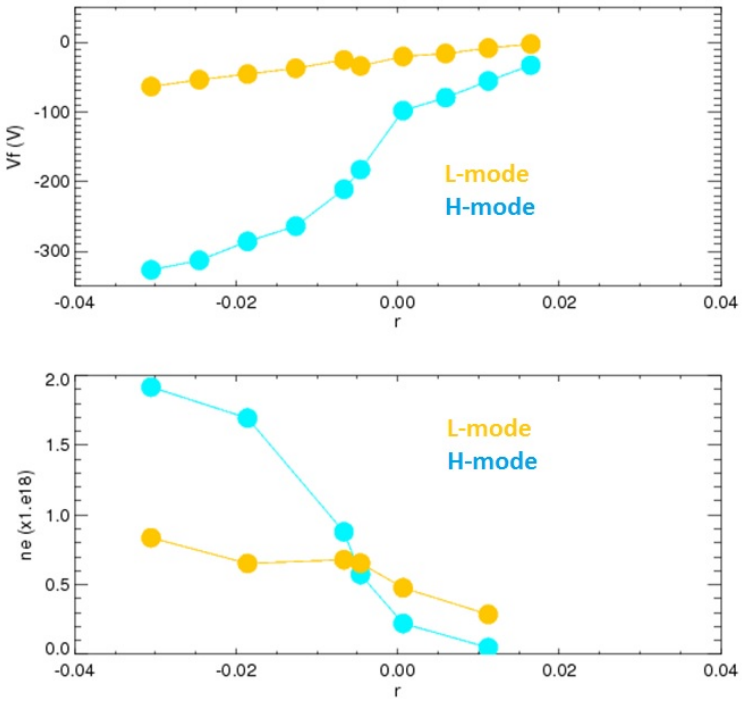

Figure 7.10: The pedestal measured by Langmuir probes in density and floating potential (Vf) in RFX-mod shot 39135. Image taken from [85]

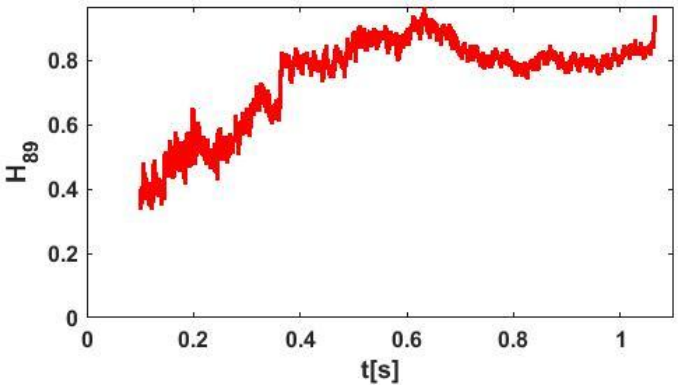

Figure 7.11: The time evolution of H_{89} in discharge 39135. The pedestal is formed at $t = 0.6$ s. However, we do not see any sign of LH transition on H_{89}.

Part III

Disruption Prediction by Real Time Plasma State Estimator RAPTOR

CHAPTER VIII

The RAPTOR Code

8.1 Motivation

In tokamak operation, it is desired to have as much information about plasma state (for instance radial profiles of plasma current, density and temperature) as possible in real time in order to control the plasma and avoid disruptions. The control is becoming more and more essential while operating in more advanced scenarios: in old and small devices such as ISTTOK, the feedback control of the plasma had not been important. In present-day devices such as RFX-mod, TCV or ASDEX Upgrade it is essential to control the plasma boundary to avoid the plasma wall contact and consequent damage of the plasma facing material. It is also desirable to suppress the tearing modes by for example ECCD power deposited at the island location [86] and pace the sawteeth crashes [87], [88] that seed the tearing modes. Another important point is the ELM mitigation [17], [18]. In present day devices, disruptions are to some extent acceptable, even if the avoidance is advantageous. The profile measurement of the above mentioned quantities needed to deal with all these tasks is recovered from complicated real time diagnostics systems.

In future devices such as ITER and even more DEMO, the control of the above mentioned profiles and instabilities will become critical: large portion of discharges will be performed in steady state advanced scenario, thus the feedback control of the current profile will become mandatory. The suppression of the tearing modes will be necessary to achieve desired plasma parameters in terms of confinement. Disruptions will not be allowed. To justify all these requirements, a detailed real time knowledge of the plasma internal profiles is needed. However, there will be just very limited set of diagnostics due to harsh enviroment in the reactor, reliability, and cost of the device. Additionally, the profile diagnostics are usually not very precise and can not measure some quantities that are essential for the plasma operation in advanced regimes, for example the bootstrap current fraction.

For the above mentioned reasons, a code to complement the simple set of future real time diagnostics and gain the missing information was developed. The code is called RApid Plasma Transport simulatOR (RAPTOR). The core of the code is a real time solver of a simplified set of transport equations. The code input consists of a few simple diagnostics (see the description given later) and the output can be basically any quantity related to the current or electron temperature profile. Detailed description of this code is given in [89], [90]

8.2 Physical Model in RAPTOR

Since RAPTOR is a code focused on real time applications, not all physical effects affecting the plasma state can be taken into account, just the most important ones for the profile computation must be picked. There are several full transport offline models such as ASTRA for fixed boundary problems [93] or CORSICA [94] and CRONOS [95] for free boundary problems. However, due to extensive requirements for computational time, these models are not suited for real time application.

For RAPTOR, the following simplifications have been made [90]:

- **Limited set of included quantities:** The RAPTOR code evolves just the poloidal flux and electron temperature solving the transport equations for these quantities. Other profiles, such as both electron and ion density, impurity or ion temperature profiles are fixed. As the most important physics related to the current profile evolution and the evolution of plasma instabilities is governed by electron temperature profile and poloidal flux diffusion and their non-linear coupling, this assumption is reasonable. Detailed description and validation of this choice against ASTRA is given in [90]. Presently, there is an ongoing project focused on electron density evolution inclusion.

- **Fixed equilibrium assumption:** RAPTOR does not include the evolution of the flux surface shape meaning that the form of $\psi(R, Z)$ is constant in time. However, the quantity $\psi(\Phi)$, where Φ stands for toroidal magnetic flux, is free to evolve to cover events such as current profile redistribution or safety factor evolution. Presently, a scheme for coupling of equilibrium solver with RAPTOR is being developed. Similar work for post-discharge analysis is done for coupling the current diffusion equation with an inverse Grad-Shafranov solver as reported in [96].

- **Ad-hoc transport model:** The electron energy transport coefficient can be described in two ways. The simplest, which is a purely ad-hoc equation aimed at very simplified modeling,

model follows equation

$$\chi_e = \chi_{neo} + c_{ano}\rho q F(s)(T_{e0}[keV])^{c_{T_e}} + \chi_{central} e^{-\rho^2/\delta_0^2}, \tag{8.1}$$

where χ_{neo} is a neoclassical transport term, c_{ano} is the anomalous transport coefficient term and $F(s)$ is a shear-dependent transport function accounting the fact that the transport is reduced for very low or negative shear. $\chi_{central}$ is an ad-hoc parameter representing the decreased confinement in the core and δ is the width of the region with decreased confinement. The temperature dependence $(T_{e0}[keV])^{c_{T_e}}$ was added to include the effect of confinement degradation at higher input powers. The typical value of c_{T_e} is between 1 and 2.3 [91].

However, this simplified model is not sufficient to deal with more complicated plasmas like on ASDEX-Upgrade. Therefore more complex model called Bohm-Gyro-Bohm (BgB) was implemented into RAPTOR. Details about this model can be found in [97]. In this case, the electron transport coefficient

$$\begin{aligned} \chi_e &= c_b \cdot \chi_e^B + c_{gb} \cdot \chi_{GB} \\ \chi_e^B &= \alpha_B \frac{cT_e}{eB} \frac{a\nabla p_e}{p_e} q^2 \\ \chi_{GB} &= \alpha_{GB} \frac{cT_e}{eB} \frac{a\nabla T_e}{T_e} \rho^*, \end{aligned} \tag{8.2}$$

where $\alpha_{B,GB}$ are numerical constants, ρ^* is the normalized electron Larmor radius, a is the minor plasma radius and c is a constant. The term χ_{GB} is significant just close to the plasma core, the χ_e^B term in all other parts of the plasma. Note that also BgB is a simplified, heuristic model that does not capture the reality of the transport physics in a wide variety of regimes. Yet its relative simplicity still make it useful for this type of simulations. More complicated models can be added in the future, as mentioned in section 11.2.

In addition to the inclusion of these two models, RAPTOR can also deal with edge transport barrier in H-mode with user defined pedestal height.

- **Heating and Current Drive Source Parametrization** The radial deposition profile of external power or current drive sources in the plasma is parametrized by a Gaussian profile.

Let us summarize the set of transport equations solved by RAPTOR using the above-listed simplifications. The magnetic flux follows

$$\sigma_{||}\frac{\partial\psi}{\partial t} = \frac{R_0 J^2}{\mu_0 \rho}\frac{\partial}{\partial\rho}\left(\frac{G_2}{J}\frac{\partial\psi}{\partial\rho}\right) - \frac{V'}{2\pi\rho}(j_{bs} + j_{aux}), \tag{8.3}$$

where $\sigma_{||}$ is the parallel conductivity,

$$\rho = \sqrt{\frac{\Phi}{\pi B_0}} \tag{8.4}$$

is identified as "effective minor radius",

$$J = \frac{\Phi}{R_0 B_0} \tag{8.5}$$

$$V' = \frac{\partial V}{\partial\rho}, \tag{8.6}$$

where V is the plasma volume and

$$G_2 = \frac{V'}{4\pi^2}\left\langle\left(\frac{(\nabla\rho)^2}{R^2}\right)\right\rangle. \tag{8.7}$$

j_{bs} is the bootstrap current density and j_{aux} is the current driven by external heating sources. The electron temperature is governed by equation

$$V'\frac{\partial}{\partial t}(n_e T_e) = \frac{\partial G_1}{\partial\rho}V' n_e \chi_e \frac{\partial T_e}{\partial\rho} + V' P_e, \tag{8.8}$$

where P_e is the external heating source power and

$$G_1 = \langle(\nabla\rho)^2\rangle. \tag{8.9}$$

Due to the fixed equilibrium assumption, the equilibrium-related quantities J, V', $G_{1,2}$ are constant during the RAPTOR simulation. Plasma density is the code input and its profile is fixed. The arbitrary parameters in (8.1), χ ($c_{ano}, \chi_{central}$, δ) are fixed as well, but their input heating power dependency can be included.

The spacial discretization of the set of partial differential equations (PDE) (8.8) and (8.3) is carried out with finite elements. Using this discretization, the original set of PDE's is transformed into a set of ordinary differential equations (ODE). The choice of basis functions is arbitrary, but the cubic B-splines were chosen to guarantee continuity up to the second derivative. The code contains a numerical scheme to solve the set of the ODE's (both (8.8) and (8.3)) iteratively by series of Newton-Raphson iterations at each time step. The model inputs are typically the plasma current, plasma density, toroidal magnetic field, Z_{eff} and the trajectories of the heating and current drive

power. It can be used to validate the simulations (for example adjusting the choice of the transport coefficients in (8.1)), (8.2) or optimize the trajectories of plasma state evolution (for instance the current ramp-up scenario). Let us call this way of RAPTOR operation predictive regime.

The other possibility is to use RAPTOR as a real time plasma state observer. In this case, one uses the a strategy based on extended Kalman filter to correct the plasma state using a real time temperature measurement. The detailed description is in [92].

8.2.1 Sawtooth Reconnection Model

The profiles of T_e and ψ are significantly modified by the sawteeth reconnections.To involve this significant effect and improve the plasma state estimate by RAPTOR, a module evolving the sawteeth reconnections was developed within [98]. The module includes two models of the sawtooth reconnection: Kadomtsev's model of complete reconnection [99], and the Porcelli's model of incomplete reconnection [100], which is an extension of the Kadomtsev's model.

First of all, let us describe the principle of the Kadomtsev's model, which stands on two assumptions. The first of them suggests that the reconnection appears between helical flux surfaces of the same helical flux located on the opposite sides of the $q = 1$ flux surface. The helical flux ψ_* is defined as

$$\psi_*(r) = \int_0^{r^2} \left(\frac{1}{q} - 1 \right) dr'. \tag{8.10}$$

The radial profile of the helical flux ψ_* is shown in Fig. 8.1. The Kadomtsev's model suggests that all the flux surfaces with $\psi_* > \psi_*(r = 0)$ are reconnected.

The second assumption of the Kadomtsev's model is that the toroidal magnetic flux between the reconnecting flux surfaces is conserved. To justify this assumption, the radius r of the new flux surface emerged from reconnection of a flux surface on the outer side of the $q = 1$ at flux surface with the one on the inner side is

$$r = \sqrt{r_e^2 - r_i^2}, \tag{8.11}$$

where r_e is the flux surface on the outer side of $q = 1$ flux surface and r_i is the radius on the inner side of the $q = 1$ flux surface. Using such a reconnection model, a curve similar to ψ^f in Fig. 8.1 is reproduced.

The comparison with the experimental data showed that the Kadomtsev's description is not sufficient. Thus, the following modification was proposed by Porcelli [100]: the reconnecting surfaces are of the same helical flux $\psi_*(r_1) = \psi_*(r_2)$ and $r_2 - r_1 = w_{crit}$, where w_{crit} is the critical width

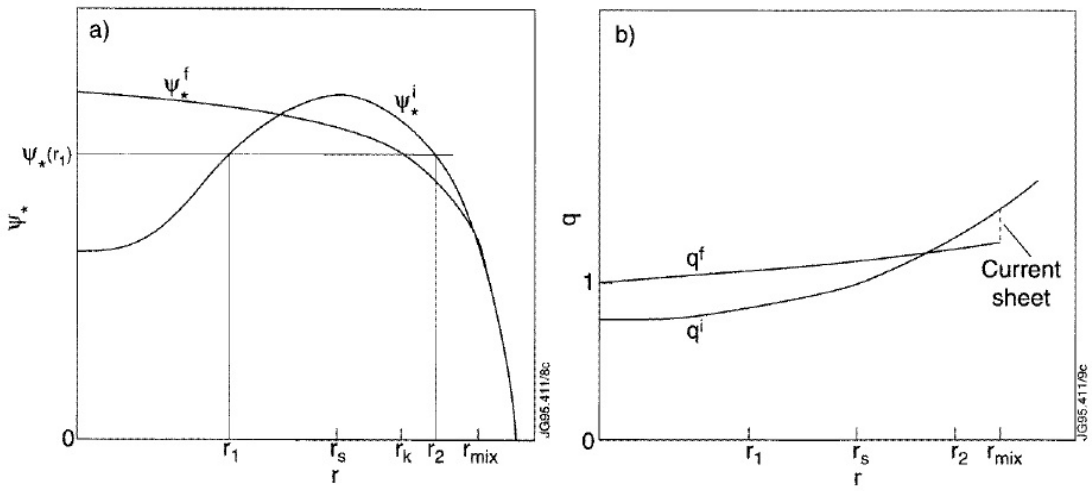

Figure 8.1: The radial profile of ψ_* (left plot) and q (right plot) before (superscript i) and after (superscript f) the sawtooth crash according to Kadomtsev's model. Figure taken from [100].

of the reconnecting region. As soon as the island width reaches this value, a magnetic turbulence causing the reconnection appears.

RAPTOR contains a sawtooth reconnection module described in [98]. RAPTOR performs the sawtooth crash reconnection if the shear defined as

$$s = \frac{r}{q}\frac{dq}{dr} \tag{8.12}$$

at $q = 1$ flux surface exceeds a critical value s_{crit}. The critical value is typically around 0.2. After that, the Porcelli's or Kadomtsev reconnection is performed by the code. The number of reconnection surfaces is 1001 in the present version of the code. This number was chosen at the beginning of the sawtooth module development to avoid problems with limited resolution. The possibility of reduction is studied in section 9.5.2.

One of the critical aspects of this model is the localization of the $q = 1$ flux surface. For sufficient precision, a dense RAPTOR spacial ρ grid is needed. This requirement is in conflict with the requirement of good time resolution. This thesis presents the best compromise found for the RFX-mod in section 9.5.1.

8.3 Disruptions Prediction by Sawtooth Period Monitoring

The real time profile reconstruction by RAPTOR has many various applications. One of them, the real time disruption prediction by sawteeth period monitoring, was elaborated within this thesis.

8.3.1 Present Disruption Prediction Methods

Before describing the method of disruption prediction by RAPTOR, let us give a brief introduction of present disruption prediction methods and describe their limitations.

Most of present disruption prediction methods are based on neural network trained on a set of disruptive and non-disruptive discharges (these methods are also referred as learning methods). The methods based on neural network are capable to predict disruption several hundreds of ms before with success rate around 90 %. Details are reported for example in [101] from AUG where 13 plasma diagnostics signals were used. Afterwards, 99 disruptive and 386 discharges were used to train the neural network. The resulting network was tested both disruptive and non-disruptive discharges not used to create the neural network. The missed alarm rate was 15 % and the fake alarm rate was 1 %. Similar application is reported from JET in [102] or in [103]. A nice summary of present day methods and some applications of learning algorithms on JET are given in [104]. This class of methods gives sufficiently reliable disruption prediction, around 90 % several hundreds of ms before the disruption, for present day devices. However, there are several major drawbacks of the learning methods.

First of all, the success rate around 90 % is not sufficient for ITER. The situation for reactor is even worse- no disruptions will be tolerated. Second, general disadvantage of the learning methods is that they are not transferable to another device. In other words, every machine needs its own shot database to train its own neural network. When the neural network trained for ASDEX-Upgrade was tested on JET and opposite, the success rate was below 70 % in both cases as reported in [105].

In addition, the neural network training requires tens- few hundreds of discharges, some of them must be disruptive. This is in conflict with no-disruption requirement for reactor. Due to these limitations, it is necessary to develop a method that would have higher success rate and would be transferable from one device to another. The later requirement indicates that the method must be physics based.

One of the possible candidates is disruption prediction by plasma state monitoring by RAPTOR or similar code. It can be based on two principles:

- Compare the plasma state estimated by RAPTOR with known MHD limits that can be computed for any device by MHD codes such as MARS [106]. In such a way, the limit can be found for β_N, for q_{95} vs. l_i diagram or for q_{95}. However, such an approach does not work in all situations. For example, the density limit can not be predicted by such an approach. Also,

this way of disruption prediction can not handle some off-normal situations (like penetration of dust into the plasma etc...). Therefore the option below is considered as well.

- The state observer (RAPTOR) estimates state of a normal, unperturbed plasma. As disruption is preceded by some plasma perturbation (mode, impurity accumulation etc...) that is not reflected in the state observer, one can use the discrepancy between the state observer estimate and experimental measurements as a feedback variable for disruption prediction. An example of application of such method is given for three devices in this thesis: RFX-mod, TCV, and ASDEX-Upgrade.

8.3.2 Sawteeth Behavior before Disruption

As stated in previous section, the disruption can be predicted by comparison of RAPTOR and real plasma state. For this purpose, we need a quantity that can be estimated by RAPTOR, easily detected in the experiment, and changes significantly before disruption. One of the candidates is the sawteeth period.

The sawteeth behavior significantly changes before the disruption caused by RWM, LM, density limit or impurity accumulation. It has been extensively observed on many devices worldwide. Let us demonstrate this property on a RFX-mod discharge with very low edge safety factor (q(a) < 2). The waveform of the plasma current, edge safety factor, 2/1 RWM amplitude and the soft X-ray (SXR) signal are shown in Fig. 8.2 The feedback control of the 2/1 mode is switched off during the current flat-top phase. One can see that the mode starts growing immediately after that. At the beginning of the current flat-top phase, the sawteeth behavior seen on the soft X-ray signal was regular with approximately constant period and amplitude. After the 2/1 mode starts growing, the sawteeth behavior changes in such a way that the crashes are becoming smaller, but more frequent until complete disappearance followed by a disruption.

Similar behavior was observed in TCV before the density limit disruption [107] discharges. The evolution of the sawteeth crashes properties is very similar to the one observed on RFX-mod for RWM: until the density reaches certain value, the sawteeth behavior does not change much as depicted in Fig. 8.3. Afterwards, at ($t = t_1$) the sawteeth behavior turns to be irregular and due to further increase of density the sawteeth crashes disappear at ($t = t_2$). A density limit disruption follows 100 ms later.

This property of the sawtooth instability inspired a new, real time physics based disruption prediction method introduced in this thesis. This method is based on the real time sawteeth period

monitoring. As RAPTOR does not contain any information about the mode perturbing the plasma, it predicts the sawteeth period for unperturbed plasma. In the other words, RAPTOR expects the regular sawteeth behavior seen before the feedback control is switched off in Fig. 8.2 or before $t = t_1$ in Fig. 8.3 even after the perturbation significantly modifies the experimental sawteeth behavior. One way to detect the presence of the perturbation is to compare the sawteeth period estimated by RAPTOR with the experimental one. If the normalized difference

$$\frac{|T_{SXR} - T_{RAPTOR}|}{T_{RAPTOR}} > R_{ST}, \tag{8.13}$$

the disruption alarm is activated. The choice of R_{ST} is arbitrary and depends on the experimental conditions. The requirement of early disruption prediction suggests picking a value close to 0. On the contrary, as the fake alarms must be avoided, we usually choose higher value depending on the quality of agreement between RAPTOR and experiment and the capability of the sawtooth detection algorithm to catch all the sawteeth crashes. This thesis explores the method of disruption prediction for RFX-mod, TCV and gives the first examples from ASDEX-Upgrade.

8.3.3 Physical Explanation of the Sawtooth Disappearance

The sawteeth disappearance observed before the disruption can be explained by three effects, possibly combined. The first, suggested in [107] and in [108] is valid for the discharges with high plasma density or high impurity content. When a limit core density approaches a critical value, the transport properties related to trapped electron mode or ion temperature gradient change between $\rho = 0.3 - 0.5$ [108]. Consequently, the core density increases and the increased radiation from the core decreases the central temperature, flattens the temperature profile and consequently decreases the conductivity of the central plasma region. The decreased core conductivity modifies the current profile: more current is carried by the edge parts of the plasma. Consequently, the $q = 1$ flux surface moves closer to the magnetic axis and the sawteeth become smaller. Smaller sawteeth cause further accumulation of the fuel in the core enhancing the original cause of the sawteeth amplitude decrease. This process continues until complete sawteeth disappearance followed by disruption, that is caused by high density induced locked mode. The same effect appears in case of impurity accumulation. It can even appear at smaller density, but in a similar way: radiation reducing core temperature.

However, this theory does not provide full picture of the physics behind, since the sawteeth disappearance is observed also in low density discharges where the core temperature decrease described above does not appear. In this situation, two effects related to the MHD modes play role.

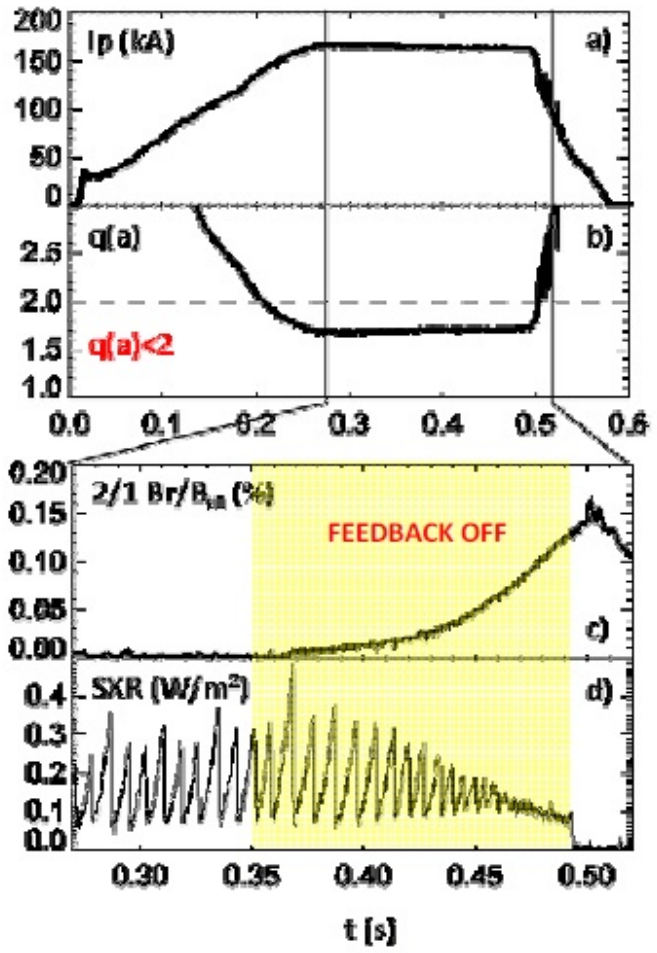

Figure 8.2: An example of the modified sawteeth behavior during the growth of the 2/1 RWM on RFX-mod. Image from [109].

The first effect is the interaction of 2/1 mode with the Shafranov shift (1/0 mode). The coupling of 2/1 with 1/0 produces the 3/1 and 1/1 sidebands. The sawtooth crash corresponds to the 1/1 internal mode, therefore it is affected by the interaction of 2/1 mode with the Shafranov shift. The sawtooth crash appears as soon as a critical 1/1 amplitude is reached. Some stationary part of the 1/1 amplitude is already generated by the coupling of 2/1 mode with the Shafranov shift. After an unaffected sawtooth crash, the 1/1 mode vanishes. However, since a stationary part of the 1/1 mode amplitude is generated by effects that do not disappear with the sawtooth crash, the crash itself becomes smaller. If the amplitude of the 1/1 sideband generated by the Shafranov shift and 2/1 becomes too large, the sawteeth disappear completely. This behavior was also reproduced by PIXIE3D simulation [110].

The second effect related to the MHD modes is related to the confinement degradation caused by the mode. Due to the profile stiffness, the presence of a mode also reduces the core temperature

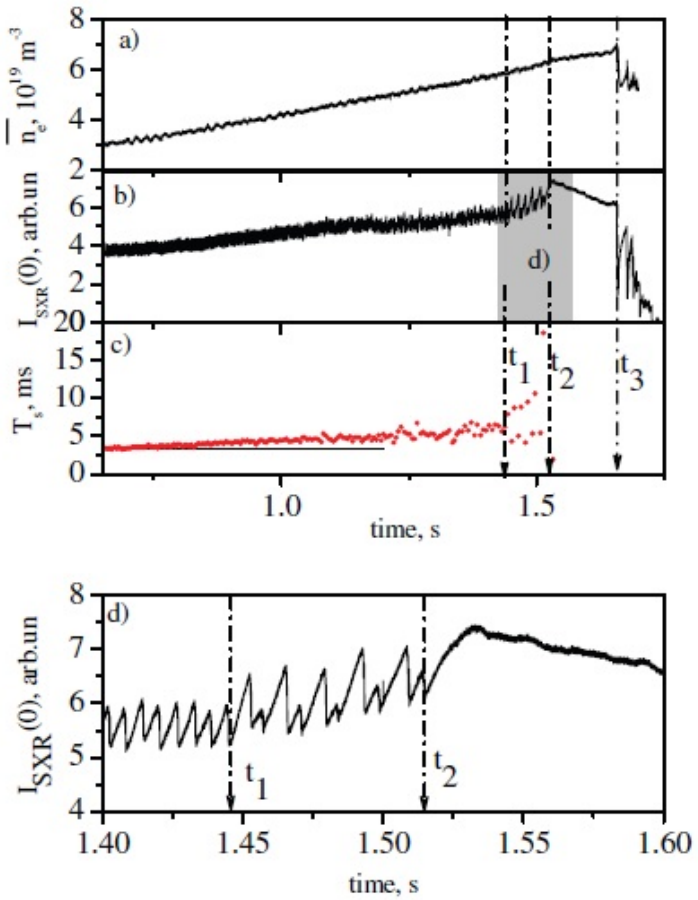

Figure 8.3: The time evolution of (a) mean plasma density (b),(d) the core SXR and (c) the sawteeth crash period for TCV shot number 45180 terminated by a density limit disruption. Image taken from [107].

and flattens the temperature profile (see for example [111]). The temperature profile flattening caused by NTM mode has the same effect on the sawteeth behavior as the flattening caused by fuel accumulation described above.

These three effects are combined and the role of each of them depends on experimental conditions.

CHAPTER IX

RAPTOR on RFX-mod Tokamak for Disruption Prediction

This chapter will focus on practical aspects of RAPTOR implementation on RFX-mod and tests of the disruption prediction method based on sawteeth period monitoring in discharges terminated by a RWM. One section will be also dedicated to optimization of RAPTOR settings in order to reduce the execution time.

9.1 Real Time Signals Preparation

As a first step of RAPTOR implementation on RFX-mod, some real time diagnostic essential for RAPTOR was prepared. In particular, a real time method to estimate the plasma density and temperature had to be found. In this work, we focused on high density discharges with high SXR signal that enables reliable temperature measurement and sawtooth detection.

9.1.1 Core Temperature Measurement Using SXR

The core electron temperature on RFX-mod is estimated using double filter method. This section gives basic description of this technique, details can be found in [112] and in [113].

The basic principle of this measurement is that the intensity of the continuous SXR radiation strongly depends on the electron temperature. The ratio of two SXR intensities measured by two detectors observing plasma through filters of different thickness is related mainly to the highest electron temperature along the line of sight. In RFX-mod, two aluminum filters of convenient thickness are used and the temperature is derived from the signal ratio. This method is simple and real time applicable.

9.1.2 Plasma Density Estimation

Another indispensable diagnostic for real time RAPTOR is the density measurement. Even if the measurement of density profile is preferable, the measurement of averaged density is a viable solution for the RFX-mod experiments. The most common diagnostic for line averaged density measurement, the interferometry, is installed on RFX-mod, but can not be used as a real time signal since it would require new hardware development. Therefore we implemented an alternative, approximate method combining existing real time measurements of β_p, T_e, plasma current and plasma minor radius. Using the definition of β_p, we arrive at the relation

$$\frac{\beta_p B_a^2}{2\mu_0} = \langle nT \rangle = \xi \cdot \langle n_e T_e \rangle, \tag{9.1}$$

where ξ is the constant representing the impact of ion pressure. The edge magnetic field is

$$B_a = \frac{\mu_0 I_p}{2\pi(a - \delta_a)}$$

where δ_a is the shift of the plasma centre measured from the vessel centre. Note that this approximation is valid just for circular discharges. The electron density could be easily calculated if the profile of T_e was known. As only the value of the core temperature can be measured, another simplification exploited later in the paragraph is needed to obtain the final form used in the experiments:

$$\langle n_e \rangle = K \cdot \frac{\beta_p I_p^2}{T_e^{core}(a - \delta)^2} \tag{9.2}$$

with K being the constant of proportion between $\langle n_e \rangle$ and the quantities on the right hand side of (9.2). Admittedly, this approach is not optimal as K depends on the shape of the $n_{e,i}$, T_e, T_i radial profile and the energy exchange between electrons and ions. Thus the value of K must be found by direct comparison of the result of (9.2) with the offline interferometric measurement. Luckily, K is almost the same for all circular discharges of interest in one experimental session, so the estimate of $\langle n_e \rangle$ by (9.2) is reasonable. An example is shown in Fig. 9.1. The agreement between the density estimated by interferometry and the one by (9.2) is sufficient at least for the RAPTOR experiments performed on RFX.

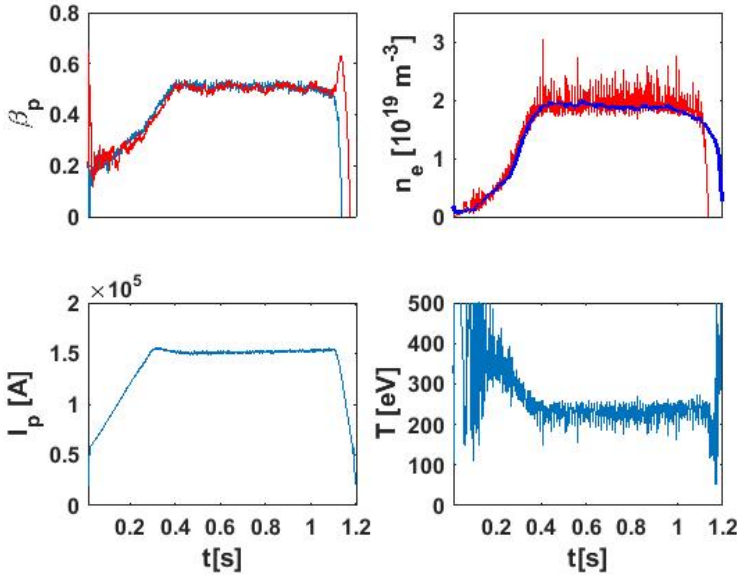

Figure 9.1: The time evolution of the real time β_p signal (red), the offline β_p signal (blue), real time plasma density provided by (9.2) (red) with the plasma density by interferometric measurement (blue). The other two waveforms represent the plasma current and the electron temperature measured by the double filter method. All quantities are plotted for the RFX-mod discharge number 38444.

9.2 Real Time Sawtooth Detection

Another essential quantity that must be determined in real time for the disruption prediction experiments is the sawteeth period. The most convenient diagnostic for this purpose is the SXR channel collecting signal from the plasma core. The sawteeth crashes can be easily seen by eye, but the real time detection is not based on straightforward criteria. Within this thesis, a simple, real time applicable method based on the following three criteria was developed:

1. The difference between the signal N samples behind and the instant SXR signal is above certain level L_1:

$$S(i-N) - S(i) > L_1. \tag{9.3}$$

The value of N represents usual number of samples inside the fast drop phase of SXR signal appearing immediately after the crash, on RFX-mod the value between 4 and 10 was used.

2. The $S(i-N)$ is a local maximum of the SXR signal:

$$S(i-N-1) < S(i-N) > S(i-N+1) \tag{9.4}$$

3. The last condition is based on comparison of the signal S with the moving average S_{MA} computed from P past samples of S. The number P is chosen to cover the time window $2-3$ times longer than the longest sawteeth period: the individual sawteeth crashes should not be visible on this signal. In case that

$$S(i-N) - S_{MA}(i-N) > L_3, \tag{9.5}$$

this condition is true.

However, the real time sawtooth crash detection is not as straightforward as it seems from the list above for several reasons: the algorithm must be able to detect a large range of sawtooth amplitudes, from tiny ones to huge ones. This task is getting even more complicated due to the presence of noise. The noise may be confused with a sawtooth crash if the algorithm is too sensitive. The sensitivity is given by the choice of L_1 and L_3, low values mean sensitive algorithm. Another problem of combination of sensitive algorithm with noise arises from the possibility of multiple detection of large sawteeth crashes. On the contrary, if the algorithm is less sensitive, small sawteeth crashes are often missed. Two other conditions had to be added to deal with these effects and additional problematic issues:

- **Multiple sawtooth detection:** the issue of multiple detection of one sawtooth crash was solved by adding a condition for minimal gap between the sawteeth crashes. If the conditions (9.3), (9.4), and (9.5) are fulfilled, the time difference between the last sawtooth crash and the detected one is computed. If the difference is below Δ_t value, the new crash is rejected. For RFX-mod, $\Delta_t = 3$ ms.

- **Irregular sawteeth behavior:** One of the problems of the algorithm using just (9.3), (9.4), and (9.5) is that it often misses a sawtooth crash in case that the behavior is irregular. A good example is in Fig. 8.3 between t_1 and t_2, where a small sawtooth crash alternates to the big one. Due to condition (9.5), the small crashes can be missed. If missed, the estimated sawteeth period would be doubled. This would lead to unacceptable error in the disruption alarm condition (8.13). An ad-hoc solution for the RFX-mod to deal with this issue was used: the new estimate of the sawteeth period is compared with the average period of the last few crashes. If the new detected period T_{new}

$$1.5 \cdot T_{old} < T_{new} < 2.1 \cdot T_{old},$$

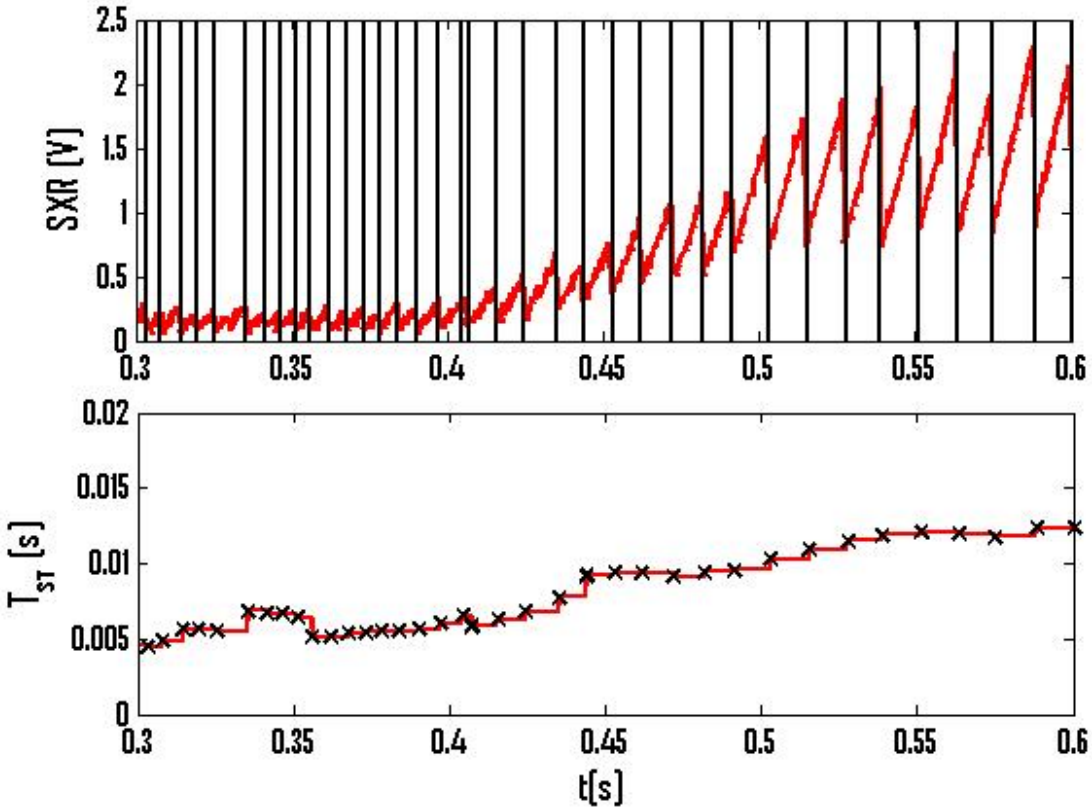

Figure 9.2: In the upper plot, the SXR signal in RFX-mod discharge 38351 is shown (red). The sawteeth crashes detected by the real time algorithm are tagged by black vertical lines. Note a multiple detection (eliminated by condition for minimal time difference between sawteeth crashes mentioned above) of one sawtooth crash immediately after t =0.4 s. The sawteeth period T_{ST} estimated by the method described in this section is shown in the lower plot.

the estimate of T_{new} is corrected as follows:

$$T^*_{new} = T_{new}/2. \tag{9.6}$$

The division by 2 is used due to the fact that one period was probably missed. This solution is relevant since no rapid changes in the sawteeth behavior have been observed on RFX-mod.

If no sawtooth crash is detected for more than $2.1 \cdot T_{old}$, we assume that the sawteeth crashes disappeared.

The sawtooth detection approach described in this chapter is sufficiently reliable for RFX-mod. An example from shot 38351 with varying sawteeth period due to varying plasma density is shown in Fig. 9.2

9.3 RAPTOR validation

To obtain reliable results, the RAPTOR internal parameters listed in Tab. 9.1 have to be tuned to match the experimental data. For this purpose, the predictive RAPTOR mode was used. The experimental values of the plasma current and electron density are the only experimental inputs of the code. The electron and ion density profile width, the transport coefficients in (9.3) and the critical shear are tuned to fit experimental measurements of the core electron temperature, β_p, sawteeth period and possibly also the Thomson scattering temperature profile. The result of the validation for shot 38444 and for β_p, core electron temperature and the sawteeth period is depicted in Fig. 9.3.

The agreement of RAPTOR with experiment is very good in the flat-top phase of the discharge which is the most important for the experiments. The agreement is not that good in the initial phase of the discharge for β_p and sawteeth period. There are several possible explanations for this: as the current ramp-up is rather fast, plasma does not need to be in steady state equilibrium assumed by RAPTOR during the ramp-up. Other possibility is that the diamagnetic diagnostics does not work well in the initial phase of the discharge since it is affected by the eddy currents induced in the conductive structures during the plasma current and toroidal field ramp-up.

The value of the core electron temperature is very noisy at the beginning of the discharge due to low density, but the RAPTOR estimate seems to be roughly the same as the experimental one. In the flat-top phase, we can see the sawteeth both on RAPTOR and experimental waveform. The experimental sawteeth amplitude is larger than the RAPTOR one, but the sawteeth period, which is important for the RFX-mod experiments, is the same.

Last, let us demonstrate the ability of RAPTOR to estimate the sawteeth period when correct s_{crit} is provided. One can see a good agreement between RAPTOR and experiment in Fig. 9.3 in the flat-top phase of the discharge. On the other hand, there are no sawteeth crashes in RAPTOR at the beginning of the discharge despite the fact that they are present in the experiment. Likely reason is that the sawtooth crash detection algorithm identifies the peaks related to the 2/1 mode as the sawtooth.

Another independent check was made using Thomson scattering installed on RFX-mod. The estimate of the temperature profile by this diagnostic is shown in Fig. 9.4. This figure shows decent agreement between the RAPTOR and the Thomson scattering temperature profile for discharge 33734 after a sawtooth crash. The RAPTOR temperature profile is slightly broader than the one measured by Thomson scattering. However, the Thomson scattering on RFX is designed to measure

the profiles in RFP shots with much higher density. Lower electron density in tokamak discharges decreases the measurement precision. Due to this fact we consider that the Thomson scattering confirms that convenient RAPTOR parameters have been chosen.

Finally, let us show the predictive simulation parameters used to obtain these results. The values of tunable quantities are in Tab. 9.1. The simulation results in the observer mode can be considered

Parameter	Value
n_e width	0.8
n_i width	0.8
T_i/T_e	0.65
c_{ano}	4.0
$\chi_{central}$	0.35
s_{crit}	0.205

Table 9.1: The RAPTOR parameter settings used for RAPTOR predictive simulations validating the code results.

precise enough to use the same RAPTOR settings in real time for disruption prediction.

9.4 Real Time Disruption Prediction

In real experiments, RAPTOR operates in observer mode meaning that the experimental value of core electron temperature and β_p serve as code inputs used for correction of the information about the plasma state.

First of all, it was necessary to prepare a real time code that could be implemented into the real time MARTe framework [54]. Such a code needs to be translated into C++ language. Matlab provides a Real-Time Workshop tool performing the translation from Simulink to a C++ code that is insertable into MARTe. The Simulink model was prepared by Dr. Federico Felici and Dr. Chiara Piron. This model, transferred into C++ and implemented in MARTe, estimates the plasma state. The simulation time step and the number of spacial grid points are tunable (the same values will be used in real time), but as the typical sawteeth period is between 8 and 15 ms, the Simulink time step should not be much longer than 2 ms to predict the crashes correctly. The results of the Simulink model are expected to be identical with the results of the real time simulation. Thus, if we demonstrate the capability of RAPTOR to predict disruptions using the Simulink model, one can expect that the real time prediction will work as well.

For reliable sawteeth period estimate by the Simulink model (working in observer mode), the core temperature input signal has to be modified in such a way that the information about the sawteeth crashes is removed.

The reason is that RAPTOR in observer regime tends to keep the plasma state as close to the diagnostic measurements as possible. This code property causes the following problems: it is not possible to perfectly align the sawteeth crashes in RAPTOR and in experiment. Consequently, there will be huge discrepancy between the RAPTOR and the experimental value of temperature after/before the sawtooth crash. Thus, RAPTOR will modify the temperature estimate to fit the experiment in non-physical way. This deformation leads to corruption of the sawteeth period estimation. An example of such a behavior is shown in Fig. 9.5. One can see that the RAPTOR evolution of the core temperature is non-physical in case that the temperature input is not smoothed and contains information about sawteeth crashes. In reality, the core temperature grows until the sawtooth crash as in case of smooth input.

Another important point is the choice of the alarm parameter in 8.13. The best results in terms of early disruption prediction and fake alarm avoidance was achieved for $R_{ST} = 0.3$. This condition is sufficient in most studied cases, but if the RWM grows too fast, it does not need to be met as the sawteeth crashes disappear (or are not detectable anymore) before the threshold value of R_{ST} is reached. Therefore we introduced another standby condition: in case that RAPTOR predicts sawteeth activity and no sawtooth crash is detected for more than $2.1 \cdot T_{SXR}^{last}$, the alarm is activated as well.

Using the Simulink model alongside with the temperature input smoothing, we can demonstrate that RAPTOR is capable to predict the disruption caused by the RWM early enough to take some action to save the discharge or at least to mitigate the consequences. Let us show it on two examples from shot 33734 and 33735.

The result for 33735 is shown in Fig. 9.6. In this case, the disruption alarm was activated by one of the last sawtooth crashes with short period. The alarm was activated 40 ms before the disruption, providing sufficient time to avoid the disruption or at least to mitigate the consequences.

The disruption prediction for 33734 in Fig. 9.7 is marginal: as the 2/1 mode grows faster than in case of 33735, the last detected sawtooth crash does not activate the alarm which is finally started by the standby condition. On the other hand, the disruption is still predicted 15 ms before. This time could be useful for mitigation of the disruption consequences.

9.5 Real Time Performance Optimization

In the previous section, we have shown that the RWM disruption on RFX-mod can be predicted by sawteeth period monitoring using RAPTOR. As RAPTOR must run in real time, another part

of the work focused on the code settings optimization. On one hand, it is desired to reduce the cycle time as much as possible for better time resolution. On the other hand, the reliability of the prediction has to be preserved while decreasing the cycle time.

In the first version of RAPTOR implemented on RFX-mod, we used 6 spacial grid points and the original version of the sawtooth module with 1001 reconnection points. The execution time of this version is shown in Fig. 9.8. When the sawtooth module is not activated, the execution time is around 0.9 ms. The sawtooth module takes approximately 0.6 ms more. The first version suffered by several initial problems: first of all, the 1 D spacial grid consisting of 6 points appears to be insufficient for reliable disruption prediction. Secondly, the extra time required for execution of the sawtooth module is unacceptably high. The solution of these issues is presented in this section.

9.5.1 Number of Spacial Grid Points Optimization

The first step that had to be done was the determination of the minimal number of spacial grid points. If regularly distributed, RAPTOR needs at least 9 grid points for reliable sawteeth period estimate. To reduce this set, one can place the points closer to the flux surface with expected sawteeth reconnection, which is located between 0.3 and 0.5 on RFX-mod. This works for 8 and marginally also for 7 grid points. The optimal spacial point distribution for different numbers of spacial grid point is shown in Tab. 9.2.

In general, the usage of equally spaced points is preferred. The reason is that it is not granted that the reconnection appears at the position we expect. In this case, the code using irregular distribution of points may fail.

The dependence of execution time on the number of spacial grid points is quadratic, meaning that the "basic" execution time would increase from 0.9 ms to 2 ms when increasing the number of spacial points from 6 to 9. This is hardly acceptable due to the issues related to the time resolution of the sawteeth period estimation. Therefore some physics contained in the RAPTOR model needs to be omitted.

First of all, we neglected the bootstrap current. The bootstrap fraction on RFX-mod is according to RAPTOR simulations between 5 and 10 % of total current and minor modification of critical shear can easily compensate the effect of the loss of this information with small influence on the model results and numerical convergence, that can be compensated by a minor modification of the transport coefficients.

Secondly, we simplified the neoclassical transport coefficients computation. In standard RAPTOR, the neoclassical transport coefficients are upgraded in each code iteration depending on other

plasma parameters. Instead, we compute the coefficients just at the beginning of each cycle and consider the value constant for all following iterations. This simplification does not affect the code robustness.

The effect of these two simplifications on computational time was tested on a desktop Windows computer. The tests suggest that the cycle time will be reduced by 20 %. Unfortunately, this estimate is not very reliable due to suspicious behavior of the PC we used: the time of computation for the same RAPTOR configuration had large root mean square error. For more reliable estimate, a detailed analysis on different machine would be required. Assuming that the reduction by 20 % is correct, the RAPTOR execution time with 9 grid points would be 1.6 ms. To keep the execution time below 2 ms, the sawtooth module must be optimized as well.

Number Of grid points	Point Spacing
9	equally spaced
8	0.0 0.16 0.31 0.42 0.53 0.67 0.83 1.0
7	0.0 0.18 0.29 0.38 0.5 0.75 1.0

Table 9.2: The best distribution of spacial points for different numbers of the grid points.

9.5.2 Sawtooth Module Optimization

The only way to optimize the sawtooth module is the reduction of the number of reconnection points. The number of reconnection points affect the radial profile of the safety factor immediately after the reconnection. This quantity was studied for several cases with different number of points in reconnection model and the result is shown in Fig. 9.9. We considered that the case with 1001 points represents the correct q profile shape after the sawtooth reconnection. Reducing the number of points, we found that there is almost no difference between the correct profile and the profile computed using a reduced set consisting of 51 reconnection points. The situation for 21 points is slightly different, therefore we consider that we can reduce the number of reconnection points in the sawtooth module to 51 safely.

The main part of the time needed for the sawtooth module is consumed by the reconnection part. As we reduced the number of reconnection points by a factor of 20, we can expect reduction of the sawtooth module execution time by a similar factor. Therefore we expect the execution time to stay well below the required 0.4 ms.

By omitting some of the neoclassical effects and reducing the number of reconnection points in the sawtooth module, a robust and fast configuration of RAPTOR code on RFX-mod was obtained. Unfortunately, due to lack of experimental time, the capability of RAPTOR to predict

the disruptions by sawteeth period monitoring could not be demonstrated in real time. However, we demonstrated the feasibility of such a physics based disruption prediction. Other experiments dealing with this issue were performed in December 2015 on TCV and are expected to be completed in February/March 2016. The results of already performed experiments are reported in chapter X. The experience gained on RFX-mod have been certainly useful.

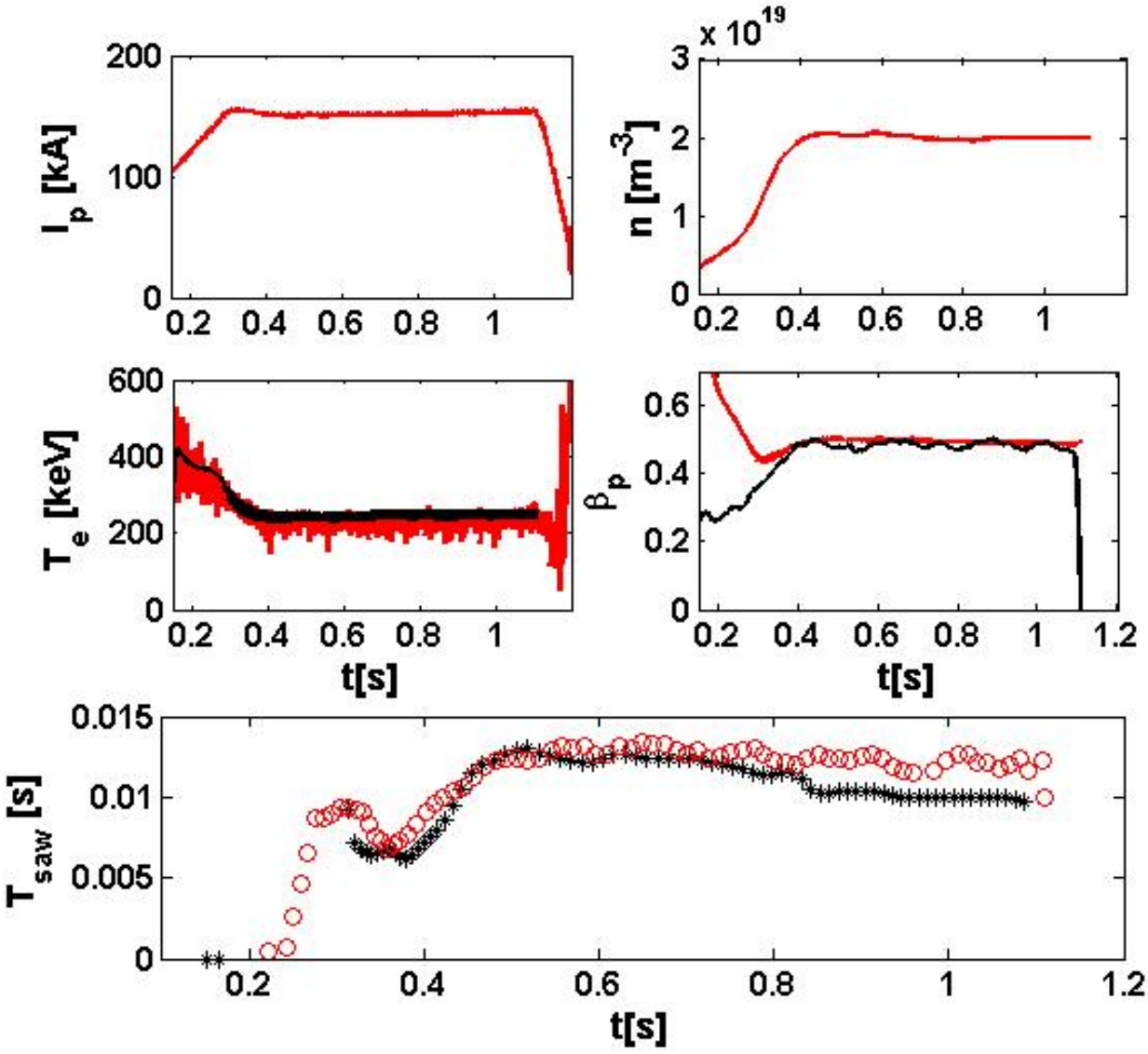

Figure 9.3: The time evolution of various plasma properties for shot 38444. The red color always denotes the experimental value, the black one the value computed by RAPTOR predictive simulation. The plasma current and electron density are the only RAPTOR inputs.

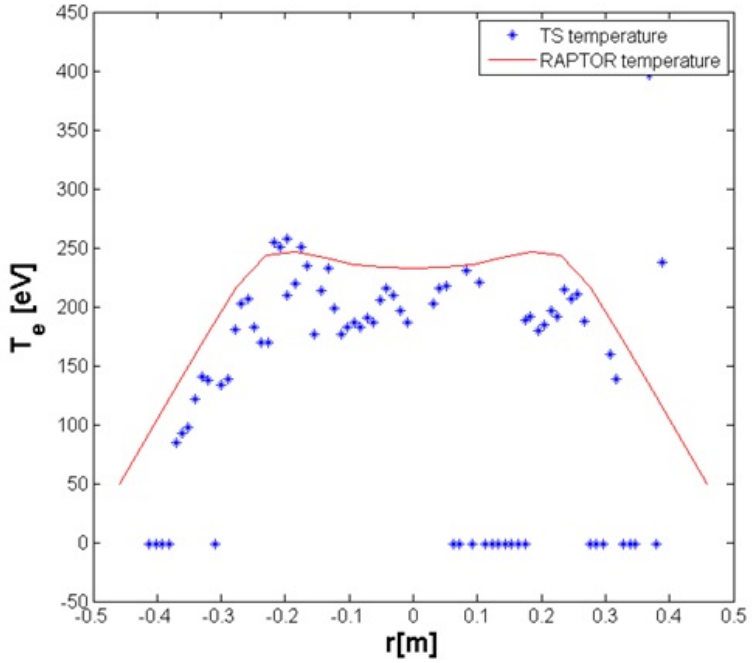

Figure 9.4: The comparison of electron temperature profile in RAPTOR and Thomson scattering for shot 33734 immediately after a sawtooth crash.

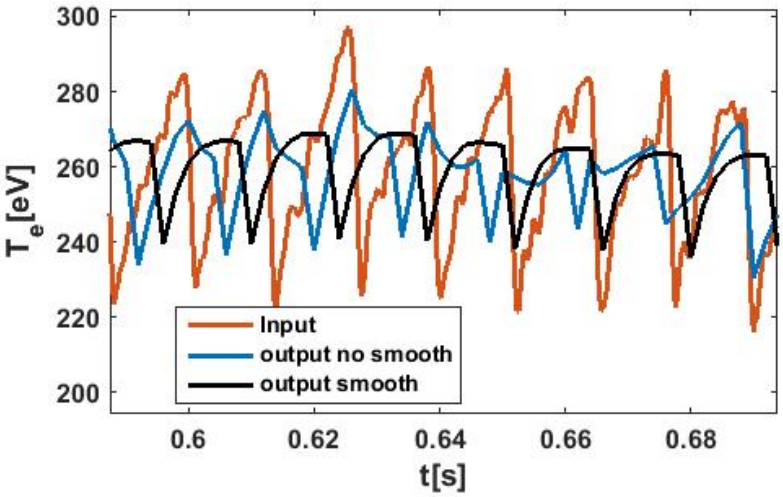

Figure 9.5: The time evolution of experimental T_e (orange), the RAPTOR T_e in case that the input T_e of RAPTOR is represented by the orange curve (blue) and the output RAPTOR T_e in case that the input is smoothed and does not contain any information about sawteeth crashes (black). Note that the evolution of the T_e represented by the blue curve is non-physical.

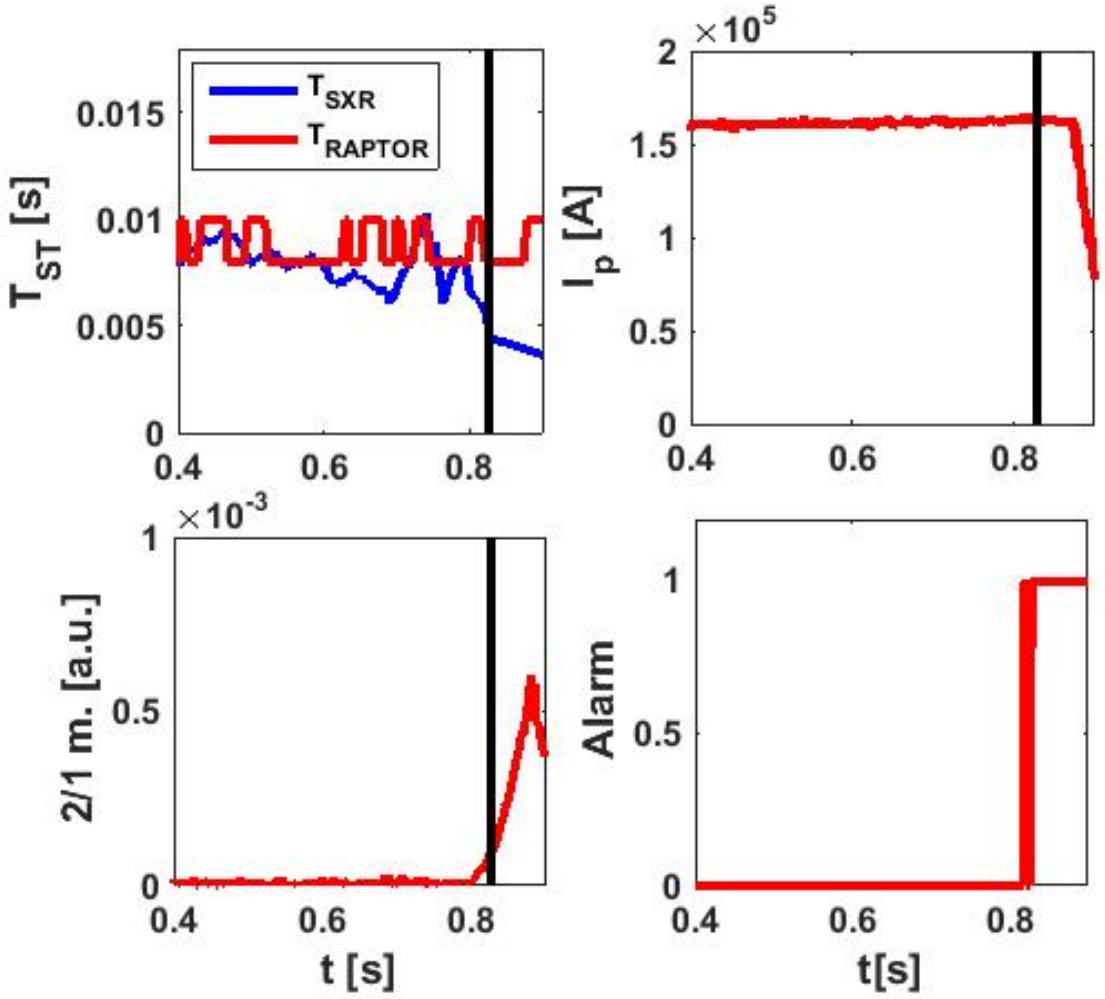

Figure 9.6: The time evolution of experimental sawteeth period (T_{SXR}), sawteeth period estimated by RAPTOR (T_{RAPTOR}), plasma current, 2/1 mode amplitude and the disruption alarm for shot 33735. For the alarm, value 0 means that the alarm is inactive and value 1 means that it is active. The black vertical line indicates the time when the alarm is activated.

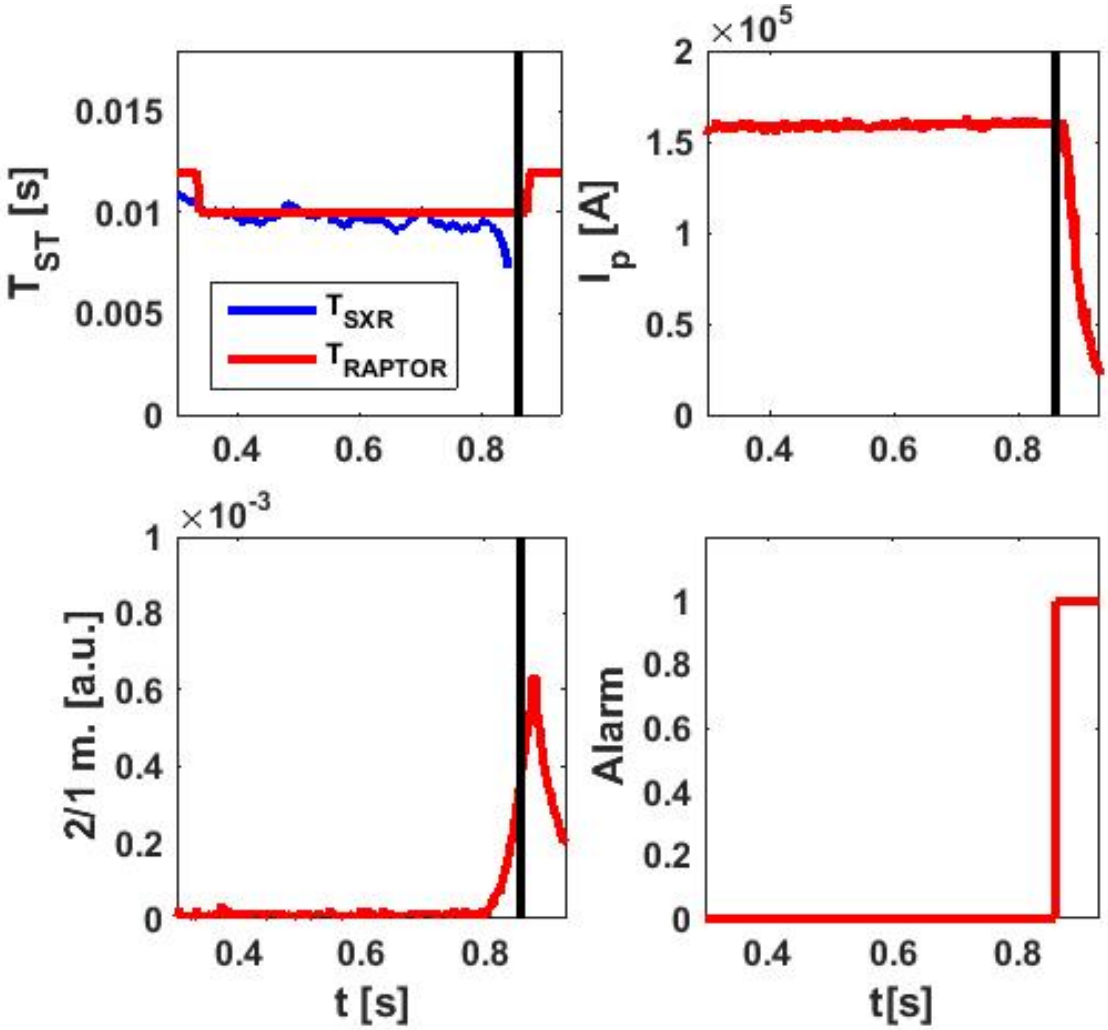

Figure 9.7: The time evolution of experimental sawteeth period (T_{SXR}), sawteeth period estimated by RAPTOR (T_{RAPTOR}), plasma current, 2/1 mode amplitude and the disruption alarm for shot 33734. For the alarm, value 0 means that the alarm is inactive and value one means that it is active. The black vertical line indicates the time when the alarm is activated.

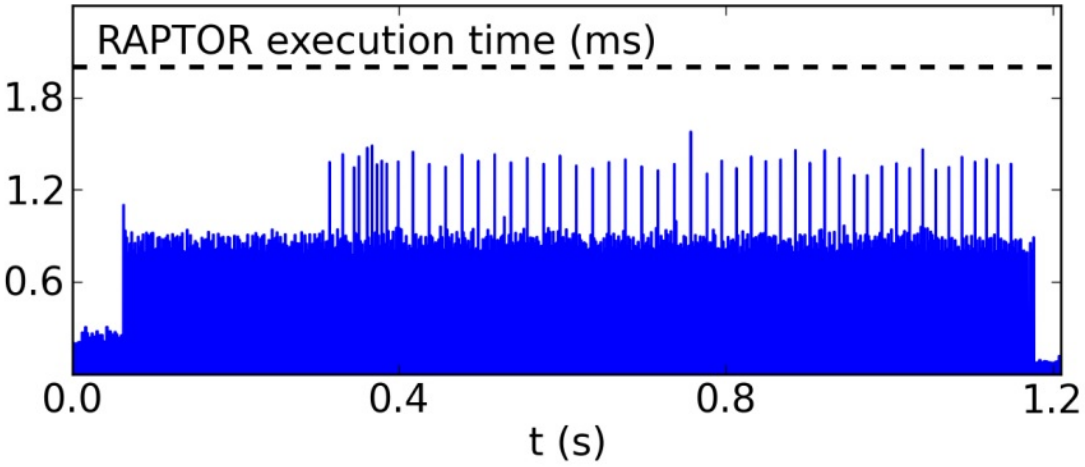

Figure 9.8: The execution time of RAPTOR in MARTe. This version uses 6 spacial grid points and the sawtooth module with 1001 reconnection surfaces. A peak in the execution time can be seen whenever the sawtooth module is activated. The black horizontal dashed line shows the cycle time (the highest possible execution time). Figure taken from [109].

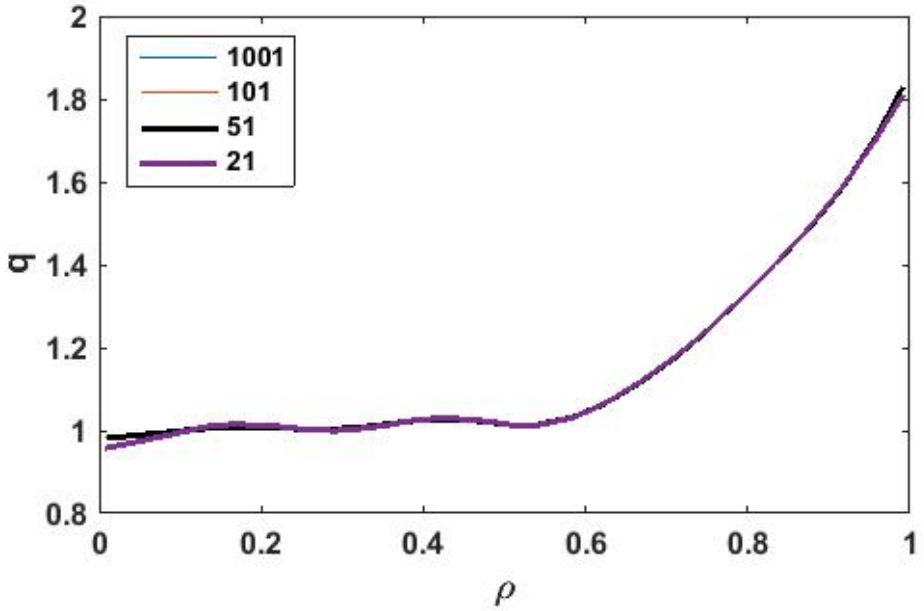

Figure 9.9: The radial profile of the safety factor immediately after the sawtooth crash for different numbers of the reconnection points. One can see that the profile for 1001, 101 and 51 overlap, but the case with 21 points is slightly different.

CHAPTER X

Density Limit Disruption Prediction on TCV

On RFX-mod, we have shown that RAPTOR is capable of RWM disruption prediction based on sawteeth period monitoring. However, there are also other classes of disruptions where the sawteeth period monitoring based prediction could be applied. Section 8.3.3 suggests that density limit disruptions should be predictable as well. To test this method, several dedicated TCV shots were made in December 2015. Since RAPTOR was not available in real time yet, the activity was focused the proof of the principle and selection of proper discharges for real time future demonstration. For all demonstrations below, we use the cycle time of real time RAPTOR on TCV equal to 1 ms.

10.1 Disruption prediction in density limit discharges on TCV

This section proves the principle of disruption prediction based on sawteeth period monitoring on TCV. For that purpose, three dedicated shots were done. The waveforms of line averaged density and plasma current are shown in Fig. 10.1. The time evolution of the electron temperature at $\rho = 0.15$ simulated by RAPTOR and measured by Thomson scattering is shown in Fig. 10.2 for all three discharges. It shows a good agreement between RAPTOR and experiment in terms of this quantity. We have used the temperature at $\rho = 0.15$ for comparison, since no direct measurement is available closer to the magnetic axis and the on-axis temperature is estimated by extrapolation, which is not very precise.

In the first discharge, 50939, the density was ramped until disruption. After the discharge, we checked the sawteeth behavior (shown in Fig. 10.3) and found the density value where the sawteeth period started deviating from RAPTOR prediction- if RAPTOR had been running in real time, this deviation would have activated a disruption alarm. In the next discharge, 50956, we stopped the density ramp at this value. After that we kept the density constant. Sawteeth behavior is shown

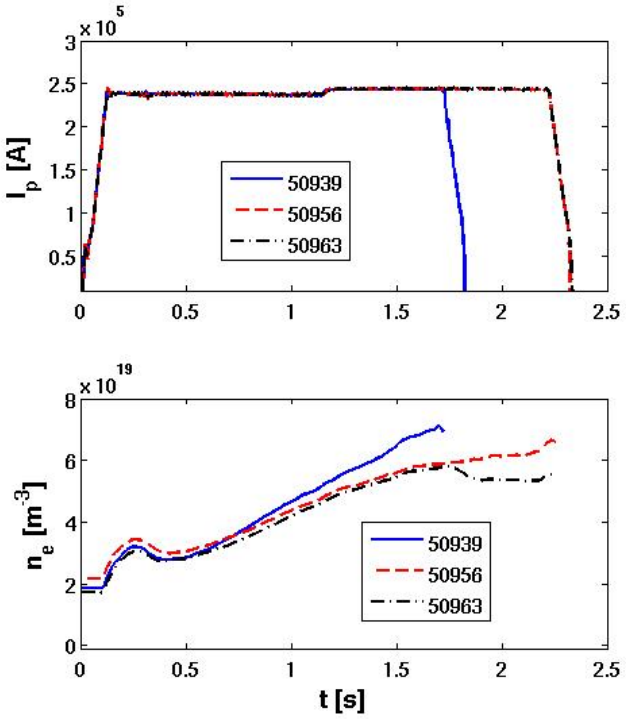

Figure 10.1: The waveforms of plasma current and line averaged density in discharges 50939, 50956 and 50963 performed for demonstration of disruption prediction based on sawteeth period monitoring on TCV.

in Fig. 10.3. No disruption was observed, but disruption alarm would be active until the end of the discharge. In the last discharge, we reached the density to activate the disruption alarm, but afterwards we decreased it by 10 %. In Fig. 10.3 one can see that normal sawteeth behavior was recovered after the density decrease.

10.1.1 Alarm condition

Before we show the results of disruption prediction using RAPTOR in the above mentioned discharges, let us introduce the condition to activate the alarm.

We used the same sawtooth detection algorithm as in RFX-mod (see section 9.2). As the sawteeth behavior in density limit cases is more irregular than in case of RWM disruptions, the alarm activation method needs to deal with occasional failures of the sawtooth detection algorithm that are unavoidable at present stage. Such an event should not activate fake alarm. The way to deal with that is to use information from the past difference between sawteeth period in RAPTOR and in experiment. In the other words, we will use integral of the past difference instead of present value of the sawteeth period difference as in (8.13).

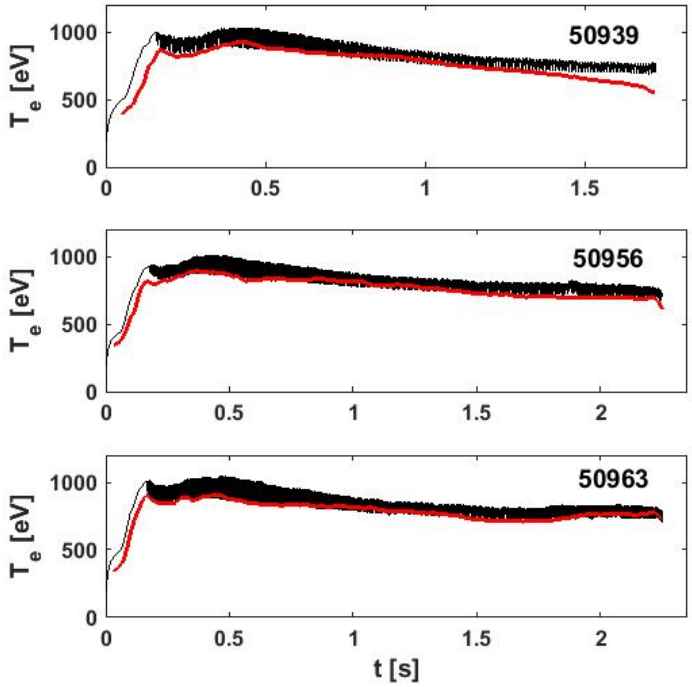

Figure 10.2: The time evolution of electron temperature at $\rho = 0.15$ in TCV discharges 50939, 50956, and 50963 measured by Thomson scattering (red) and estimated by RAPTOR (black).

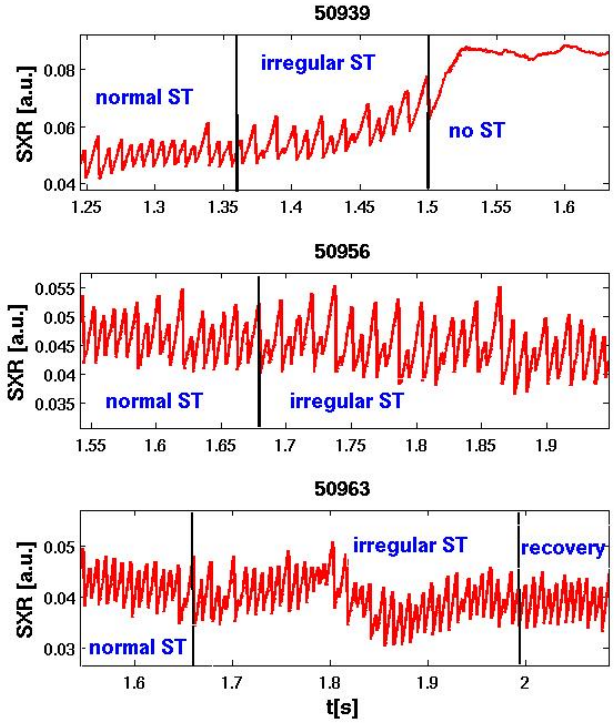

Figure 10.3: The sawteeth behavior in TCV discharges 50939, 50956, and 50963 in time intervals significant for disruption prediction.

Computing the difference from long time window increases the reliability of the disruption prediction (decreases risk of fake alarm), but increases the reaction time (increases risk of missed alarm). The length of the time window must be selected properly to reach the best possible compromise between these two requirements. We have decided to take information from the time window covering last 80 ms (8-15 sawteeth crashes). Let us define deviation D_{ST} of the experimental sawteeth period from the RAPTOR prediction as

$$D_{ST} = \frac{1}{N}\sum_{i=1}^{N} \frac{1}{log(10+N-i)} \frac{(T_{SXR}(i) - T_{RAPTOR}(i))^2}{\left(\frac{T_{SXR}(i)+T_{RAPTOR}(i)}{2}\right)^2}, \tag{10.1}$$

where N is number of samples (in our case equal to 80, but it is a tunable parameter) and i is the index of the sample; $i = 1$ corresponds to the oldest sample, $i = N$ to the newest sample. The inverse logarithmic term in the sum is introduced to increase the significance of newer data.

The disruption alarm is activated if

$$D_{ST} > 0.03 \tag{10.2}$$

and deactivated if

$$D_{ST} < 0.02. \tag{10.3}$$

The reason we use different levels for activation and deactivation is that the value of D_{ST} can be temporarily increased/decreased due to failures in the sawtooth detection algorithm.

10.1.2 Disruption prediction using RAPTOR

After defining the alarm condition, let us demonstrate the behavior of the plasma state predicted by RAPTOR in the above mentioned TCV discharges. First of all, let us show discharge 50939 ended by disruption. The time evolution of the sawteeth period, deviation D_{ST}, and alarm (active <=> 1, inactive <=> 0) are shown in Fig. 10.4. The disruption alarm would be activated at density equal to $6.1 \cdot 10^{19}$ m^{-3} and 200 ms before the disruption that appears at density $7 \cdot 10^{19}$ m^{-3}. The time is sufficient to react, for example decreasing the plasma density by closing the gas puffing valves or terminating the discharge in controlled way. One can see a fake alarm at the beginning of the discharge. The cause and possible solutions will be discussed in the following section.

In the next discharge, 50956 (shown in Fig. 10.5), one can see that the alarm becomes active after the density exceeds the value $5.9 \cdot 10^{19}$ m^{-3} at time 1.72 s, but the disruption does not appear: this means that there is a margin between the density where the alarm is activated and the density that

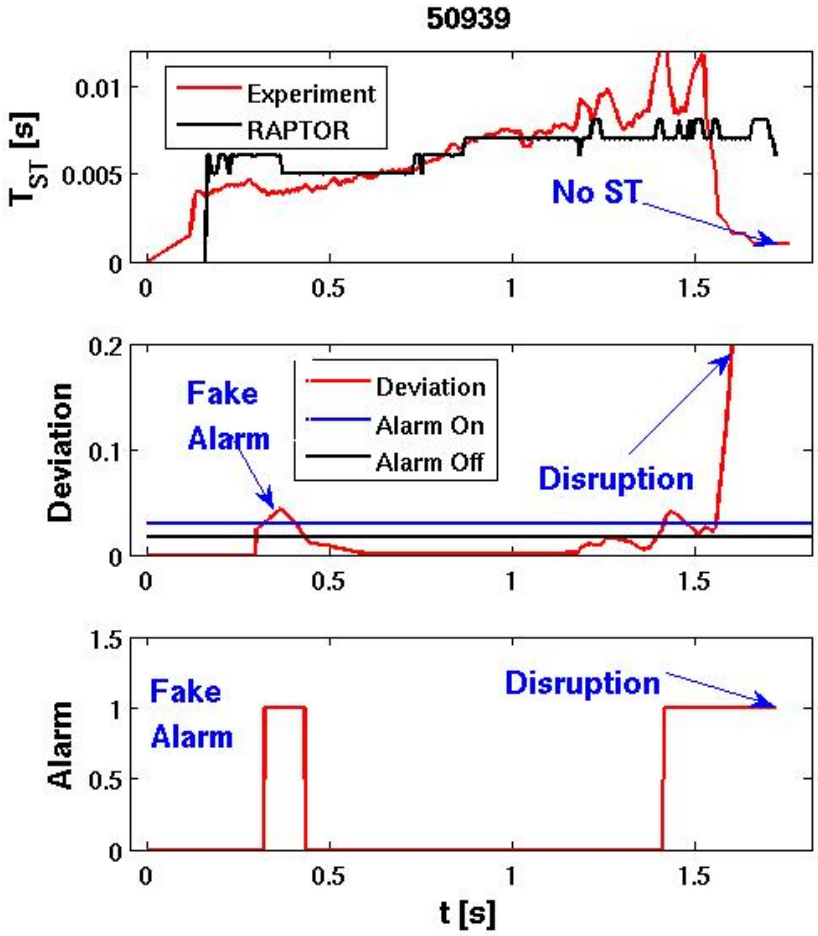

Figure 10.4: The time evolution of the sawteeth period in experiment and estimated by RAPTOR, the value of deviation D_{ST} and the disruption alarm for TCV discharge 50939. For alarm, the value 0 means inactive alarm, value 1 means active alarm.

leads to disruption: concluding from shot 50939, 50956, and 50963, the density causing disruption is approximately 15 % higher than the density activating the alarm. However, this estimate is just approximate and will have to be verified on a larger set of discharges.

In the last discharge, 50963, shown in Fig. 10.6, one sees that the alarm was activated after the density reached the value $5.8 \cdot 10^{19}\ m^{-3}$. However, later the alarm was switched off due to the density decrease to $5.4 \cdot 10^{19}\ m^{-3}$. As in case of 50939, there was a fake alarm at the beginning of the discharge.

All simulations were made with constant transport parameters and critical shear given in Tab. 10.1. The parameters were tuned on other discharges from the density limit experiments. Having constant parameters is one of the key conditions that must be met by successful method for disruption prediction.

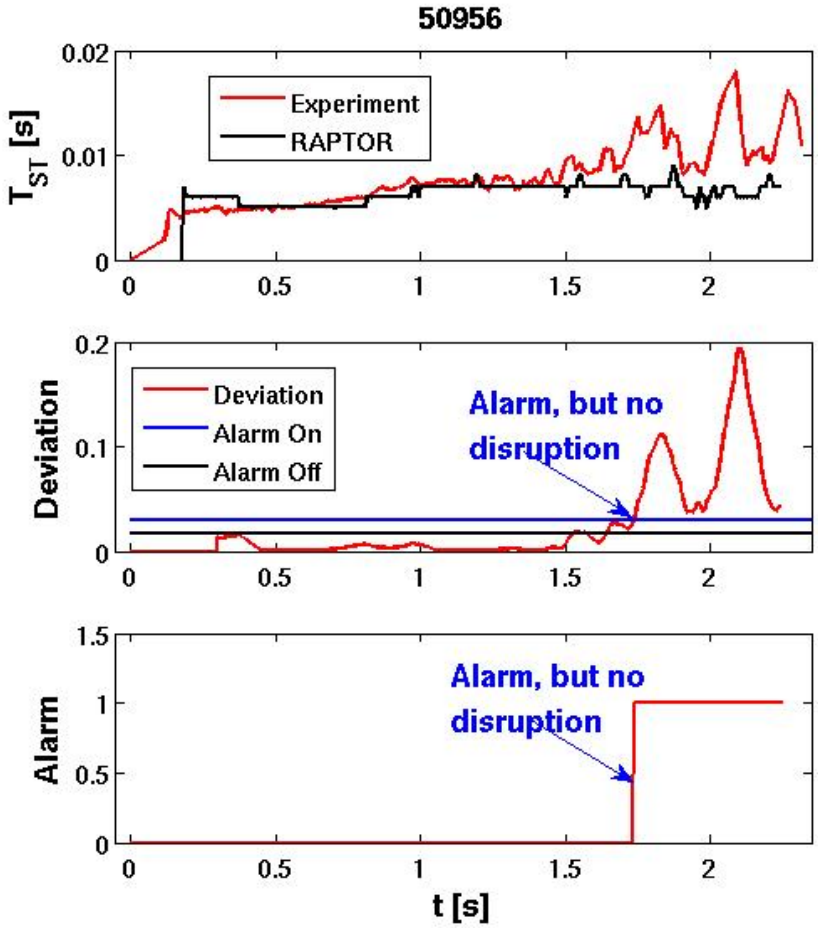

Figure 10.5: The time evolution of the sawteeth period in experiment and estimated by RAPTOR, the value of deviation D_{ST} and the disruption alarm for TCV discharge 50956. For alarm, the value 0 means inactive alarm, value 1 means active alarm.

The above mentioned discharges showed that disruption prediction by sawteeth period monitoring is feasible in TCV ohmic L-mode discharges. A dedicated campaign with RAPTOR running in real time is scheduled for February/March 2016. For this purpose, the sawtooth detector and the code activating the alarm will have to be transferred into the real time framework.

c_{ano}	1.7
$\chi_{central}$	0.0
s_{crit}	0.23

Table 10.1: The transport coefficients and critical shear used for all TCV simulations shown in this chapter.

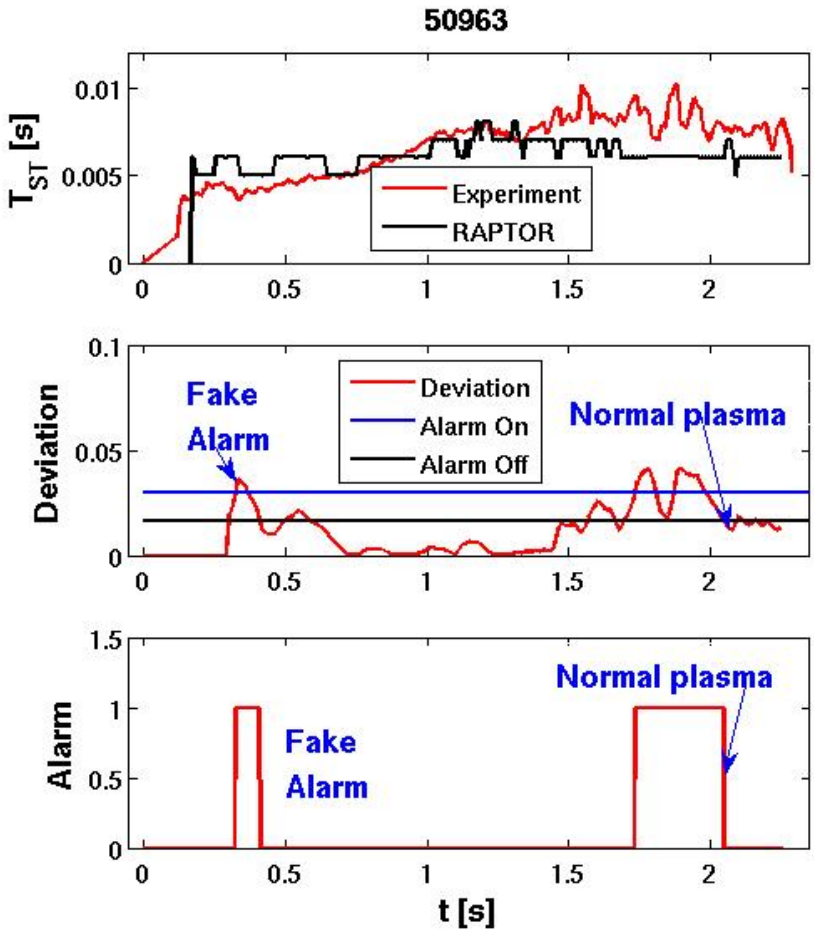

Figure 10.6: The time evolution of the sawteeth period in experiment and estimated by RAPTOR, the value of deviation D_{ST} and the disruption alarm for TCV discharge 50963. For alarm, the value 0 means inactive alarm, value 1 means active alarm.

10.1.3 Fake Alarms at the Beginning of the Discharge

Last, let us describe the reason and possible solutions of the fake alarms observed at the beginning of the discharge 50939 and 50963. The reason of discrepancy in the sawteeth period is too long time step of RAPTOR simulation, that does not allow capturing the fast effects at the beginning of the discharge (fast density and current ramp). The differences in sawteeth period between simulations with 1 ms and 0.1 ms timestep are depicted in Fig. 10.7. One can see that the simulation with 0.1 ms time step tracks the experimental results at the beginning of the discharge better than the simulation with 1 ms timestep. Later, the agreement of 1 ms and 0.1 ms simulation with experiment is comparable in terms of trends in the observed sawteeth period. In reality, if the 0.1 ms time step were used, one would have to adjust the alarm condition in section 10.1.1.

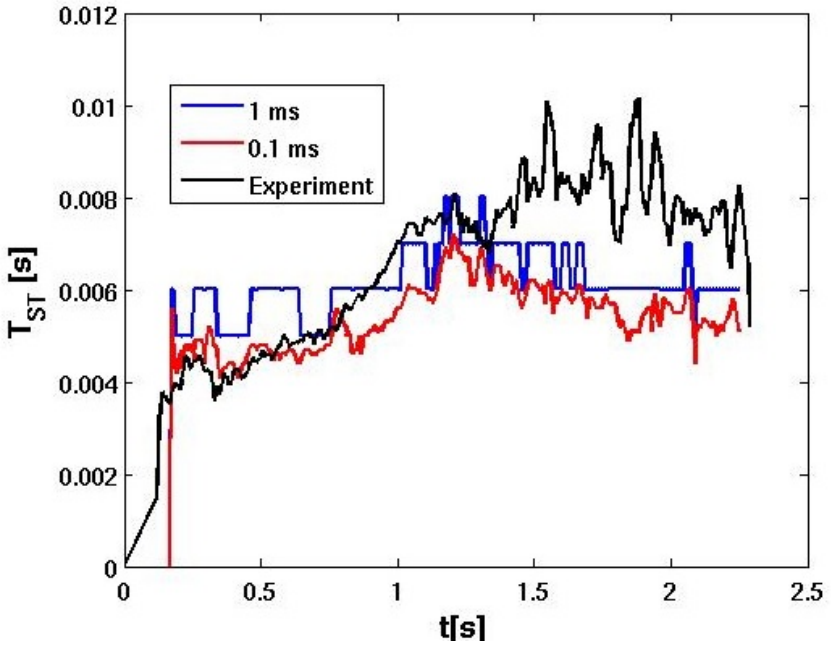

Figure 10.7: The difference in sawteeth period between the simulation with 0.1 and 1 ms RAPTOR time step and their comparison to experimentally observed sawteeth period for TCV discharge 50963.

However, it is not feasible to run RAPTOR simulation with time step lower than 1 ms on TCV at this stage. Hence one needs to find another way to deal with this problem. For the moment, we suggest enabling disruption alarm activation 300 ms after the discharge gets to the flat-top phase, which corresponds to current redistribution characteristic time for TCV ohmic plasma. It is unlikely that the plasma meets the physical limits in such a short time, but it eliminates the fake alarms at the beginning of the shot.

10.2 Alarm Condition Implementation in Simulink

In the view of the experiments, the system activating the alarm was implemented in Simulink. Afterwards, this Simulink module will be inserted into the complete RAPTOR Simulink model. The model scheme is shown in Fig. 10.8. The inputs of the model are the sawteeth period in experiment and the sawteeth period estimated by RAPTOR.

The first Simulink block computes the most recent term of sum (10.1), the second block combined with the delay block updates the value of all sawteeth related terms in sum (10.1), keeps the old values in a vector of N elements and computes the deviation D_{ST} by multiplying the sawteeth period related vector by the weight factor in (10.1). Later, the alarm is activated or deactivated based on the value of D_{ST} and on actual value in Alarm variable. If the method is proven to work with

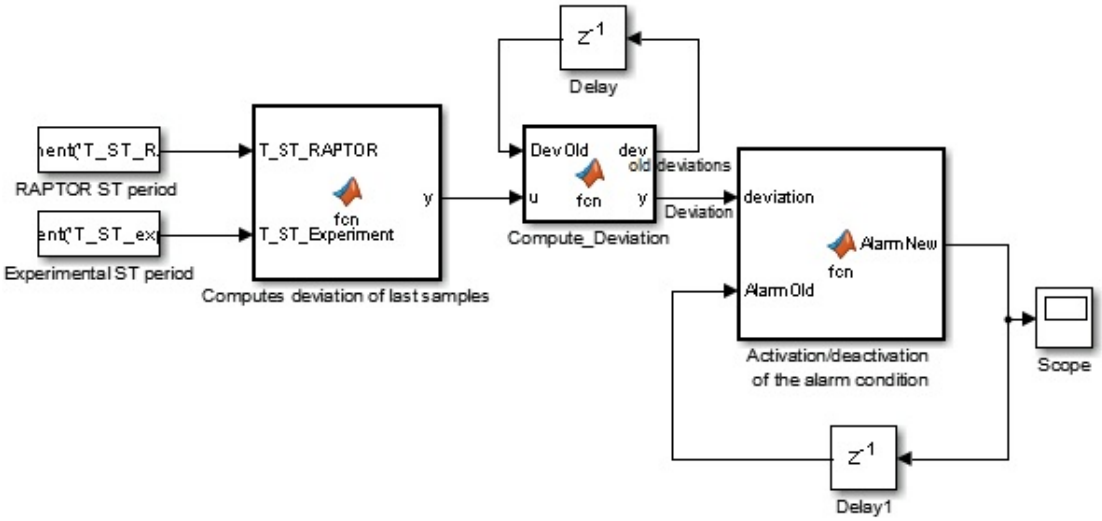

Figure 10.8: The Simulink scheme of the disruption alarm that will be inserted into the real time control scheme.

sufficient reliability in real time, the alarm will be passed to the control system that will take proper actions to avoid the density limit disruption.

CHAPTER XI

Outlook: Disruption Prediction on ASDEX-Upgrade

The last part of the activity focused on disruption avoidance by RAPTOR was performed on ASDEX-Upgrade (see part 2.5.4 for the basic machine description). Clearly, ASDEX-Upgrade is much more complex device compared to RFX-mod or TCV and the RAPTOR activity on disruption avoidance is intended to show the direction of future activities and determine the level of the RAPTOR code complexity.

As first examples, two density limit disruption discharges, one with a 3/2 mode at the beginning of the discharge were studied.

In both studied cases, RAPTOR was run in predictive mode (it is also available in observer regime, as reported in [114]). The inputs were the electron density profile, EC and NBI power, and the plasma current. For transport, we used BgB model introduced in section 8.2. The comparison between RAPTOR and the experiment was done on sawteeth period and on electron temperature around $\rho = 0.2$. The reason we did not compare the core temperature are the problems with magnetic axis ($\rho = 0$ flux surface) geometric location on AUG by standard equilibrium reconstruction tools, that do not provide good estimate of flux surface geometry close to the magnetic axis.

11.1 Studied discharges

11.1.1 Density limit disruption: 30615

The first studied case is focused on disruption caused by density limit. In this case, the discharge was in H-mode and NBI heating with power of 2.5 MW from 0.7-1.3 s and 5 MW for the rest of the discharge.

The time evolution of relevant quantities is shown in Fig. 11.1. The agreement between RAPTOR and experiment is decent in terms of temperature until the several hundreds of ms before the disruption (the only short exception is the time window between 0.7 and 1 s).

The agreement in terms of sawteeth period is very good until the density reaches certain limit where the transport properties change. This is foreseen by the theory described in section 8.3.3. In addition, the crashes in RAPTOR and experiment start almost at the same time. However, the time of the first sawtooth crash is very sensitive to two parameters. First of all, the right temperature on the top of the pedestal must be provided. The measurement of this value is not trivial. Second, the tearing modes at the beginning of the discharge can slow down the current penetration to the plasma centre, therefore keeping $q(\rho = 0) > 1$ for longer time than in case where no mode is present. The sawteeth properties can be also significantly modified by the presence of fast particles.

In this discharge, the disruption could be predicted based on both sawteeth period. Alternatively, the disruption prediction could be based on monitoring of temperature close to the magnetic axis and alarm activation if the difference between RAPTOR prediction and real temperature becomes too high.

11.1.2 Density limit disruption 2: 32424

The second studied discharge on AUG was shot 32424 ended by density limit disruption: NBI heated H-mode plasma. The NBI heating power was 2.5 MW between 0.5 and 0.9 s, 5 MW between 0.9 and 1.4 s and 7.5 MW from 1.4 s until the end of the discharge.

In this case, the agreement between electron temperature in RAPTOR and experiment shown in Fig. 11.2 is decent until a certain density level is reached. However, one can see huge discrepancy between the time of the first sawtooth crash appearance in RAPTOR and experiment. This could be caused by several effects. The first of them is the presence of a 3/2 mode in the beginning of the discharge between 1.1 and 1.6 s. The presence of the mode was included in the RAPTOR simulation to fit the temperature profile. However, the agreement between the time of the first sawtooth crash was not obtained. The reason might be that the 3/2 mode, besides the temperature profile modification, slows down the current penetration to the plasma core (this effect is not taken into account in RAPTOR) by pumping the poloidal flux outside the core. The principle of this effect is discussed in [115], [116] for a hybrid tokamak regime generation, that can be supported by 3/2 mode. General explanation of similar effects for RFP is reported in [117]. Several hundreds of milliseconds after the 3/2 mode disappears (t = 1.6 s), the sawteeth behaves as expected: the sawteeth crashes disappear before disruption while RAPTOR predicts unaffected crashes.

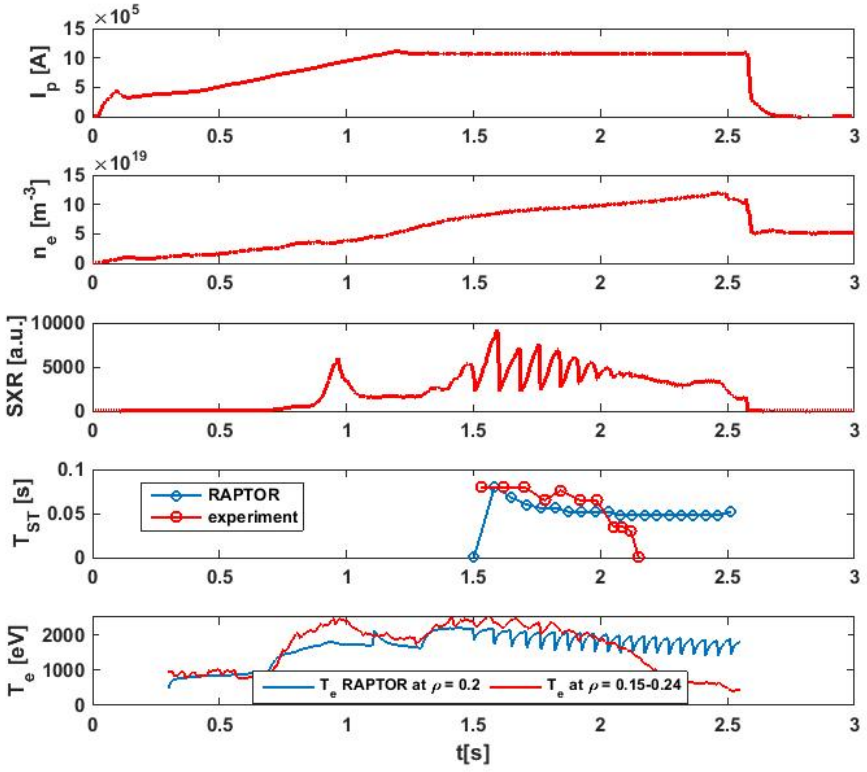

Figure 11.1: The time evolution of plasma current, plasma density, SXR signal, sawteeth period in RAPTOR and experiment and the temperature estimated by RAPTOR and ECE diagnostics for discharge 30615.

However, there are several other options that could explain the discrepancy, for example significant fast ion population. In the following analysis, we will focus on identification of the reason and possible solutions within RAPTOR.

In this discharge, disruption is predictable by both temperature and sawteeth crashes. However, the prediction by sawteeth crashes would activate a fake alarm at the beginning of the discharge.

In this section, we have shown two AUG discharges where disruptions can be predicted by either sawteeth period or close axis temperature monitoring. However, it must be mentioned that the transport coefficients had to be tuned to make the simulation fit the experiment: the transport coefficient values are in Tab. 11.1.2.

discharge	c_b	c_{gb}	s crit
30615	2.5	0.5	0.26
32424	2.5	0.7	0.23

Table 11.1: The transport coefficients and critical shear used in the ASDEX-upgrade simulations mentioned in this chapter.

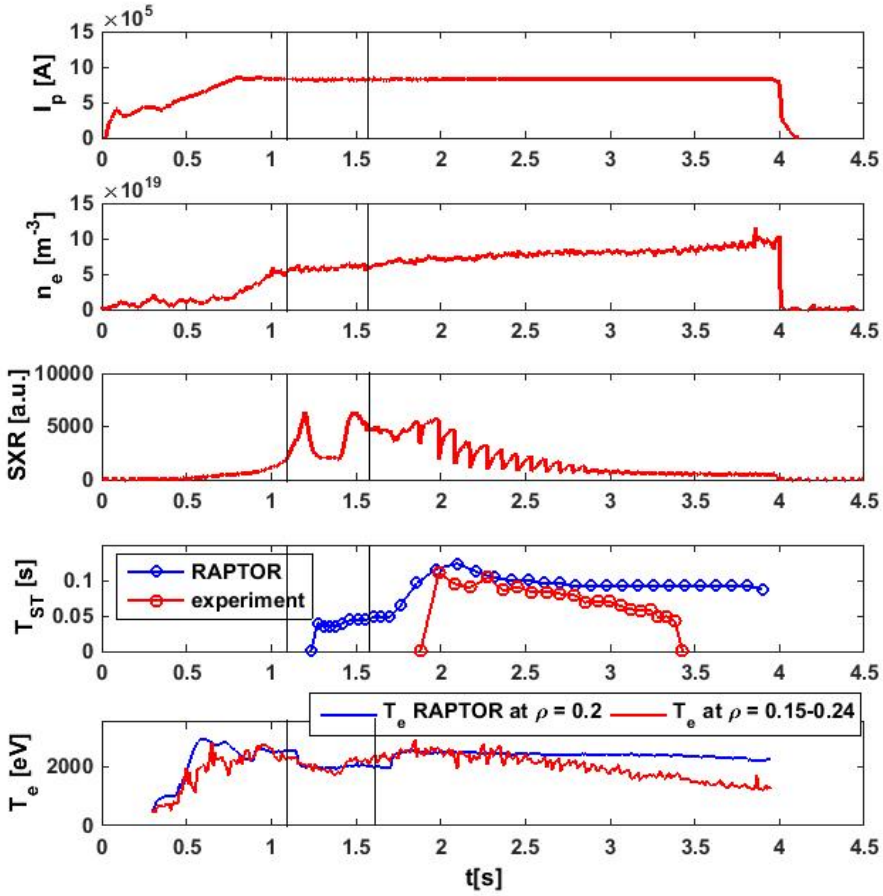

Figure 11.2: The time evolution of plasma current, plasma density, SXR signal, sawteeth period in RAPTOR and experiment and the temperature estimated by RAPTOR and ECE diagnostics for discharge 32424. The vertical black lines indicate the time when the 3/2 mode was present.

11.2 Future of disruption prediction by RAPTOR

As mentioned in previous section, the simulation parameters must be tuned from shot to shot. Obviously, this feature is not acceptable for future disruption avoidance algorithm. However, a new disruption avoidance schemes must be developed, since the present day strategies do not provide satisfactory results for future devices as described in section 8.3.1.

Certainly, strategies based on RAPTOR simulations represent an interesting alternative to the standard approaches. However, the present RAPTOR version does not represent viable option yet. There are several physical effects that need to be included into RAPTOR model.

First of all, it will be necessary to include complete coupling of RAPTOR with a real time equilibrium solver to deal with situations where plasma shape changes. At the moment, the coupling works just in one direction: the real time Grad-Shafranov solver passes equilibrium information to

RAPTOR, but does not use RAPTOR profiles as constraints yet. It will be also necessary to include IC heating and current drive. Next point to be resolved is the real time estimation of the current driven by EC, IC, and NBI systems. For the EC waves, the estimation can be done for example by comparing RAPTOR with the TORBEAM code [118], for IC waves one can use TORIC [119], and for NBI NUBEAM [120] code. To some extent, this has been done, but it presently requires re-tuning for each discharge if one changes e.g. the EC injection angle.

Another important issue is related to the population of fast ions in plasma. The fast ions can significantly contribute to the plasma energy and influence MHD stability of the plasma, for example stabilize sawteeth crashes. The most important source in present day devices is the NBI and IC heating, possibly also their coupling. In ITER, the α particles produced by fusion reaction will become dominant component in the fast ion population. To keep RAPTOR relevant to the experiment, a model of fast particles production will have to be included. Eventually, the RAPTOR estimate can be corrected by collective Thomson scattering measurement of fast particle population (basic description of the method together with useful references is given for example in [121]).

The RAPTOR state estimate can be significantly improved by using more advanced transport models. One possibility, reported in [122], suggests to use a transport model derived by nonlinear regression. The regression model is build using a database of a gyrokinetic transport code outputs.

However, one needs to keep in mind that RAPTOR is a real time lightweighted code, therefore the plasma state in more complex discharges can not be reliably estimated just by solving the simple transport equations described in section 8.2. Significant improvement could be achieved by more precise electron temperature estimate from plasma diagnostics, especially close to the magnetic axis, where either no data are available by now or the measurement of $T_e(\rho)$ is inaccurate due to imprecise real time equilibrium reconstruction precision close to the magnetic axis (however, this can be improved in post-shot analysis using more advanced codes such as IDA [123]). The later can be also improved by coupling of Grad-Shafranov solver with RAPTOR. If the temperature profile was known, the transport coefficients tuning would be less important and the information about current and pressure profiles would be more reliable.

After incorporating the above mentioned improvements, we believe that RAPTOR will be a valid tool for disruption avoidance in any device with a high degree of complexity.

CHAPTER XII

Conclusions

This thesis contains methods of real time measurement used in tokamak devices for plasma control from the oldest and simplest ones to the most modern ones: from the plasma current centroid position control to the internal profiles control. The thesis provides a novel and original contribution to methods in each category.

The first part deals with the problem of plasma current centroid position measurement on IST-TOK using magnetic diagnostics. This measurement is problematic from two reasons: the signals on magnetic pick-up coils are strongly affected by the eddy currents induced in the passive structures, therefore it is difficult to separate the signal generated by the plasma current and estimate the current centroid position. Second problem is caused by flawed magnetic sensors calibration. The first problem was resolved using a state space model fitted from the vacuum discharge, that is capable to subtract the eddy current signal in real time. For the second one, a simple provisional algorithm that is not very sensitive to calibration errors was found. The plasma centroid position behaves as expected in case of externally applied perturbation and the trends measured by Heavy Ion Beam show the same results as the suggested simple algorithm. Therefore I believe that the proposed algorithm is a viable solution for ISTTOK plasma centroid position measurement with present diagnostics. However, after a planned upgrade of magnetic diagnostics, one can use much more advanced methods. One of them was suggested at the end of the chapter. This activity will likely lead to the design of a plasma current centroid position controller that will improve the properties of the ISTTOK plasma and possibly extend the possibilities of physical analysis of ISTTOK discharges.

One of the most important achievements of the work presented in this thesis is the development of an original real time applicable plasma boundary reconstruction algorithm suited for application on RFX-mod. Such an algorithm was proposed, validated against Grad-Shafranov solver MAXFEA and

experimentally tested in RFX-mod discharges. The highlight of this algorithm is that it works with very low error (below 2 %) for a limited number of sensors (8 pick-up coils and 8 flux-loops in RFX-mod). Design and the real time implementation of the algorithm and its use to generate feedback signal for the shape control system allowed extending the space of the RFX-mod operation, especially in diverted regimes. The knowledge of the plasma boundary and magnetic field everywhere in the vacuum provided by the plasma boundary reconstruction method combined with the diamagnetic measurement can be also used to calculate plasma macroscopic parameters important for tokamak operation such as β_p, internal inductance l_i, edge safety factor q_{95}, total energy content and many other quantities derived from these parameters. Well controlled and diagnosed diverted discharge also facilitated LH transition experiments in RFX-mod. H-mode in ohmic regime was not achieved, but the consequent experiments with biasing electrode led to LH transition as confirmed by the drop of H_α signal, increase of core density and soft X-ray signal and pedestal formation at the edge of the plasma. The algorithm is also expected to be used after the planned upgrade of the RFX-mod in order to support future tokamak experiments.

The control and measurement of the plasma boundary is still insufficient for future devices, that will also require feedback control of the internal profiles (current, temperature, density, impurity etc...) and complete disruption avoidance. The existing profile control algorithms appear to be insufficient, since the above mentioned tasks will have to be reached in harsh neutron radiation environment with limited set of diagnostics. Additionally, some quantities that can not be measured will become important, for example the bootstrap current fraction. Therefore a code that complements the information from real time diagnostics is needed. A possible candidate is RAPTOR (RApid Plasma Transport simulatOR) code and the final part of the thesis is dedicated to activity related to disruption prediction by this tool. RAPTOR implementation on RFX-mod and experiments on Resistive Wall Mode disruption prediction by real time sawteeth period monitoring are reported in the thesis. We show that RAPTOR is capable of predicting the RWM disruption several tens of ms before it appears. Similar experiments for density limit disruptions were started on TCV in December 2015 and are expected to be completed in early 2016. The disruption can be predicted hundreds of milliseconds before. The results from RFX-mod and TCV suggest that the disruptions can be predicted by sawteeth period monitoring using RAPTOR in ohmic discharges. The rate of missed alarms and fake alarms is to be analyzed.

Clearly, predicting some classes of disruptions in L-mode ohmic plasma is a nice demonstration of RAPTOR capabilities, however it can not be taken as a valid tool for disruption prediction in more complex devices in the present stage of its development. The last part of the thesis tests

the same method as the one used on RFX-mod and TCV for disruption prediction on ASDEX-Upgrade for density limit cases. It shows that disruption avoidance by RAPTOR is feasible, but significant code development is still needed. First of all, it will be necessary to include all heating and current drive sources and include computation of the current drive efficiency for each source. Second important part, that is presently being developed, is the coupling of a real time Grad-Shafranov solver with RAPTOR. This will improve the precision of RAPTOR prediction in discharges with shape modifications and improve the quality of equilibrium reconstruction. The improved equilibrium reconstruction will enable better estimate of the electron temperature profile, hence also RAPTOR state estimate precision. Last, the information about fast particle pressure will have to be included into the model in order to describe the stabilizing effects of these particles on the sawteeth dynamics.

ACKNOWLEDGEMENTS

At this stage, I would like to thank the people who significantly contributed to this thesis, both directly and indirectly. I appreciated the creative atmosphere in the research team in Consorzio RFX and the help of my supervisors, Dr. Giuseppe Marchiori, who helped me to start my research program in Padova, followed my activities during whole thesis period and has always been helpful and supportive, Dr. Paolo Piovesan for introducing me to the RAPTOR team and help with all RAPTOR related problems whenever it was needed. I would also like to thank many of my colleagues from Consorzio RFX: Dr. Paolo Zanca who provided the basic idea for the shape recontruction algorithms and helped whenever a problem appeared, Dr. Claudio Finotti with whom I collaborated on the shape reconstruction issues, Dr. Chiara Piron for collaboration on RAPTOR on RFX project, Dr. Lionello Marrelli, Dr. Roberto Cavazzana, and Dr. Matteo Zuin for fruitful collaboration on projects related to macroscopic parameters reconstruction on RFX-mod and LH transition attempts. I thank Prof. Paolo Bettini for coordinating the PhD program and his help with organizational issues.

I would like to thank all members of the RAPTOR team I worked with during the last year of my PhD, especially Dr. Federico Felici for coordinating the activities, a lot of help and patience that was needed especially in the beginnings of my RAPTOR work. I thank Dr. Olivier Sauter for support with the disruption prediction experiments on TCV and RFX. I thank also Thomas Blanken for pleasant and effective collaboration on the disruption avoidance activities.

Another important part of the PhD period was spent at IST Lisbon. From this institution, I appreciate the help both with integration in Lisbon and scientific activity provided by prof. Bernardo Brotas Carvalho. I thank to Rafael Henriques for collaboration on the plasma position measurement and for help with all aspects of life in Portugal. I also appreciated Dr. Humberto Figueiredo for the help with the experiments.

I thank my mother Jaroslava, father Frantisek and brother Frantisek for their continuous support during my whole life and my physics related activities, both mental and financial. It would not be possible even to start the PhD without them. I would like to thank my girlfriend Xenia support during the thesis preparation and for tolerating long periods spent abroad. I also highly appreciate

my grandparents Jiri Hruska, Irena Hruskova, and Marie Kudlackova for the stimulating environment they helped to establish during my childhood.

At this stage, I would like to acknowledge the people who helped me in early stages of my physics studies. First of all, I would like to thank Dr. Frantisek Zacek from IPP Prague for recruiting me to the field of nuclear fusion. I would like to thank Dr. Josef Havlicek for the long time he spent introducing me to the field of tokamak and computational physics. I thank Dr. Jan Mlynar for advices related to my academic future, and, together with Dr. Vojtech Svoboda, allowing for the possibility of studying nuclear fusion starting from the bachelor level. I thank Dr. Wolfgang Treutterer who helped me to learn the basics of scientific work and for introducing me to the international fusion community. I thank my secondary school teachers Sarka Frintova, Petr Pajersky, and Alena Havlikova for provoking my interest in mathematics and physics and helping me to gain extra knowledge even before starting the university studies.

This work was supported by the European Commission and carried out within the framework of the Erasmus Mundus International Doctoral College in Fusion Science ans Engineering (FUSION-DC).

This project has received funding from the European Union's Horizon 2020 research and innovation programme under grant agreement number 633053. The views and opinions expressed herein do not necessarily reflect those of the European Commission.

IST activities received financial support from "Fundação para a Ciência e Tecnologia" through project UID/FIS/50010/2013.

Last, not least, I would like to thank my fellows from the PhD programme for making the PhD period much more fun and for their help with integration into Italian society.

APPENDICES

APPENDIX A

Analytical solution of Laplace equation in cylindrical geometry

The solution of the Laplace equation $\Delta\phi = 0$ in cylindrical coordinates can be derived using the following approach: The Δ operator is expressed in cylindrical coordinates as

$$\Delta\phi = \frac{1}{r}\frac{\partial}{\partial r}(r\frac{\partial\phi}{\partial r}) + \frac{1}{\rho^2}\frac{\partial^2\phi}{\partial\theta^2} + \frac{\partial^2\phi}{\partial z^2} = 0. \tag{A.1}$$

Tokamaks are generally considered axi-symmetrical devices, thus all derivatives with respect to z are equal to 0. Let us decompose the potential ϕ into the Fourier serie

$$\phi = \sum_{m=1}^{\infty} \phi_c^m cos(m\theta) + \phi_s^m sin(m\theta) \tag{A.2}$$

Using the Fourier serie, A.1 can be written in form

$$0 = \sum_{m=1}^{\infty} \frac{\partial}{\partial r}(r\frac{\partial\phi_c^m}{\partial r^2})cos(m\theta) + \frac{\partial}{\partial r}(r\frac{\partial\phi_s^m}{\partial r^2})sin(m\theta) - \frac{m^2}{r}\phi_c^m cos(m\theta) - -\frac{m^2}{r}\phi_s^m sin(m\theta). \tag{A.3}$$

Since the base function of the Fourier expansion form an orthonormal basis, A.3 can be solved separately for $sin(m\theta)$ and $cos(m\theta)$ terms. Let us assume that the radial dependence of the $\phi_{c,s}$ r^α. After that

$$0 = \frac{\partial}{\partial r}(r\frac{\partial}{\partial r}\phi_{c,s}^m) - \frac{m^2}{r}\phi_{c,s}^m = (\alpha^2 - m^2)\phi_{c,s}^m \tag{A.4}$$

To meet this condition, $\alpha = \pm m$. Thus, the final form of the Fourier terms of the magnetic potential is

$$\phi_{c,s}^m = A_{c,s}^m r^m + B_{c,s}^m r^{-m} \tag{A.5}$$

APPENDIX B

Equilibrium reconstruction by LIUQE

This appendix contains a description of a real time inverse equilibrium solver LIUQE based on paper [36]. LIUQE was originally developed for TCV, but it can be applied to any air core tokamak device. Recently, the RFX-mod geometry was inserted into the code and first LIUQE results are expected in a few months.

The goal of inverse equilibrium solvers is to find $p'(\psi)$ and $TT'(\psi)$ to satisfy Grad-Shafranov equation

$$\Delta^*\psi = -4\pi^2\mu_0 r(rp' + \frac{TT'}{\mu_0 r}). \tag{B.1}$$

Note that this equation is just another representation of (2.5). The term T is related to the poloidal currents (corresponds to term $I(\psi)$ in (2.5) and p is the plasma pressure. The superscript $'$ refers to the first derivative with respect to ψ. This equation can be rewritten as

$$\Delta^*\psi = -2\pi\mu_0 r(j_\phi + j_e), \tag{B.2}$$

where j_e is the toroidal current density in all parts but the plasma and

$$j_\phi = 2\pi\Big(rp' + \frac{TT'}{\mu_0 r}\Big), \tag{B.3}$$

represents the plasma current. Using this approach, one can separate the contribution of the plasma from the contribution of currents in the poloidal field coils and passive structures. One can relatively easily find the contribution of the external non-plasma currents. However, finding j_ϕ requires the use of dedicated numerical schemes.

In LIUQE Picard iteration is used working as follows:

$$\Delta^* \psi^{t+1} = -2\pi\mu_0 r(j_\phi^t + j_e^t), \tag{B.4}$$

where t is the iteration number. In each iteration step, the boundary between the vacuum region and the plasma is updated. Functions $p'(\psi)$, $TT'(\psi)$ that form plasma current density profile are computed in every iteration to best reproduce the experimental data. A problem with this approach is that the Picard iteration is unstable along vertical direction [125], therefore the plasma axis vertical position must be recovered from external measurement and fixed in the iterations.

During the iteration process, first the plasma boundary is computed. Plasma boundary flux is the highest flux on the first wall or on X-point. The contour line of the boundary flux defines the plasma boundary.

In the following step, p' and TT' are estimated. In order to simplify the algorithm, both functions are parametrized by functions $g_g(\psi)$ that depend just on ψ as follows:

$$j_\phi = 2\pi\left(rp' + \frac{TT'}{\mu_0 r}\right) = \sum_g a_g r^{v_g} g_g(\psi), \tag{B.5}$$

where a_g are the free parameters, v_g is 1 for p' related terms and -1 for TT' terms. The values of a_g are derived from measurements using a quadratic cost function minimization. Such a process provides sufficiently precise information about the plasma equilibrium on TCV in less than 200 μs on a single core processor computer.

On TCV, the following measurements are used to recover the equilibrium by solving (B.1): measurements of currents in all TCV coils, both poloidal and toroidal, 38 flux loops outside the vacuum vessel and 38 magnetic probes located inside the vessel, the loop voltages measured by the flux loops to estimate the vessel currents, diamagnetic measurement and the plasma current measurement. Optionally, Faraday rotation measurements can be incorporated as well to increase the precision of internal profiles reconstruction.

APPENDIX C

State Estimate by Kalman Filter

For control applications, a technique to estimate a state of the system as close to the real state as possible in presence of noise is required. This task is called *optimal estimation problem* and the solution was proposed by Kalman. The description in this appendix is based on [124].

Let us start from the following plant model:

$$\begin{aligned} \dot{x} &= F(t)x(t) + G(t)u(t) + v(t) \\ y &= H'(t)x(t) + w(t), \end{aligned} \tag{C.1}$$

where x is the state vector, u is the input vector to the plant and v, w are the zero-mean Gaussian sources of white (covering full frequency spectrum) noise with the following properties:

$$\begin{aligned} E[v(t), v(\tau)] &= Q(t)\delta(t-\tau) \\ E[w(t), w(\tau)] &= R(t)\delta(t-\tau) \\ E[w(t), v'(\tau)] &= 0 \quad \forall\ t, \tau. \end{aligned} \tag{C.2}$$

The matrix functions F, G, and H describe the relation between inputs, states, and outputs in the plant.

The target of the optimal estimate problem is to minimize the error variance of the state at every time:

$$\sigma^2 = E\Big\{[x(t_1) - x_e(t_1)]'[x(t_1) - x_e(t_1)]\Big\}, \tag{C.3}$$

where x is the real state and x_e is the state estimate by (C.1). Assume the existence of a matrix function $M(t)$ for which

$$x_e(t_1) = \int_{t_0}^{t_1} M'(t)y(t)dt \tag{C.4}$$

provides minimum variance estimate and define a matrix function $Z(t)$

$$\begin{aligned} \dot{Z} = -F'(t)Z(t) + H(t)M(t); Z(t_1) = I \\ \frac{d}{dt}[x(t)Z(t)] = M'y - M'w + Z'v, \end{aligned} \tag{C.5}$$

where I is a unit matrix. One can show that

$$\begin{aligned} E\Big\{[x(t_1) - x_e(t_1)]'[x(t_1) - x_e(t_1)]\Big\} = \\ = trace\Big\{Z'(t_0)P_{e0}Z(t_0) + \int_{t_0}^{t_1}[M'(t)R(t)M(t) + Z'(t)Q(t)Z(t)]dt\Big\}. \end{aligned} \tag{C.6}$$

The function M reads as

$$M^* = R^{-1}(t)H'(t)P_e(t)Z(t), \tag{C.7}$$

where

$$\begin{aligned} \dot{P}_e(t) = P_e(t)F'(t) + F(t)P_e(t) - P_e(t)H(t)R^{-1}(t)H'(t)P_e(t) + Q(t) \\ \frac{d}{dt_1}Z'(t,t_1) = [F(t_1) - P_e(t_1)H(t_1)R^{-1}(t_1)H'(t_1)]Z'(t,t_1), \end{aligned} \tag{C.8}$$

where $Z(t,t_1)$ denotes to integral of (C.5) from t to t_1. To obtain the optimal state estimation, the first line of (C.1) is realized as follows:

$$\begin{aligned} \dot{x_e} = F(t)x_e(t) + K_e(t)[H'(t)x_e(t) - y(t)] \\ K_e(t) = -P_e(t)H(t)R^{-1}(t). \end{aligned} \tag{C.9}$$

All the matrixes used above but Q and R can be derived from the physical model describing the plant. The choice of Q and R is arbitrary and depends on system properties.

Bibliography

[1] Key World Energy Statistics 2014, International Energy Agency,

[2] UN Human Development Report 2007

[3] Kikuchi M., Lackner K, Minh Quang Tran, Fusion Physics, International Atomic Energy Agency, Vienna, 2012, ISBN 978–92–0–130410–0

[4] O. A. Hurricane, Nature, 2014, 506, doi:10.1038/nature13008

[5] Laser Megajoule official web, www-lmj.cea.fr/en/lmj/index.htm, accesed on 04/08/2015

[6] H. W. Muller, M. Hirsch Proceedings of IPP Summer University for Plasma Physics, Greifswald, 2007

[7] Wesson et al, Tokamaks, 3rd edition, Oxford University Press 2004, ISBN: 0198509227

[8] Freidberg J., Plasma Physics and Fusion Energy, Cambridge University press 2007, ISBN-13 978-0-521-85107-7

[9] Chen F., An Indispensable Truth, Springer 2011, ISBN 978-1-4419-7820-2

[10] Kulhanek P., Teorie plazmatu, Czech Technical University textbook, ISBN 978-80-904582-2-2, online at http://www.aldebaran.cz/studium/fpla.pdf, accessed on 14/01/16

[11] Shafranov V.D., 1958 Soviet Physics JETP 6 (3) 1013

[12] O. Kudlacek, Rizeni polohy plazmatu v tokamaku COMPASS s prihlednutim k t-lumicimu efektu vodive komory zarizeni, 2011, master thesis, available online at http://physics.fjfi.cvut.cz/publications/FTTF/DP_Ondrej_Kudlacek.pdf

[13] Wagner, F., et al., Physical Review Letters 49 (1982) 1408, doi: 10.1103/PhysRevLett.49.1408

[14] Soldner, F.X., JET TEAM, Plasma Phys. Control. Fusion 39 (1997) B353, doi: 10.1088/0741-3335/39/12B/027

[15] Wolf, R.C., et al., Nucl. Fusion 41 (2001) 1259, doi: 10.1088/0029-5515/41/9/315

[16] CAE official webpage, http://www-fusion-magnetique.cea.fr/gb/fusion/physique/modesconfinement.htm, accessed on 12/08/2015

[17] Evans, T. E. et al., Physical Review Letters (2004) 92.23, doi: 10.1103/PhysRevLett.92.235003

[18] Suttrop, W. et al., Physical Review Letters (2011) 106.22, doi: 10.1103/PhysRevLett.106.225004

[19] TC Hender et al., 2007, 47, S128. doi: 10.1088/0029-5515/39/12/303

[20] Fernandes H. et al, 20 Years of ISTTOK Tokamak Scientific Activity, 2012, Accessed 28/05/15, www-naweb.iaea.org/napc/physics/FEC/FEC2012/papers/651_OVP08.pdf

[21] R. Henriques et al, Review of Scientific Instruments, 2012, 83, 10D705, doi: 10.1063/1.4729496

[22] R. Henriques et al, Review of Scientific Instruments, 2014, 85, 11D848, doi: 10.1063/1.4891045

[23] P. Sonato et al, 2003 Fusion Engineering and Design, Volumes 66-68, 161-168, doi: 10.1016/S0920-3796(03)0017-7

[24] Martin, P., Fusion Science and Technology, Vol. 59, p. 602-616

[25] Marrelli L. et al, Feedback control of the m=1, n=2 mode in RFX-mod tokamak plasma with qcyl(a) < 2, 38th EPS Conference on Plasma Physics

[26] P Zanca et al 2012 Plasma Phys. Control. Fusion 54 094004, doi: 10.1088/0741-3335/54/9/094004

[27] spc.epfl.ch, accessed on 12/10/2015

[28] Hofman F. et al, 1994, Plasma Physics and Controlled Fusion 36, B277, doi: 10.1088/0741-3335/36/12B/023

[29] Franke S., Phd thesis n. 1654, 1997, Ecole Polytechnique Federale de Lausanne

[30] Barry S., 1997, Proceedings of the 8th international symposium on Laser-aided Plasma Diagnostics, Doorwerth, The Netherlands

[31] http://www.ipp.mpg.de/16208/einfuehrung, accessed on 02/12/15

[32] www.iter.org

[33] Kocman J., master thesis, FJFI CVUT Prague, 2015

[34] Janky et al, Fusion Engineering and Design, 2011, Vol. 86, 1120-1124, doi: 10.1016/j.fusengdes.2011.01.143

[35] Janky et al, Fusion Engineering and Design, 2014, Vol. 89, 186-194, doi: 10.1016/j.fusengdes.2013.12.042

[36] Hofman F., Tonetti G., 1998, Nucl. Fusion 28 1871, doi: 10.1088/0029-5515/40/4/302

[37] Bettini P. et al, 2005, Nucl. Fusion 45, 1–12, doi: 10.1088/0029-5515/45/1/001

[38] P. Bettini et al, 2003, Nucl. Fusion 43 (2003), 119–129, doi: 10.1088/0029-5515/43/2/305

[39] L.L. Lao et al, 1985, Nucl. Fusion 25 1611, doi: 10.1088/0029-5515/25/11/007

[40] D.W. Swain, G.H. Nielson, 1982, Nuclear Fusion 22 (8) 1015, doi: 10.1088/0029-5515/22/8/002

[41] F. Alladio, F. Crisanti, 1986, Nuclear Fusion 26 (9) 1143, doi: 10.1088/0029-5515/26/9/002

[42] L. Zabeo et al, Fusion Engineering and Design 82 (2007) 1081-1088, doi: 10.1016/j.fusengdes.2007.04.028

[43] Ferron J.J. et al, 1998, Nucl. Fusion 38 1055, doi: 10.1088/0029-5515/38/7/308

[44] O'Brien et al, 1992, Nucl. Fusion 32 1351, doi: 10.1088/0029-5515/32/8/105

[45] O'Brien et al, 1993, Nucl. Fusion 33 467, doi: 10.1088/0029-5515/33/3/108

[46] Pustovitov V.D., 2001, Nucl. Fusion 46 721, doi: 10.1088/0029-5515/41/6/307

[47] K. Kurihara, 1993 Nucl. Fusion 33 399, doi: 10.1088/0029-5515/33/3/103

[48] Blum J. et al, 2012 Journal of Computational Physics 231 960, doi: 10.1016/j.jcp.2011.04.005

[49] P Zanca and S Martini, 1999, Plasma Physics and Controlled Fusion 41 1251, doi:10.1088/0741-3335/41/10/304

[50] O. Kudlacek et al, EPS 2014 Berlin, P5.062

[51] G. Marchiori et al, EPS 2014 Berlin, P5.040

[52] Kudlacek O et al, 2015, Physics of Plasmas, 22, 102503, doi: 10.1063/1.4932992

[53] Barabaschi P., The MAXFEA code, Plasma Control Technical Meeting, Naka (Japan) 1993

[54] G. Manduchi et al, 2012, Fusion Engineering and Design, 87, 1907, doi: 10.1016/j.fusengdes.2012.05.014

[55] D'haeseleer W. D., Flux Coordinates and Magnetic Field Structure, Springer Verlag 1991, ISBN 0387524193

[56] Durand, Magnetostatique, Masson et C., Paris, 1968

[57] Zanca P., 2007, Nucl. Fusion 47 1425, doi: 10.1088/0029-5515/47/11/004

[58] Swain D.W., 1982, Nucl. Fusion 22 1015, doi: 10.1088/0029-5515/22/8/002

[59] Solovev L.S., 1967, Sov. Phys. JETP, 26:400

[60] Jardin S., Computational Methods in Plasma Physics, CRC Press 2010, ISBN 9781439810217

[61] Marchiori G. et al, 2015, 'Design and operation of the RFX-mod Plasma Shape Control System', submitted to Fusion Engineering and Design

[62] R. Albanese and F. Villone, 1998, Nuclear Fusion 38 723, doi: 10.1088/0029-5515/38/5/307

[63] F. Villone et al., 1997, Nuclear Fusion 37 1395-1410, doi: 10.1088/0029-5515/37/10/106

[64] R. Albanese et al., 2004, Nuclear Fusion 44 999–1007, doi: 10.1088/0029-5515/44/9/009

[65] R. Albanese et al., 2005, Fusion Engineering and Design 74, p. 627-632, doi: 10.1016/j.fusengdes.2005.06.290

[66] Wotton A., *Magnetic fields and tokamak plasmas*

[67] Moret J. M., 2003, Review of Scientific instruments, Vol. 74, Issue 11, p. 4634-4643, doi: 10.1063/1.1614856

[68] Lao L.L. et al: 1985 Nucl. Fusion 25 1421, doi: 10.1088/0029-5515/25/10/004

[69] Havlicek J. et al: Global Power Balance in Non-Stationary Discharge Phases in the COMPASS Tokamak, WDS 2014

[70] Martin Y. et al, 2008, Journal of Physics: Conference Series 123, 012033, doi: 10.1088/1742-6596/123/1/012033

[71] Ryter F. et al: EPS 2014 Berlin, P2.016

[72] Ryter F. et al, 2009, Nuclear Fusion 49, 062003, , doi: 10.1088/0029-5515/49/6/062003

[73] Sauter P. et al, 2012, Nuclear Fusion 52, 012001, doi: 10.1088/0029-5515/52/3/032004

[74] Bush C. E. et al, 1990, Physical Review Letters 65, 424, doi: 10.1103/PhysRevLett.64.531

[75] ASDEX team, 1989, Nuclear Fusion 29, 1959, doi: 10.1088/0029-5515/29/11/010

[76] Tibone F. et al, 1993, Nuclear Fusion 33, 1319, doi: 10.1088/0029-5515/33/9/107

[77] Yushmanov P. N. et al, 1990, Nuclear Fusion 30, 1999, doi: 10.1088/0029-5515/30/10/001

[78] Thomas D. M. et al, 1998, Plasma Physics and Controlled Fusion, V. 40, 5, 707, doi: 10.1088/0741-3335/40/5/054

[79] Panek R. et al, 2013, 40th EPS Conference, Espo, P4.103

[80] Taylor J. R. et al, 1989, Physical Review Letters, 63, number 21, p. 2365, doi: 10.1103/PhysRevLett.63.2365

[81] P.E.Phillips, et al., 1987, Journal Nuclear Materials 145-147 807, doi: 10.1016/0022-3115(87)90450-8

[82] Kirneva N. et al., 2003, Plasma Physics and Controlled Fusion, 45 337, doi: 10.1088/0741-3335/45/5/320

[83] Stockel J. et al, 1999, 26th EPS conference Maasricht, ECA Vol.23J 1589 - 1592

[84] Henriques R. et al, 2015, 42nd EPS conference Lisbon, O1.101

[85] Marrelli L., 2015, Tokamak Experiments in RFX-mod, RFP Workshop, USTC, Hefei

[86] Zohm, H. et al., 1999, Nuclear Fusion 39.5, p. 577, doi: 10.1088/0029-5515/39/5/101

[87] Chapman, I .T. et al., 2007, Plasma Physics and Controlled Fusion 49.12B, B385, doi: 10.1088/0741-3335/49/12B/S35

[88] Chapman, I. T. 2011, Plasma Physics and Controlled Fusion 53.1, p. 013001, doi: 10.1088/0741-3335/53/1/013001

[89] Felici F. et al, 2011, Nuclear Fusion 51.8, p. 083052, doi: 10.1088/0029-5515/51/8/083052

[90] Felici F., Phd thesis, Ecole Polytechnique Federale de Lausanne, 2011, number 5203

[91] Geelen P., Felici F., Merle A., Sauter O., 2015, Plasma Physics and Controlled Fusion 57 125008, doi: 10.1088/0741-3335/57/12/125008

[92] Felici F. et al, 2014, A dynamic state observer for real-time reconstruction of the tokamak plasma profile state and disturbances, American Control Conference, doi: 10.1109/ACC.2014.6858781

[93] Pereverzev, G. V. and P.N. Yushmanov, 2002, Tokamak. Tech. rep. 5/98. IPP Report

[94] Crotinger, J.A. et al., 1997, UCRL-ID-126284. Tech. rep. LLNL

[95] Kim, S. H. et al., 2009, Plasma Physics and Controlled Fusion 51.10, pp. 105007, doi: 10.1088/0741-3335/49/12B/S35

[96] Fischer R. et al, 2016, Coupling of the Flux Diffusion Equation with the Equilibrium Reconstruction at ASDEX Upgrade, accepted for Fusion Science and Technology

[97] Erba M. et al, 1998, Nuclear Fusion, 38, p. 1013, doi: 10.1088/0029-5515/38/7/305

[98] C. Piron, 2015, Phd thesis, Universita degli studi di Padova

[99] Kadomtsev B. B., 1987, Reports on Progress in Physics, 50:115, doi: 10.1088/0034-4885/50/2/001

[100] F. Porcelli et al., 1996, Plasma Physics and Controlled Fusion, 38(12) 2163, doi: 10.1088/0741-3335/38/12/010

[101] Pautasso G. et al, 2002, Nuclear Fusion 42 100 - 8, doi: 10.1088/0029-5515/42/1/314

[102] Cannas B. et al, 2004, Nuclear Fusion 44 68 - 76, , doi: 10.1088/0029-5515/44/1/008

[103] Murari et al, 2009, Nuclear Fusion, 49, 055028, doi:10.1088/0029-5515/49/5/055028

[104] Odstrcil M., 2012, master thesis, title 'Application of Machine Learning Tools to the Analysis of Tokamak Massive Databases', Czech Technical University, online at http://physics.fjfi.cvut.cz/publications/FTTF/DP_Michal_Odstrcil.pdf

[105] CG Windsor et al, 2005, Nuclear fusion 45, p. 337. doi:10.1088/0029-5515/45/5/004.

[106] Hender T.C. et al, 2007, Nuclear Fusion 47 S128, doi: 10.1088/0029-5515/47/6/S03

[107] N. A. Kirneva, 2014 et al., Plasma Physics and Control Fusion, 57, 025002, doi: 10.1088/0741-3335/57/2/025002

[108] Sauter O. et al, 2014, Physics of Plasmas 21, 055906; doi: 10.1063/1.4876612

[109] Piron C. et al, "Real-time simulation of internal profiles in the presence of sawteeth using the RAPTOR code and applications to ASDEX Upgrade and RFX-mod", submitted to Nuclear Fusion

[110] Bonfiglio D. et al, 2010, Physics of Plasmas 17, 082501; doi: 10.1063/1.3462908

[111] Sauter O. et al, 1997, Physics of Plasmas, 4, 1654, doi: 10.1063/1.872270

[112] Martin P. et al, 1996, Plasma Physics and Controlled Fusion 38 1023, doi: 10.1088/0741-3335/38/7/007

[113] Murari A. et al, 1999, Review of Scientific Instruments 70 581, doi: 10.1063/1.1149342

[114] Felici F. et al, 2015, 42nd EPS Lisbon, O4.127

[115] Politzer P.A. et al, 32nd EPS 2005 Tarragona, O-1.001

[116] Jardin S. C. et al, 2015, Physical Review Letters, 115, 215001, doi: 10.1103/PhysRevLett.115.215001

[117] Bonfiglio D. et al, 2005, Physical Review Letters, 94, 145001, doi: 10.1103/PhysRevLett.94.145001

[118] E. Poli et al, 2001, Computer Physics Communications Volume 136, Issues 1–2, Pages 90–104, doi: 10.1016/S0010-4655(01)00146-1

[119] M. Brambilla and R. Bilato, 2006, Nuclear Fusion, Volume 46, Number 7, doi: 10.1088/0029-5515/46/7/S01

[120] A. Pankin et al, 2004, Computer Physics Communications, Vol. 159, Page 157, doi: 10.1016/j.cpc.2003.11.002

[121] H. Bindslev et al, 1999, Physical Review Letters 83, 3206, doi: 10.1103/PhysRevLett.83.3206

[122] Citrin J. et al, 2015, Nuclear Fusion 55 092001, doi:10.1088/0029-5515/55/9/092001

[123] Fischer R. et al, 2003, Plasma Physics and Controlled Fusion 45 1095, doi 10.1088/0741-3335/45/7/304

[124] Anderson B. D. O., Moore J. B., Optimal Control, 2007 by Prentice-Hall, New Jersey, ISBN 0-48645766-4

[125] Lackner K., 1976, Computer Physics Communications 12 33, doi: 10.1016/0010-4655(76)90008-4